

NEWTON Deliverable D3.4

Final Design Report: NEWTON instrument prototype 1

Project Number:	730041
Project Title	New portable multi-sensor scientific instrument for non-invasive on-site characterisation of rock from planetary surface and sub-surfaces.
Deliverable Type:	Public

Title:	D3.4 - Final Design Report: NEWTON instrument prototype 1
Work Package:	Work Package 3
Responsible:	INTA
Due Date:	30.04.2018
Nature:	Report
Security:	Public
Version:	1.0
Authors:	
	TTI: Cristina Lavín, Laura González, Reinel Marante
	INTA: Marina Díaz, José Luis Mesa, Javier de Frutos, Miguel Ángel Rivero, Amanda Ordoñez, Veracruz González
	UPM: Claudio Aroca, Mar Sanz, Marco Maicas, Marina Pérez, Pedro Cobos
	UT: Rolf Kilian

Abstract: As it is included in NEWTON DoA, D3.4 - Final design and validation report for the magnetic head, should describe the final design and validation of the magnetic head. However, during the first NEWTON periodic review it was agreed to modify the content and objectives of deliverables D3.4, D3.5 and D3.6 and to include in each of them the final design of NEWTON prototypes 1, 2 and 3 respectively. This was requested with the aim of improving the comprehensibility of the documents and the activities developed for the completion of the final design of each instrument. Due to this reason, this document, renamed as D3.4 - Final Design Report: NEWTON instrument prototype 1, describes the final design of the NEWTON instrument prototype 1, as well as the functional verification of its key building blocks, i.e. Sensor Unit, electronic Control Unit and the Power Distribution Unit.

Keyword list: Planetary Science, complex susceptibility, multi-sensor system, Mars, the Moon, control unit, lock-in, signal processing, susceptometer, magnetometer, magnetic amplifier.

Disclaimer: This document reflects the contribution of the participants of the research project NEWTON. The European Union and its agencies are not liable or otherwise responsible for the contents of this document; its content reflects the view of its authors only. This document is provided without any warranty and does not constitute any commitment by any participant as to its content, and specifically excludes any warranty of correctness or fitness for a particular purpose. The user will use this document at the user's sole risk.

Executive Summary

As it is included in NEWTON DoA, D3.4 - Final design and validation report for the magnetic head should describe the final design and validation of the magnetic head. However, during the first NEWTON periodic review it was agreed to modify the content and objectives of deliverables D3.4, D3.5 and D3.6 and to include in each of them the final design of NEWTON prototypes 1, 2 and 3 respectively. This was requested with the aim of improving the comprehensibility of the documents and the activities developed for the completion of the final design of each instrument. Due to this reason, this document, renamed as D3.4 - Final Design Report: NEWTON instrument prototype 1, describes the final design of the NEWTON instrument prototype 1, as well as the functional verification of its key building blocks.

With the aim of maximizing the impact of novel NEWTON technology, different prototypes are being developed within the project. Two prototypes (named prototype 1 and 3) are being developed for planetary application, while a slightly (reduced) adapted version of prototype 1 (named prototype 2) will be developed in order to demonstrate the spin-off of the technology between space and non-space fields. The three prototypes share the same architecture while they provide different performance capabilities adapted to different scenarios. The key building blocks of the three prototypes are the same, i.e. Power Distribution Unit (PDU), the electronic Control Unit (CU) and the Sensor Unit (SU). As already indicated, this document reports the final design of prototype 1, as well as the functional verification of its Sensor Unit, electronic Control Unit and Power Distribution Unit, while D3.5 and D3.6 describe the final design of NEWTON prototype 2 and 3 respectively, as well as the functional verification of their respective key blocks.

This document is structured in different sections. Section 2 gives an overview of the architecture and main features of NEWTON instrument prototype 1. Section 3, 4 and 5 describe respectively the final design of the Sensor Unit, electronic Control Unit and Power Distribution Unit. The functional verification of each key building block is also included in the respective section. Finally, Section 6 presents a summary of the content included in this document, the main conclusions on the degree of advance obtained from it as well as the future lines of work. In addition to this, Annex 1 and 2 provides the schematics and the list of components of the PDU and a last section is included with the referenced bibliography.

Authors

Partner	Name	Email
TTI	Cristina Lavín	clavin@ttinorte.es
	Laura González	lgonzalez@ttinorte.es
	Reinel Marante	rmarante@ttinorte.es
INTA	Marina Díaz	diazma@inta.es
	José Luis Mesa	mesaujl@inta.es
	Javier de Frutos	frutosfj@inta.es
	Miguel Ángel Rivero	riveroma.pers_externo@inta.es
	Amanda Ordoñez	arlensiuoca@inta.es
	Veracruz González	gonzalezgv@inta.es
UPM	Claudio Aroca	claudio.aroca@upm.es
	Mar Sanz	mar.sanz.lluch@upm.es
	Marco Maicas	marco.maicas@upm.es
	Marina Pérez	marina.perez@isom.upm.es
	Pedro Cobos	pedro.cobos@upm.es
UT	Rolf Kilian	kilian@uni-trier.de

Table of Contents

1.	INTRODUCTION.....	7
2.	NEWTON PROTOTYPE 1	8
3.	SENSOR UNIT	10
3.1.	OVERVIEW AND TARGET REQUIREMENTS.....	16
3.2.	DETAILED DESIGN.....	18
3.2.1.	Ferrite H core design.....	18
3.2.2.	Magnetic Amplifier design	20
3.2.3.	Electrical Resonant Circuit design	21
3.3.	FUNCTIONAL VERIFICATION	22
3.3.1.	Measurement on the input resistor.....	22
3.3.2.	Measurement on the secondary coils.....	23
3.4.	PRELIMINARY VIBRATION AND AMBIENT TESTS.....	25
3.4.1.	Vibration test	25
3.4.2.	Thermal-Vacuum Test (TVT).....	29
3.4.3.	Conclusions of preliminary tests	30
3.5.	MAGNETOMETER POSITION	31
4.	ELECTRONIC CONTROL UNIT	33
4.1.	OVERVIEW AND TARGET REQUIREMENTS.....	33
4.2.	DETAILED DESIGN	33
4.2.1.	Hardware system for excitation and measurement.....	33
4.2.2.	Explanation of the codes using in the system.....	43
4.3.	FUNCTIONAL VERIFICATION.....	46
5.	POWER DISTRIBUTION UNIT	48
5.1.	OVERVIEW AND TARGET REQUIREMENTS.....	48
5.1.1.	Background from the preliminary design	50
5.2.	DETAILED DESIGN	50
5.2.1.	Non-Isolated DC/DC converter.....	50
5.2.2.	Isolated DC/DC converter.....	56
5.3.	FUNCTIONAL VERIFICATION	60
5.3.1.	Non-Isolated DC/DC converter.....	60
5.3.2.	Isolated DC/DC converter.....	62
6.	SUMMARY AND CONCLUSIONS	65
	ANNEX 1: NON-ISOLATED DC/DC CONVERTER	66
	ANNEX 2: ISOLATED DC/DC CONVERTER.....	74
	REFERENCES	81

Abbreviations

A	Ampere
AC	Alternating Current
ADC	Analog to Digital Converter
ACK	Acknowledgement
AMR	Anisotropic Magneto Resistance
ARM	An hysteretic Remanence Measurements
B	Magnetic Induction
BGA	Ball Grid Array
COTS	Commercial off the shelf
CU	Control Unit
D	Deliverable
DAC	Digital to Analog Converter
DC	Direct Current
DoA	Description of Action
DSP	Digital Signal Processor
eGaN	Enhanced Gallium Nitride
EMI	Electromagnetic Interference
FET	Field Effect Transistor
GaN	Gallium Nitride
HB	Half Bridge
IEEE	Institute of Electrical and Electronics Engineers
INTA	Instituto Nacional Técnica Aeroespacial “Esteban Terradas”
IRM	Isothermal Remanent Magnetization
IS	International System
LSB	Least Significant Byte
M	Magnetization
MOSFET	Metal-Oxide Semiconductor Field-Effect Transistor
MSB	Most Significant Byte
NACK	Negative Acknowledgement
NRM	Natural Remanent Magnetization
PC	Personal Computer
PCB	Printed Circuit Board
PDU	Power Distribution Unit
PIV	Peak Inverse Voltage
PWM	Pulse Width Modulation
PS	Portable Susceptometer
QUCS	Quite Universal Circuit Simulator
R	Resistance
SCLK	Serial Clock
SDI	Serial Digital Interface
SDO	Serial Data Output
SH	Sensor Head

SMPM	Switch Model Power Supply
SPI	Serial Peripheral Interface
SQUID	Superconducting Quantum Interference Devices
SU	Sensor Unit
T	Teslas
TBC	To Be Completed
TBD	To Be Determined
TLL	Transistor-Transistor Logic
TRL	Technology Readiness Level
TTI	Tecnologías de Telecomunicaciones e Información
TUF	Transformer Utilization Factor
TVT	Thermal Vacuum Test
UPM	Universidad Politécnica Madrid
USART	Universal Synchronous and Asynchronous Receiver-Transmitter
UT	University of Trier
V	volts
VSM	Vibrating Sample Magnetometer
WP	Work Package

1. INTRODUCTION

Magnetic characterization is essential to know the past and present of planetary objects. The objective of magnetic prospecting is to perform the complete characterization of the magnetic environment. The magnetic field constitutes by itself an incomplete source of information, given that a simple measurement is not enough to determine the magnetic source, much less the characteristics of the source. To acquire such information, complementary measurements are needed. To make magnetic prospecting in-situ, requires a magnetic susceptometer (it's real: χ' and imaginary: χ'' parts) to determine the magnetic structure recorded during the formation of the studied rocks. These measures with the combination of vector magnetometers to know the total magnetic field (B) and its components (B_x , B_y , B_z), complete a total study for the planetary exploration.

NEWTON project aims to develop novel instrumentation beyond the state of the art to perform a complete, in-situ magnetic characterization, by means of field and susceptibility measurements during planetary exploration with rovers and spun off to Earth surveys. As the principal scope of the project is the planetary exploration, a combined magnetic characterisation and susceptibility measurements are considered a breaking through technology capable to provide geological information of planetary bodies and even biological implications [1]. NEWTON instrument includes magnetometer, portable susceptometer, power supply system immune to radiation and a frequency generation system. The magnetic field measurement part of the instrument will be inherited from the design of AMR instrument for Exomars 2020 mission, led by NEWTON technical coordinator, Dr. Marina Díaz Michelena.

As already mentioned, with the aim of maximizing the impact of novel NEWTON technology, three different prototypes are being developed within the project. The prototypes which share the same architecture and provide different performance capabilities adapted to different scenarios are:

- **Prototype 1:** This prototype is designed for planetary exploration missions with the particular case of Martian and Moon's system with an envelope adapted to a rover-mounted payload. This prototype performs in-situ measurements of the complex susceptibility in a planetary environment combined with vector Natural Remanent Magnetization (NRM) data. This prototype will work in a sweep of continuous frequencies.
- **Prototype 2:** This prototype is a reduced version of prototype 1 implemented on a hand-held device for a rapid and preliminary analysis of surface during prospecting on Earth. This prototype performs in-situ measurements of the susceptibility at discrete frequencies. It will be employed to potentiate the impact of NEWTON technology not only in space sector, but also on Earth for civil engineering applications.
- **Prototype 3:** This prototype is an advanced system for the in-situ analysis and full magnetic characterization of drilled samples in the medium term missions with more powerful rovers or to be part of base stations with the particular case of Martian and Moon's systems. This prototype performs in-situ measurement of the susceptibility, demagnetization and isothermal remanent magnetization (IRM) acquisition experiments.

The present document describes the final design of the NEWTON instrument prototype 1, its capabilities and the measurement procedures. Environmental issues and technology maturity are addressed in pursuit of the objective level of TRL 6, by means of execution of environmental testing, such as vibration test and thermo-vacuum test. The final design of NEWTON instrument prototype 2 and 3 are respectively reported in deliverables D3.5 [2] and D3.6 [3].

2. NEWTON PROTOTYPE 1

The architecture of prototype 1 is depicted in the following block diagram, which has been updated from deliverable D3.1 [4].

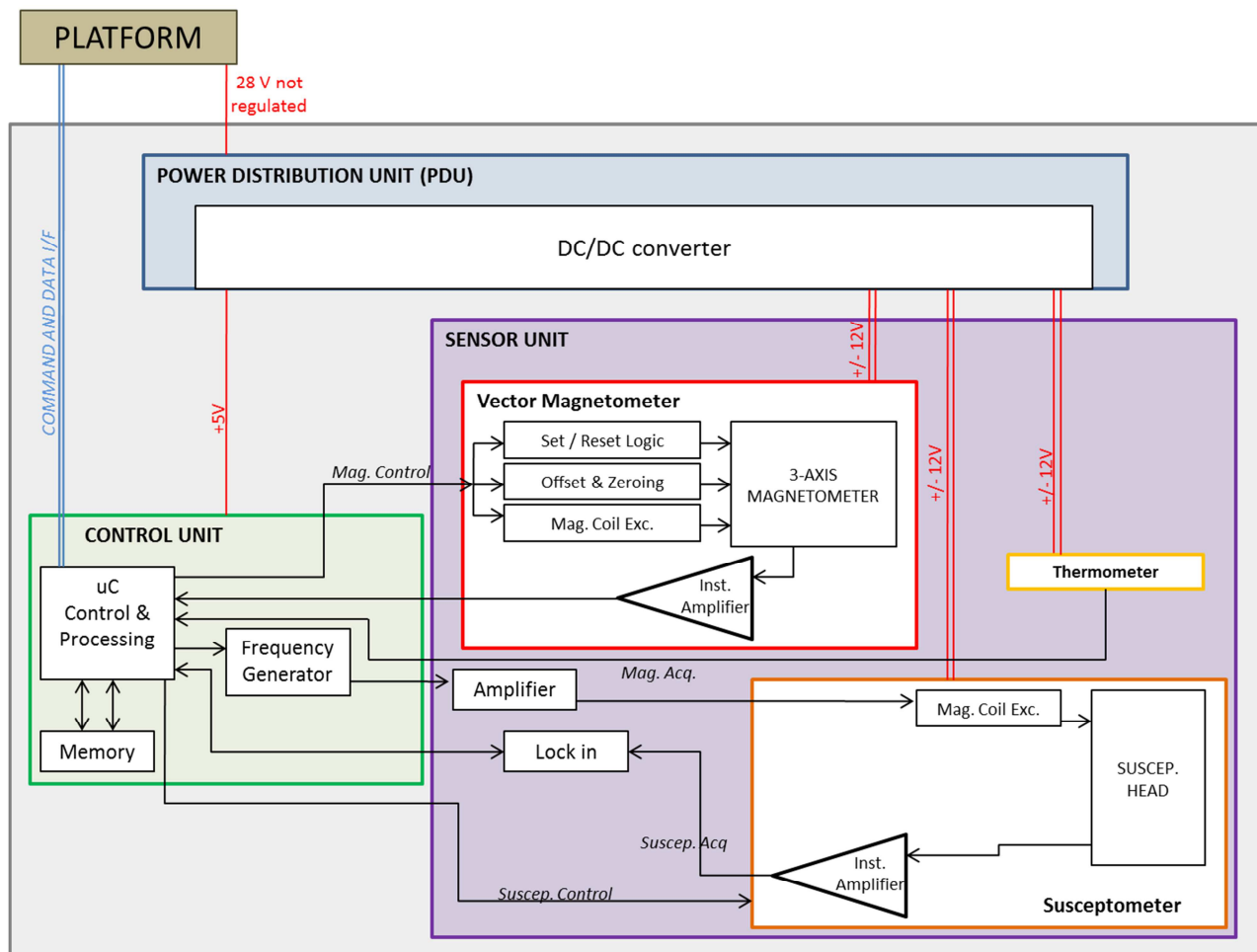


FIGURE 1. Block Diagram of the NEWTON multi-sensor instrument for prototype 1.

The Sensor Unit

The Sensor Unit assembly gathers all the sensing parts of the instrument: susceptometer, magnetometer and thermometer. They, together with the rest of proximity electronics of the SU have been designed with criteria of suitability to planetary exploration missions on board rovers, and the target specifications have been aligned with those for missions to Mars, more specifically the mission Exomars 2020. The Vector Magnetometer measures the environmental magnetic field, the superposition of the global and the crustal fields, and the Susceptometer measures the magnetic complex susceptibility in a sweep of 10 to 40 kHz within the range of 10 to 100 kHz. Current frequency sweeps using the magnetic amplifier are: 5 kHz up to 15 kHz with the biggest capacitor (4.7 μF), 15 kHz up to 40 kHz with the medium size capacitor and 40 kHz up to 80 kHz using the smallest considered capacitor (0.15 μF).

The magnetometer is based on COTS technology, a designed based on the heritage of NEWTON group.

The susceptometer is based on a ferrite core with a H shape (L). The construction of the sensor head is based on a couple of U ferrite cores (originally designed for transformer cores), forming a H shape and with

a primary coil on each of the four arms of the H. The primary coils are connected in series and forms part of an electrical resonant circuit (FIGURE 2). It is included in the electrical circuit a magnetic amplifier (L_{var}) to achieve different resonance frequencies avoiding high current switches.

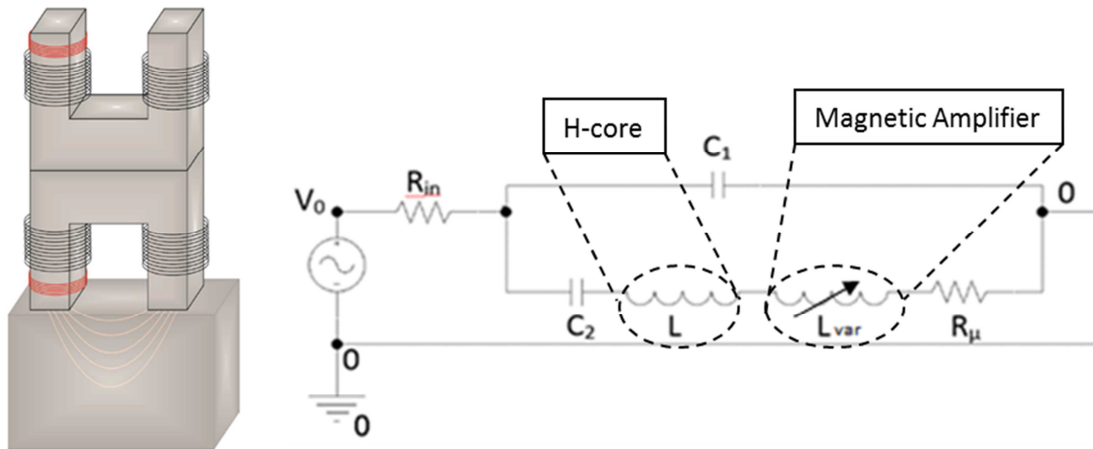


FIGURE 2. H-core illustration (left). Block Diagram of the NEWTON multi-sensor instrument for prototype 1 (right).

Additionally, the SU includes a temperature sensor for a proper thermal calibration of Susceptometer and Vector Magnetometer data.

The Power Distribution Unit

The Power Distribution Unit supplies energy to the Control and to the Sensor Units. The PDU is integrated by the power module, i.e. DC/DC converter, and the AC current source. For prototypes 1 and 2, the current is sourced by the resonance of the circuit and therefore, there is no extra AC current source. In this case, the control unit includes a power inverter to change direct current into alternating current (DC/AC). The alternating voltage working cycle is controlled by a microprocessor and continuous voltage is controlled by magnetic transformers.

The DC/DC converter receives the primary power from the rover or external batteries, i.e. 28 V not regulated, and it generates the secondary lines to supply the Sensor and the Control Units.

The Control Unit

The Electronic Control Unit is the responsible of the control, acquisition and processing of the signals of the sensor unit. The microcontroller performs these tasks as well as it generates the different frequency signals for the susceptometer and magnetometer. The detection will have scalable performance between the different prototypes.

Apart from the micro controller, the CU includes an oscillator to generate a stable reference frequency and a memory to save the input data measurements. The lock-in amplifiers are allocated inside the SU module analog circuitry. A Digital Signal Processing (DSP) lock-in was studied but it was discarded given the complexity involved in the sample rate required for the measuring frequency range (DC to 100 kHz).

3. SENSOR UNIT

As aforementioned, the sensor unit includes the magnetometer, the susceptometer and the thermometer. **The magnetometer** is an HMC1023 3-axis magnetic sensor manufactured by Honeywell. It is a high performance three-axis magneto-resistive sensor design in a single package. The advantages of the HMC1023 include orthogonal three-axis sensing, small size and a 16- contact Ball Grid Array (BGA) surface mount package. Each of the magneto-resistive sensors is configured as 4-element Wheatstone bridge to convert magnetic fields to differential output voltages. Capable of sensing fields down to 8.5 nT, these sensors offer a compact, high sensitivity and highly reliable solution for low field magnetic sensing.

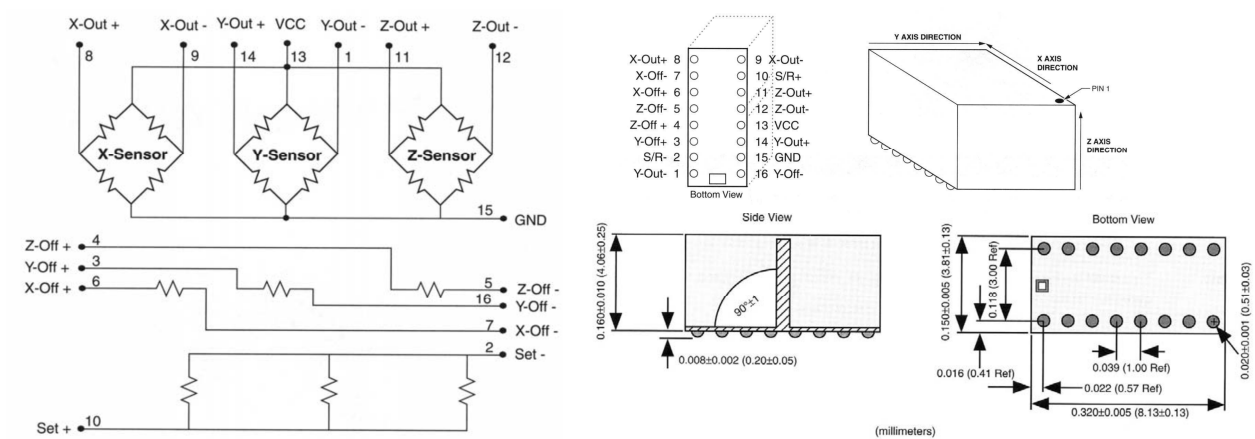


FIGURE 3. HMC1023 Circuit Diagram

The main features of the HMC1023 sensor are listed below, while TABLE 1 depicts the specification of this sensor:

- BGA Surface-Mount Package
- Three Orthogonal Magneto-Resistive Sensors
- Wide Field Range of $\pm 600 \mu\text{T}$ ($\pm 6 \text{ G}$)
- 1.0 mV/V/gauss Sensitivity
- Minimum Detectable Field to 8.5nT (85 μG).
- Patented On-Chip Set/Reset and Offset Straps

TABLE 1. HMC1023 specifications.
SPECIFICATIONS

Characteristics	Conditions*	Min	Typ	Max	Units
Bridge Elements					
Supply	Vbridge referenced to GND	1.8	5.0	12	Volts
Resistance	Bridge current = 5mA, VCC to GND	250	350	450	ohms
Operating Temperature	Ambient	-40		125	°C
Storage Temperature	Ambient, unbiased	-55		125	°C
Humidity	Tested at 121°C			100	%
Field Range	Full scale (FS) – total applied field	-6		+6	gauss
Linearity Error	Best fit straight line ± 1 gauss ± 3 gauss ± 6 gauss		0.05 0.4 1.6		%FS
Hysteresis Error	3 sweeps across ±3 gauss		0.08		%FS
Repeatability Error	3 sweeps across ±3 gauss		0.08		%FS
Bridge Offset	Offset = (OUT+) – (OUT-) Field = 0 gauss after Set pulse, VCC = 5V	-10	±2.5	+10	mV
Sensitivity	Set/Reset Current = 2.0A	0.8	1.0	1.2	mV/V/gauss
Noise Density	@ 1kHz, VCC=5V		48		nV/sqrt Hz
Resolution	50Hz Bandwidth, VCC=5V		85		µgauss
Bandwidth	Magnetic signal (lower limit = DC)		5		MHz
Disturbing Field	Sensitivity starts to degrade. Use S/R pulse to restore sensitivity.	20			gauss
Sensitivity Tempco	T _A = -40 to 125°C, VCC=5V T _A = -40 to 125°C, ICC=5mA	-2800	-3000 -600	-3200	ppm/°C
Bridge Offset Tempco	T _A = -40 to 125°C, No Set/Reset T _A = -40 to 125°C, With Set/Reset		±500 ±10		ppm/°C
Bridge Ohmic Tempco	VCC=5V, T _A = -40 to 125°C	2100	2500	2900	ppm/°C
Cross-Axis Effect	Cross field = 1 gauss, Happlied = ±1 gauss		+0.3		%FS
Max. Exposed Field	No perming effect on zero reading			200	gauss
Sensitivity Ratio of X,Y,Z Sensors	T _A = -40 to 125°C		100±5		%
X,Y, Z sensor Orthogonality	Sensitive direction in X, Y and Z sensors			1.0	degree

* Tested at 25°C except stated otherwise.

SPECIFICATIONS

Characteristics	Conditions*	Min	Typ	Max	Units
Set/Reset Strap					
Resistance	Measured from S/R+ to S/R-	2.0	3.0	4.0	ohms
Current	0.1% duty cycle, or less, 2 μ sec current pulse	1.5	2.0	4.0	Amp
Resistance Tempco	T _A = -40 to 125°C	3300	3700	4100	ppm/°C
Offset Straps					
Resistance	Measured from OFFSET+ to OFFSET-	40	50	60	ohms
Offset Constant	DC Current Field applied in sensitive direction	4.0	4.6	6.0	mA/gauss
Resistance Tempco	T _A = -40 to 125°C	3500	3900	4300	ppm/°C

* Tested at 25°C except stated otherwise.

The **thermometer** is a TMP36 from Analog Devices. The TMP36 is a low voltage, precision centigrade temperature sensor. It provides a voltage output that is linearly proportional to the Celsius (centigrade) temperature. The TMP36 does not require any external calibration to provide typical accuracies of $\pm 1^\circ\text{C}$ at $+25^\circ\text{C}$ and $\pm 2^\circ\text{C}$ over the -40°C to $+125^\circ\text{C}$ temperature range.

The low output impedance of the TMP36 and its linear output and precise calibration simplify interfacing to temperature control circuitry and ADCs. It is intended for single-supply operation from 2.7 V to 5.5 V maximum. The supply current runs well below 50 μA , providing very low self-heating—less than 0.1°C in still air. In addition, a shutdown function is provided to cut the supply current to less than 0.5 μA . The circuit diagram of the TMP36 is illustrated in FIGURE 4, while TABLE 2 lists the specifications of the sensor.

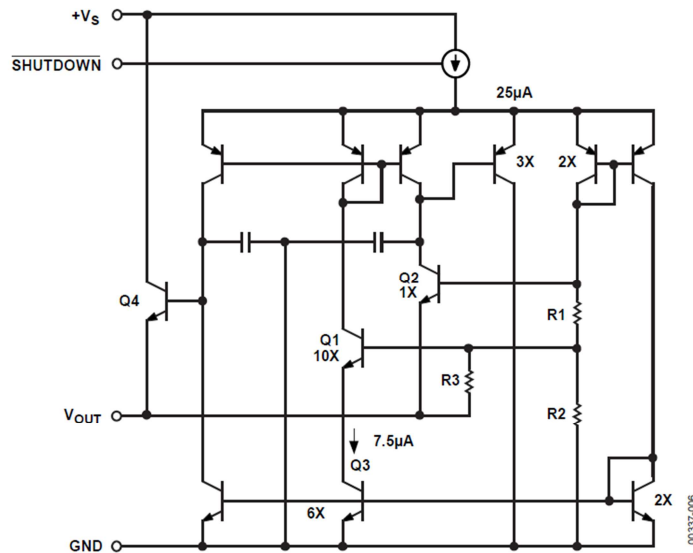


FIGURE 4. TMP36 Circuit Diagram

TABLE 2. TMP36 specifications

Parameter	Symbol	Test Conditions/Comments	Min	Typ	Max	Unit
ACCURACY						
F Grade		$T_A = 25^\circ\text{C}$		± 1	± 2	$^\circ\text{C}$
G Grade		$T_A = 25^\circ\text{C}$		± 1	± 3	$^\circ\text{C}$
F Grade		Over rated temperature		± 2	± 3	$^\circ\text{C}$
G Grade		Over rated temperature		± 2	± 4	$^\circ\text{C}$
Scale Factor		$-40^\circ\text{C} \leq T_A \leq +125^\circ\text{C}$		10		$\text{mV}/^\circ\text{C}$
		$3.0\text{ V} \leq V_S \leq 5.5\text{ V}$				
Load Regulation		$0\ \mu\text{A} \leq I_L \leq 50\ \mu\text{A}$				
		$-40^\circ\text{C} \leq T_A \leq +105^\circ\text{C}$		6	20	$\text{m}^\circ\text{C}/\mu\text{A}$
		$-105^\circ\text{C} \leq T_A \leq +125^\circ\text{C}$		25	60	$\text{m}^\circ\text{C}/\mu\text{A}$
Power Supply Rejection Ratio	PSRR	$T_A = 25^\circ\text{C}$		30	100	$\text{m}^\circ\text{C}/\text{V}$
Linearity				0.5		$^\circ\text{C}$
Long-Term Stability		$T_A = 150^\circ\text{C}$ for 1000 hours		0.4		$^\circ\text{C}$
SHUTDOWN						
Logic High Input Voltage	V_{IH}	$V_S = 2.7\text{ V}$	1.8			V
Logic Low Input Voltage	V_{IL}	$V_S = 5.5\text{ V}$			400	mV
OUTPUT						
TMP36 Output Voltage		$T_A = 25^\circ\text{C}$		750		mV
Output Voltage Range			100		2000	mV
Output Load Current	I_L		0		50	μA
Short-Circuit Current	I_{SC}				250	μA
Capacitive Load Driving	C_L	No oscillations	1000	10000		pF
Device Turn-On Time		Output within $\pm 1^\circ\text{C}$, 100 $\text{k}\Omega$ 100 pF load		0.5	1	ms

POWER SUPPLY						
Supply Range	V_s		2.7		5.5	V
Supply Current	I_{SY} (ON)	Unloaded			50	μA
Supply Current (Shutdown)	I_{SY} (OFF)	Unloaded		0.01	0.5	μA

The **susceptometer** is an induction-based device, consisting of a ferrite core with H shape. The H shaped ferrite core of the susceptometer allows perform a differential measurement, necessary for the interpretation of the data (all susceptibility data will be referred to the susceptibility of the atmosphere, practically that of the vacuum). The susceptometer ferrite core is constructed with a primary winding for the driving and a couple of secondary coils in opposition for the measurements.

The current through the primary coils (see FIGURE 5) creates a flux, which follows a U path on each of the core halves and closes through the gaps.

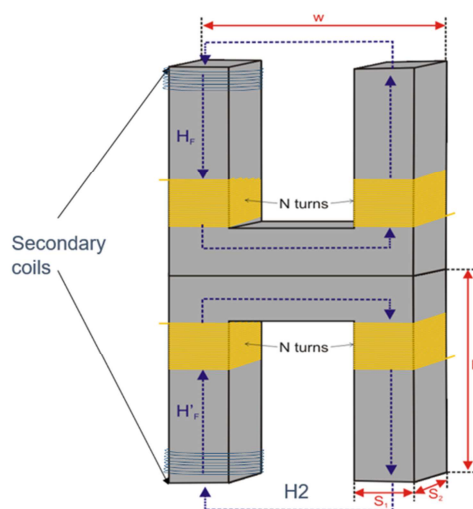


FIGURE 5. H-Core Design Diagram

A set of secondary coils are placed in two of the ferrite arms in order to pick up the electromotive force signal of the magnetic field.

Due to the nature of the magnetic field in a magnetic circuit, when a magnetic material is placed in one of the open ends of the H core, the flux lines closes through the new magnetic material and modifies:

- Electrical properties of the H core self-induction.
- Magnetic flux through the H core.

The changes in the electric and magnetic circuit behaviour are monitored and used for the determination of the magnetic properties of the approached samples. The system is sensitive to both the real and the imaginary component of the magnetic permeability (i.e. complex magnetic susceptibility).

The presence of a sample (rocks, sediments, bulk material, soils, etc.) will affects the nominal performance of the resonant electric circuit without sample.

These effects are caused by the modification of the self-inductance of the system formed by the H core and sample. This new system presents a higher value of its self-inductance. At the free end of the H core where the sample is presented, the magnetic field magnetise the material and the total reluctance of the magnetic circuit diminishes.

The electric circuit has a shift in its resonance frequency with the changes in the self-inductance. The changes of the resonance frequency for the system with and without sample can be used to determine the real value of the susceptibility of the samples. The phase shift induced in the electromotive force picked up by the secondary coils is used to determine the imaginary component of the susceptibility.

To accomplish these objectives, both H core and sample must meet a set of characteristics:

Characteristics of the H core:

- The magnetic permeability of the core material (μ_H) must be high in comparison to that of the sample or the air ($\mu_{\text{ferrite}} \gg \mu_{\text{sample}}$), in order to concentrate the magnetic flux and force the lines to follow the desired magnetic path.
- The current through the primary coils circulates in such way that, in the junction between the two U core halves, the magnetic flux vanishes. This is to avoid saturation in the case of high current circulating through the primary coils.
- Experimental studies have shown that at the working frequencies (10 kHz – 100 kHz), eddy currents on the wire do not affect the proper performance of the device. If higher frequencies are considered, then the influence of induced currents and methods to avoid them must be considered. Copper wires must be within a determined range of sizes [4].

Characteristics of the sample:

- The surface of the sample must have an area, at least, as big as the contact area of the H core.
- The depth of the sample must be, at least, as long as the penetration depth of the stray field produced by the ferrite (1 cm).
- The conductivity of the sample must be negligible.
- The permeability of the sample cannot exceed a certain value, which is in the order of the permeability of the magnetic core ($\mu_{\text{sample}} \ll \mu_{\text{ferrite}}$).

The instrument is designed to be a portable, hand-held device, with very low power consumption and capability to perform the measurement of the real component at different frequencies. In order the perform measurements at different frequencies, two possibilities could be considered:

- To modify the value of the capacitors.
- To modify the value of the self-inductance.

The modification of the capacitors values would be preferred in the terms that a modification in the self-inductance values would include modification of the characteristics of the H core, or the addition of a variable self-inductance in the circuit, affecting some performances of the susceptometer. However, given that the self-induction of the H core depends on the geometry and this is not much flexible by design, the values of the capacitors must be in a given order of magnitude to reach the desired working frequencies. These values are in the order of μF , and there are not available variable capacitors of this magnitude with the appropriate performances.

The only way to modify the resonance frequency by changing the capacitors under such conditions is to switch between different capacitors. Using a set of different selectable capacitors, the resonance frequency

can be modified discretely to preselected frequency values. This technique offers a partial solution to the problem of measuring at different frequencies but not a complete solution. To accomplish this objective, a magnetic amplifier is added to the circuit, as shown in FIGURE 6.

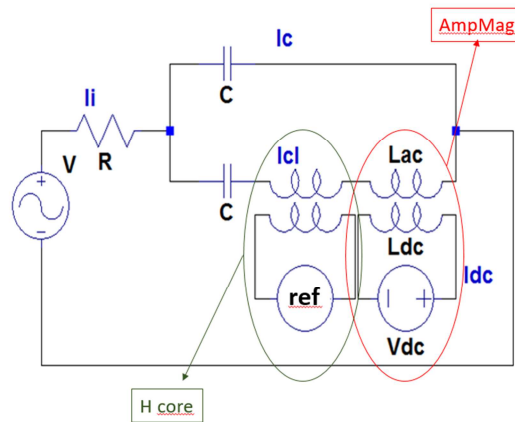


FIGURE 6. Electric circuit with Magnetic Amplifier (AmpMag).

The magnetic amplifier modifies its self-inductance by means of a controlled DC current applied to the DC loop. This allows the system to modify the resonance frequency in a continuous way. By using the combination of magnetic amplifier and proper capacitor values, the complex magnetic susceptibility can be determined in a significant range of frequencies, not affecting the power consumption of the measurement routine.

3.1. Overview and target requirements

As mentioned before, the objective of NEWTON project is to design and develop novel instrumentation to perform in-situ and combined magnetic field and susceptibility measurements during planetary exploration with rovers and spun off to Earth surveys. The final goal is to perform the complete characterization of the magnetic environment. To acquire such information, complementary measurements are needed. For example, to determine unambiguously the geometry and intensity of the magnetic moments of the source, a complete 3D vector magnetic map is required. This magnetic field map can be complemented with a gradiometric map. These measurements provide information about orientation of the field source, enhance the magnetometric results and allow the geometric characterization of the source with a 2D map, decreasing the number of magnetic field measurements.

In order to obtain information of the magnetic material, it is necessary to characterize the source by means of its physical properties. These properties are the complex magnetic susceptibility, the saturation field, the remanent magnetization and the coercive field. All these measurements are, of course, counterproductive in a field measurement, even more when talking about planetary exploration. In order to find a trade-off between number of measurements, complexity of measurement performance and the provided information, NEWTON consortium has been working on a combination of instruments for a complete magnetic environment characterization: Magnetometer + Magnetic Susceptometer.

$$\begin{pmatrix} B_x \\ B_y \\ B_z \end{pmatrix} + \chi \tag{3.1-1}$$

Following the requirements included in D3.1, TABLE 3 and TABLE 4 have been updated to represent the final operational and environmental target requirements for prototype 1.

TABLE 3. Common design operational requirements for prototype 1.

ELECTRICAL CHARACTERISTICS	
Power supply (W)	≤1.5 TBC
Voltage (V)	$5.00 \leq V \leq 5.40$ TBC
Ripple voltage (mVpp) (f: 0 - 30 MHz)	150
MAGNETIC CHARACTERISTICS	
Susceptibility Range (χ)	$10^{-6} \leq \chi \leq 10^3$ TBC
Frequency Range: f(kHz)	$10 \leq f \leq 100$ TBC
Magnetic Field, at 3 cm from head: B(μ T)	$30 \leq B \leq 300$ TBC
Resolution	$1 \cdot 10^{-6}$
Sensitivity	$1 \cdot 10^{-6}$
Noise	$2 \cdot 10^{-7}$
Sensitivity Temp. Coeff.	1 % FS
Magnetic field dynamic range	± 200 μ T
Magnetic field resolution	1 nT
Bandwidth	10 Hz
Stability	1 ‰
PHYSICAL CHARACTERISTICS	
Head Dimensions maximum (mm)	70 x 40 x 85 mm
Mass (g)	≤400 TBC

As already described, the architecture of NEWTON instrument is divided into three blocks: the power and control units will be allocated inside the rover body, and the Sensor Unit will be deployed to ground. Therefore, the environmental requirements are only applicable to the sensor unit. TABLE 4 shows the environmental requirements for the SU of prototype 1. Environmental requirements have been extracted from Exomars 2020 mission. With this regard, a set of tests have been carried out in representative prototypes to verify the resistance of the susceptometer components to the space environmental conditions.

TABLE 4. Design requirements for the SU of prototype1.

TEMPERATURE	
Operating: T(°C)	-40 ≤ T ≤ 110 TBC
Storage: T(°C)	-150 ≤ T ≤ 80 ; Relative humidity ≤ 90 % TBC Air cleanliness class at least 8 of ISO to GOST ISO 14644-1-2002
ENVIRONMENTAL	
Vibration	Low-sine sweep: 5Hz to 2000 Hz at 2 oct / min 0.5g for each axis (worst case) Random: f = 5 - 2000 Hz 0.197 g ² /Hz (worst case) The instrument must not have resonant frequencies less than 40 Hz (Exomars 2020 launcher requirement).
Thermal vacuum	Storage: Cycles from -130°C to 65°C, 10 ⁻⁶ mbar Functional: Cycles from -55°C to 65°C, 10 ⁻⁶ mbar 4 cycles
RADIATION	
Components	Flight model (rad hardened capacitors and resistors) immune to radiation.

3.2. Detailed Design

3.2.1. Ferrite H core design

The sensor head is based, as mentioned, on a magnetic core with a H shape, a set of excitation coils and a set of pick up coils.

The magnetic core is made of ferrite. The ferrite material is selected because of its performance in terms of real permeability and losses. The relative permeability is in the range of $\mu_r = 2000 - 2300$ [IS]. This is a high value in comparison with the expected values for natural samples, selected because of two reasons:

- A high permeability values ensures a high magnetization and concentration of the magnetic field created by the core in the desired area.
- The flux lines are always conducted through the same path and this allows a comparison between the different samples and measurement scenarios.

Some measurements are based on the changes of the self-inductance of the H-core, and the higher is the value of its permeability with respect to that of the sample, the smaller is this change, affecting the sensitivity of the instrument. However, due to the high stray field produced by the ferrite core, the demagnetization factor decreases the permeability of the core and compensates the high permeability of the material. These conditions constrain the self-inductance value of the H-core to values around 50 - 60 μH , for cores of the declared sizes and materials, and primary coils of 10 turns/arm. Two materials have been used as cores of the ferrites [4]: Ferrite 1 - Manifer 198 by Tridelta™ and Ferrite 2 - 3C90 by Ferroxcube™ (FIGURE 7).

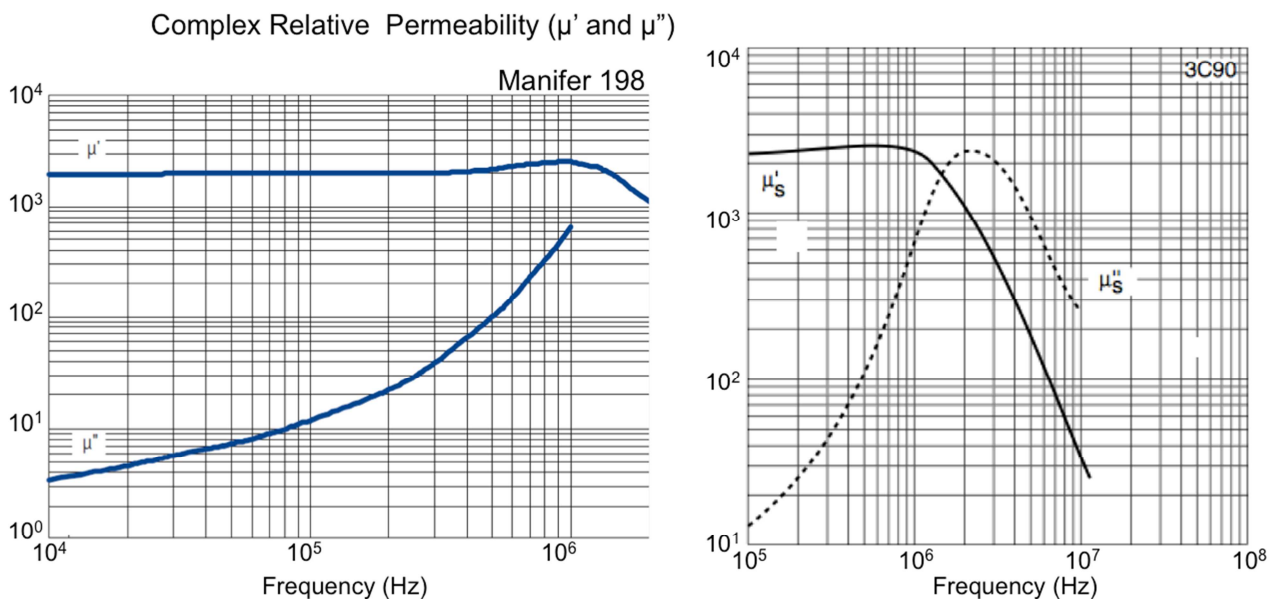


FIGURE 7. Complex relative permeability as a function of the frequency for the two materials used: Manifer 198 by Tridelta™ (left) and 3C90 by Ferroxcube™ (right).

The two selected ferrite cores have been exhaustively proved in different prototypes showing good performances. One of these materials have been also submitted to environmental tests and analysed by VSM in a representative range of temperatures. The results can be seen on section 3.4.

The sellers provide different sizes of U cores, which are used to manufacture the H core. There is a slight change in the size of the two cores considered. The U cores are fixed forming the H shape. The magnetic

flux in each U core must be independent from the flux in the other U core. The geometry and the permeability of the core ensure this condition. Besides that, a set of test were performed to verify the independence. The tests consisted of the introduction of different number of layers of high ferromagnetic (Permalloy) and conductive diamagnetic (copper) in the junction between the U cores. The analysis of the induction in one of the cores while a high magnetic field was induced in the other, and the comparison with the nominal situation without any layers shows minimum interaction. Simulations with AMPERES/COMSOL were also conducted. The model and experimental results verify that the flux induction on each U-core halves was, in the worst case, below 1% of the total magnetic flux induced in the other U-core. The U-cores can be considered independent in terms of magnetic induction and the only interaction between them comes from the common primary coil.

The primary winding is made of enameled copper wire. A unique wire is used to coil the four arms of the ferrite core in the following way:

- On each U half, the flux lines follow a U path which closes through the air in the outer face.
- In the junction between the U halves, the flux must flows counter-wise between upper and lower U halves. This not only enhances the independence of each U half from the other, but also ensures that, in the case of high magnetic induction (high current through the wire), the flux vanishes in the junction instead of adding.

In the case of independent primary coils on each arm of the core, the winding must be connected in the described way. The type and dimensions for the primary winding wire is described in D3.1 [4]. The diameter of the wire must be between 0.4 mm and 1 mm, monofilament enameled copper wire. The estimated length of the total wire would be around 1 meter maximum, with a total resistance of 0.2 Ω .

The secondary windings are placed on two arms of the ferrite, one in the upper part and the other in the lower part, in the same lateral side of the H core (FIGURE 8). The secondary coils are independent one from each other. The secondary coil on the side presented to the sample (active coil) is measured by a lock-in amplification, and the other secondary coil is presented always to the air (passive coil), and it is measured by a lock-in amplification, using this result as a reference point. These secondary coils pick up the electromotive force induced by the magnetic induction in the ferrite core. When a sample is presented, the performance of the device experiences two main disturbances:

1. The amplitude of the magnetic induction increases in the part of the core presented to the sample (paramagnetic / ferromagnetic), and the electromagnetic force induced in the corresponding pick-up coil increases. When the system works at the resonance frequency, the increase in the electromotive force on this secondary coil is related to the real component of the magnetic susceptibility of the sample. However we must be careful and notice that the self-induction is changing, and so does the current through the primary coil. The measurement in the passive secondary coil provides a good reference measurement of this disturbance and improves the accuracy of this measurement.
2. The magnetic induction set on the sample experiences a delay due to the imaginary component of its magnetic susceptibility. This produces a phase shift between the magnetic induction in the magnetic circuit formed by the susceptometer core and sample and the current through the primary coil. When the circuit is taken out of its resonance frequency, the inductance (L) modifies, and there is a shifting of the current, i.e. there is a phase difference. To avoid this, the magnetic induction is picked up by the active secondary coil and the reference signal is achieved from the passive coil, which is the best reference to the current through the primary coil in the scenario with sample. The phase shift produced by the sample can be calculated with a differential measurement and it is proportional to the imaginary component of the magnetic susceptibility of the sample.

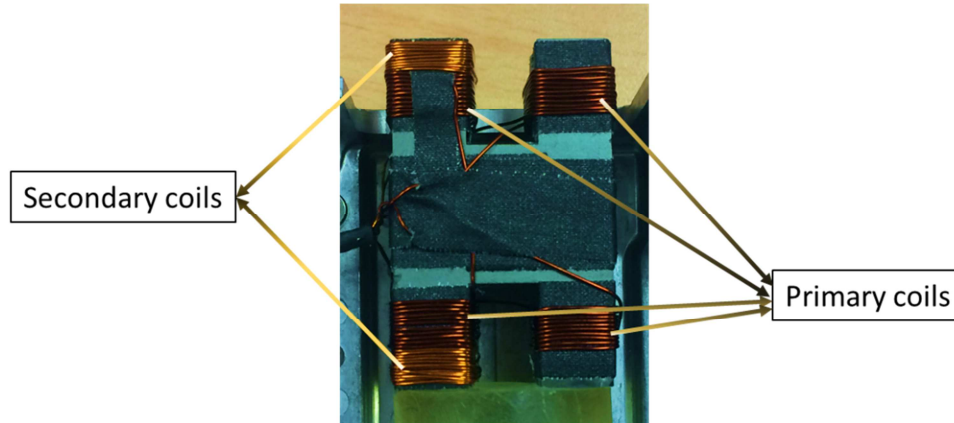


FIGURE 8. H-core winding image.

The measurement of the phase shift in the electromotive force is performed preferably at the resonance frequency of the system with sample. On the one hand, at this frequency the ratio current through the primary coil – power consumption is optimal. On the other hand, at this working point the phase shift between active and passive can be better refereed as the electrical circuit is optimized.

The secondary windings are coiled near the free ends in the left (or right) upper and lower arms of the ferrite. They are made of monofilament copper wire of a maximum diameter of 0.5 mm (current diameter: 0.2mm). They should be made of a number of turns around 20 turns, and connected to high impedance inputs in order to avoid mutual inductance. The number of turns on each secondary coils must be adjusted to minimize the differential measurement. This can be done by calculating experimentally the product of $N_{sec} \times N_p$, in the upper and lower halves of the H-core and adjusting the number of turns in the secondary coils until this product is as close as possible.

3.2.2. Magnetic Amplifier design

The magnetic amplifier is introduced to have a varying self- inductance in the resonant circuit and use this variability to tune the resonance at different frequencies in prototype 1. Prototype 2 will be tuned at a single frequency by design [2].

The design of the magnetic amplifier is based on a couple of toroidal ferrites coiled with a double winding. The proposed toroidal ferrites are of $\varnothing 16 \times \varnothing 9.6 \times 6.3$ mm and the material is 3E25, manufactured by FerroxCube, with a relative permeability of $\mu_r = 5500$ [IS].

The toroidal cores constitute a magnetic circuit with the double winding (FIGURE 8): one winding carries AC current, the other winding is connected to a DC power supply which injects DC current into the winding. This current changes the permeability of the core in such a way that it can modulate the amplitude of the AC current for a certain power supply. In NEWTON design, the DC current is used to change the permeability and therefore, the self-inductance and its resonance with the capacitors. FIGURE 9 shows the scheme of the resonant circuit with the magnetic amplifier. The windings are made of monofilament enamelled copper wire of 0.3mm diameter. The DC loop is constructed with $N_{DC}=45$ turns and the AC loop have $N_{AC}=5$ turns.

The self-inductance of the magnetic amplifier must be around $L=315 \mu\text{H}$ (no current through DC loop) for the proposed H-core geometries and characteristics. With this value, it can be achieved variations in the resonance frequency up to 40 kHz within the range of 10 kHz – 100 kHz, only varying the DC current from 0 mA to 300 mA. This value can be tuned for different H-core developments.

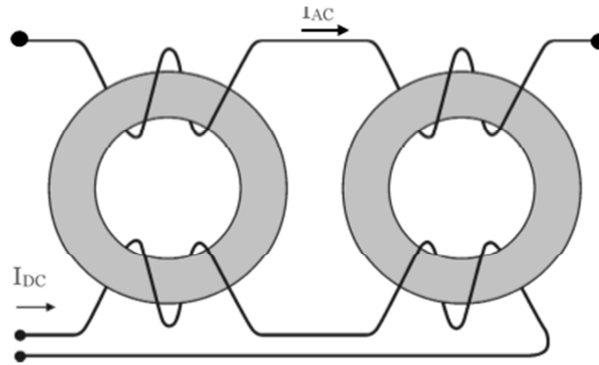


FIGURE 9. H-core diagram.

The presence of the magnetic amplifier in the circuit implies a number of consequences on its performance and capabilities, which are reflected in the measurement techniques and its accuracy. First of all, the magnetic amplifier is connected in series with the ferrite H-core and their self-inductance values add ($L_{Total} = L_H + L_{AmpMag}$). L_{AmpMag} depends on the current through the DC loop, and the variation in the current implies the modification of L_{Total} . This characteristic allows the system to tune different working frequencies (electrical resonance frequencies).

The disadvantage of using the magnetic amplifier is that the resonance frequency shift decreases as the value of self-induction increases. This affects the resolution and sensitivity of the technique, and the precision with which it can be found the resonance frequency with sample.

The advantages, however, are numerous and valuable:

- We can measure at different frequencies in a continuous range of frequencies, as shown in D3.1 [4], which is of high interest especially for the imaginary component.
- The measurements in the secondary coils are not affected by the presence of the magnetic amplifier or its saturation state, and this method is not affected in terms of resolution, sensitivity, range or precision.

Nevertheless, given that it is recommendable to work at the resonance frequency with sample when measuring in the secondary coils, and that this type of measurement do not offer a good resolution in frequency, a combined measurement technique ($R_{in} +$ secondary coils) is used for the optimum performance of the device. Thus, in spite of the disadvantage, very good results and redundant measurements are obtained for the real susceptibility, both when measured without a magnetic amplifier, and with a saturated amplifier or near saturation. Measurement in the secondary coils provides an excellent measure of the imaginary component in both scenarios and a redundant measure of imaginary susceptibility, whatever the state of saturation of the magnetic amplifier.

3.2.3. Electrical Resonant Circuit design

The susceptometer system consists, not only on the H-core and the magnetic amplifier, but also of a modified tank circuit (FIGURE 10), in which it is included the ferrite core and magnetic amplifier ($L = L_H + L_{AmpMag}$) as a self-inductance in the resonating loop. The circuit is composed by the inductance (L) in series with a capacitor (C_2) and both in parallel with a capacitor C_1 . In the present design: $C_1 = C_2 = C$.

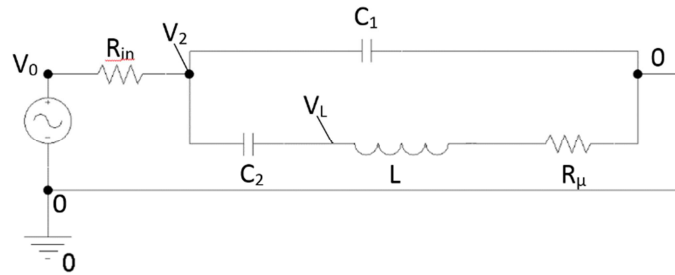


FIGURE 10. Modified tank circuit scheme.

This circuit has two resonant frequencies, which were discussed in D3.1 [4]:

$$f_{o1} = \frac{1}{2\pi\sqrt{LC}} \quad (3.2-2)$$

$$f_{o2} = \frac{1}{2\pi} \cdot \sqrt{\frac{2}{L \cdot C}} \quad (3.2-3)$$

In the second one, f_{o2} , it is achieved an optimum ratio between the current circulating in the resonant loop and the input current. This guarantees a moderate to high current in the circuit with low power consumption from the power supply. The resistor is a non-inductive ceramic component for high power load. This ensures no phase shift produced in the resistor and very low heat dissipation. The capacitors are Polypropylene/Polyester layer capacitors, or metallized Polypropylene, with capacitances from 0.15 μF up to 4.7 μF . These components are of high temperature stability and low AC impedance, with high AC voltage capabilities. All components are selected to induce a minimum uncontrolled phase shift in the circuit, and to have good temperature stability.

3.3. Functional Verification

The system has been extensively tested in terms of performances. A set of natural and synthetic samples have been measured and used as preliminary calibration of the system, showing good performance. Some results are presented on deliverable D3.1 [4], where it can be seen a very good performance for the determination of the real susceptibility.

On the following it is presented the calibration and measurement procedures for the real and imaginary components. Two complementary techniques will be used, each with different applications and performances:

- 1- Frequency shifting. Measurement on the input resistor R. Real susceptibility only.
- 2- Magnetic flux variation. Measurement on the secondary coils. Complex susceptibility.

3.3.1. Measurement on the input resistor

This measurement was detailed in D3.1 [4]. When the H-core is presented to a sample, the self-inductance of the system modifies. The values of the resonance frequency of the circuit with and without sample are used to determine the real component of the susceptibility of the sample. The resonance frequency values obtained with this method are used in the other technique as working points.

The resonance seeking procedure is as described in D3.1 [4], with a minor modification in the data processing to improve the resolution.

Prior to the sample approach, the circuit is symmetric, being the four free ends of the ferrite in contact to the air. In this configuration the resonance frequency is determined when the input current (determined as $I_{in} = (V_0 - V_s)/R_{in}$ measuring the difference of voltage) is minimized during the sweep. The phase in this

condition is set as the zero phase (reference phase). When the sample is approached to the ferrite closing one of the magnetic circuits, the resonance frequency is determined because it zeroes the phase, i.e. in the new resonance frequency, which is possible when the relative permeability of the sample is much smaller than that of the ferrite core ($\mu_{r \text{ sample}} \ll \mu_{r \text{ ferrite}}$). This is a reasonable approximation when measuring natural samples and the manufactured samples prepared for the calibration. The amplitude and phase values are recorded during the frequency sweep performed for the determination of the resonance frequency with the sample. Later, in a close range around the minimum amplitude value, the recorded data is fitted to a parabola and the resonance frequency can be determined more accurately by means of this math processing.

The real component of the susceptibility can be determined using the two resonance frequency values using formula (3.3-4):

$$\chi_s = \frac{f_0^2 - f_1^2}{f_1^2 - \frac{l_f}{2\pi^2 N^2 C S_f \mu_f}} \quad (3.3-4)$$

3.3.2. Measurement on the secondary coils

The modification of the flux amplitude and phase is a very good measurement in terms of stability, given that it is not affected by the presence of the magnetic amplifier. Moreover, the measurement in the secondary coils offers an excellent and straightforward measurement of the imaginary component of the susceptibility by using a lock-in amplification of the electromotive force.

As described in D3.1[4], the effect of the rock or soil approaching the H-core changes the magnetic induction and therefore, the electromotive force (ε), which can be picked up by the secondary coils. This measurement in amplitude and phase of the magnetic induction in the ferrite arms provides information about the magnetic properties of the sample under measurement.

The permeability is derived from the measurement of the difference in the magnetic flux in the secondary coils. In this case the theoretic are simpler but the results are more complicated due to the complex contributions of the different factors taken into account. The objective is to relate the electromotive force induced in the secondary coils, easily measured with a lock-in amplification given that the excitation is a sinusoidal magnetic field, with the magnetic susceptibility of the sample under measurement.

The procedure, as described in D3.1 [4], is to determine the magnetic flux within the secondary coils by means of the solution of the magnetic circuit, and then relate it with the magnetic susceptibility using the relation between magnetic field and magnetic induction.

A relation which relates directly the amplitude of the voltage difference in the terminals of the secondary and the real susceptibility emerge from these calculations. A simplified version of this expression is the following:

$$\varepsilon = \omega \cdot N_s \cdot S \cdot \mu_f \left(\frac{N_p \cdot I \cdot \mu_f}{\mu_f \cdot l_i + \mu_i \cdot l_f} \right) \quad (3.3-5)$$

Where N_s and N_p are the number of turns of the secondary and the primary coils respectively, S is the cross-section area of the secondary, I the current through the primary, l_s and l_i are the length of the path of the magnetic flux in the ferrite and in the air/soil, and μ_f and μ_i the real permeability of the ferrite and the air/soil respectively.

From this relation it can be solved the real permeability of the sample and thus, the real magnetic susceptibility. This relation shows the dependences of the measured value with the susceptibility, but as

mentioned before, a calibration on the device is mandatory in order to obtain an absolute value of the magnetic susceptibility.

For the best resolution, differential measurement with two lock-in amplifiers is performed. Using the difference between the active and passive secondary coils, the changes in the magnetic induction produced by the presence of the sample can be directly determined, and the amplitude, at the resonance frequency with sample, can be related with the real part of the susceptibility.

For the imaginary component, it is used the phase shift between the active and passive secondary coils. On the one hand, the ε in the passive coils experiences a $\pi/2$ phase shift with respect to the field induction (B) in the passive half of the ferrite, and a π phase shift with respect to the current (considering negligible dissipation in the wire and ferrite core). On the other hand, the magnetic induction in the active half of the ferrite experiences a phase shift (ϕ) proportional to the dissipation in the sample (imaginary component of the susceptibility). Considering negligible (or equal) the dissipation produced by the ferrite core and the wires in the active and passive halves, the imaginary component of the susceptibility can be related to the phase shift and the real component of the susceptibility of the sample using the following relations.

The magnetic induction, magnetization and permeability are described as follows.

Magnetic induction:

$$B = \mu \cdot H; \quad (3.3-6)$$

magnetization:

$$M = \chi \cdot H; \quad (3.3-7)$$

and permeability:

$$\mu = \mu_o \cdot (1 + \chi) \quad (3.3-8)$$

Taking into account these formulas, we have:

$$\phi_\mu = \tan^{-1}\left(\frac{\mu''}{\mu'}\right) = \tan^{-1}\left(\frac{\chi''}{\chi'+1}\right) = \phi_B - \phi_H = \phi_A - \phi_B = \Delta\phi \quad (3.3-9)$$

The phases ϕ_A and ϕ_B are the measurements taken from lock-in A and lock-in B respectively. We know the phase difference ($\Delta\phi$) by measurement and to find the imaginary susceptibility (χ'') we have to measure previously its real part (χ')

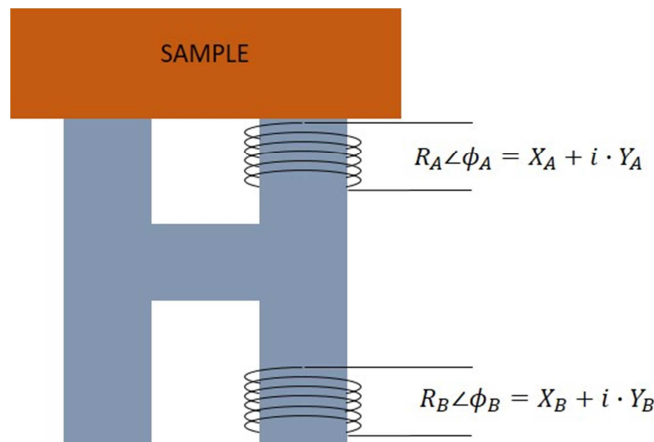


FIGURE 11. Schematic of ferrite H-core with secondary coils. Upper coil (Φ_A) represents de active coil. Lower coil (Φ_B) represents de passive coil.

Measurements of susceptibility ($\chi = \chi' + i\chi''$) are shown in TABLE 5, for different artificial test samples, when it is applied the double lock-in measurement technique.

TABLE 5. Susceptibility measurements (Imaginary not calibrated).

Freq=13635 Hz	χ' [IS]	χ'' [IS]
SAMPLE 1	1.09×10^{-1}	3.29×10^{-3}
SAMPLE 2	1.18×10^{-2}	3.00×10^{-4}
SAMPLE 3	1.17×10^{-2}	8.82×10^{-5}
SAMPLE 4	8.71×10^{-3}	1.06×10^{-4}

3.4. Preliminary vibration and ambient tests

NEWTON susceptometer Prototype 1 is design to be placed on board a rover during planetary exploration. Space missions are exigent environments, in which all instruments must met a set of requirements of dependability, robustness and reliability under extreme conditions. These conditions are highly dependent on the type of mission: interplanetary, orbital, lander, rover, or mixed are some examples of the different types of space missions. Furthermore, different planets, orbits or trajectories, implies different requirements that all instruments must met. All these circumstances lead to a wide range of possibilities in terms of requirements, depending on many factors that must be analysed for each mission and for each instrument.

NEWTON prototype 1 is designed for Martian system vehicles, where three environmental factors are critical in the design of the susceptometer head: temperature, vacuum and vibrations. The susceptometer, so far tested at Earth laboratory conditions, must face storage and functional conditions which may affect its structural integrity and utilization performance. The validation of the design under space missions' conditions is carried out by means of a battery of tests in which such conditions are recreated. These tests, named qualification tests in the frame of a space targeted project, are carried out applying certain levels and tolerances that are defined by those responsible for each mission and instrument.

NEWTON project does not have to be compliant with any specific vibration or ambient requirements. However in order to validate the design and to prove the TRL, prototype 1 has been submitted to vibration and thermo-vacuum tests. As representative values, Exomars 2020 qualification levels regarding vibration and thermal vacuum tests for rover and lander platform instruments have been applied. In the following it is summarised this preliminary testing process, as part of the design validation.

3.4.1. Vibration test

The aim of this campaign is to perform a structural and mechanical validation of the design. Specifically, this campaign is conceived as a development test of the NEWTON prototype 1. Current engineering model of prototype 1 (FIGURE 12) is structural and mechanically representative of the Sensor Head Unit, with envelope dimensions 126x80x75 mm and a weight of 800 g, being fully functional.

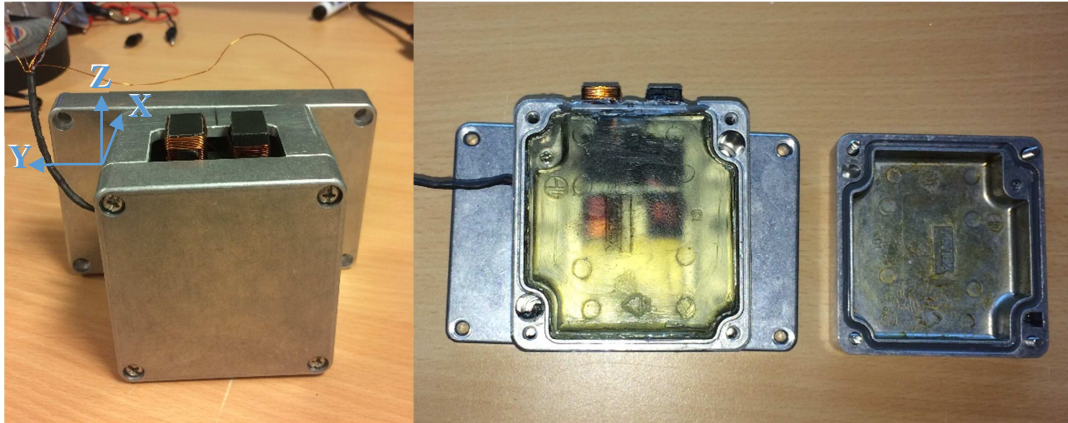


FIGURE 12. Engineering Model for vibration test.

The casing for the testing is a RETEX box (Series 68, ENAC-GdAlSi12 (Fe) DIN1706), and the instrument has been totally filled with epoxy (Royapox 5050) as foreseen in the final design.

Test definition and conditions of test

1. Electrical and functional verification procedure prior and post test
2. Test procedure
 - a. Low sine

To characterize the model and to evaluate if any of the mechanical properties of the assemblies have changed, in each axis a low-level sine (and visual inspection) will be performed before starting the test (random). The conditions for the low level sine are presented in TABLE 6.

TABLE 6. Low Level Sine.

f (Hz)	Level Sweep Rate
5-2000	0.5 g – 2oct/min (one sweep up)

- b. Random vibration

A random vibration test can be correlated to a life cycle. Since random vibration contains all frequencies simultaneously, all product resonances will be excited together which could be worse than exciting them individually as in sine testing. In this campaign, the duration of the test run is 120 seconds for the following qualification levels. The random environment is defined in the TABLE 7 below:

TABLE 7. Random test levels applicable to NEWTON prototype 1 engineering model.

f (Hz)	ASD (G²/Hz)	dB	OCT	dB/OCT	AREA	Grms
20.00	0.0390	*	*	*	*	*
50.00	0.0770	2.95	1.32	2.23	1.76	1.33
100.00	0.0970	1.00	1.00	1.00	6.15	2.48
200.00	0.1930	2.99	1.00	2.99	20.65	4.54
500.00	0.1970	0.09	1.32	0.07	79.24	8.90
1000.00	0.0580	-5.31	1.00	-5.31	132.25	11.50
2000.00	0.0290	-3.01	1.00	-3.01	172.45	13.13

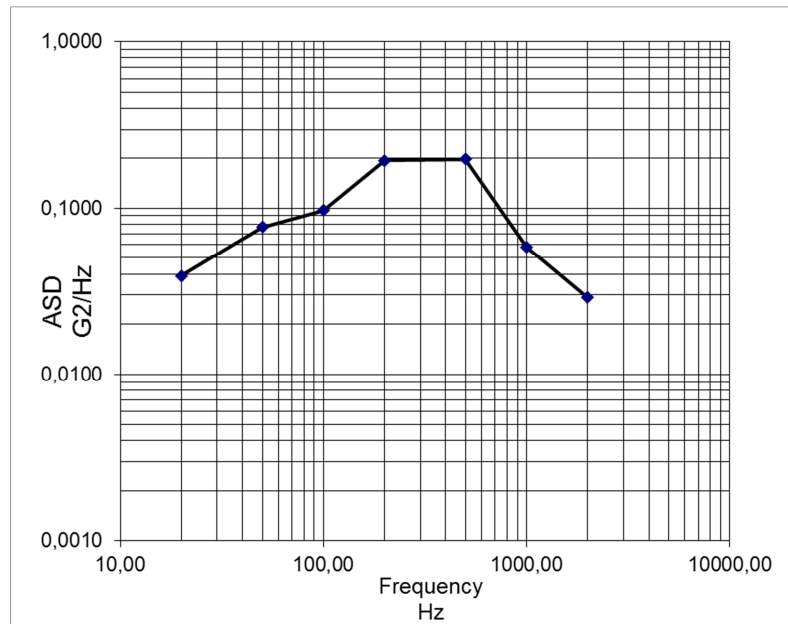


FIGURE 13. Random Vibration (120 s – 13.13 Grms)

The test facility and instrumentation main characteristics are summarized in TABLE 8.

TABLE 8. Test facilities and Instrumentation.

NAME	UTILITY
Vibration Systems: Shaker LDS 984: head and Horizontal slip table.	Dynamic Load Application: Vibration.
Control triaxial accelerometers.	Acceleration input control at the Interface fixture – EUT.
PCB lightweight triaxial accelerometers	Frequency response of the unit.

3. Validation criteria:

C1. No failures in the specimen's integrity are detected during the hardware visual inspections.

C2. Sine profile is reproduced before and after random vibration.

C3. Results after the test have a deviation respect to initial data lower than 10 % in resonance frequency, which correspond to deviations lower than 10 % in the results.

4. No clean conditions are needed.

5. No planetary protection protocol needs to be implemented.

Test results

- R1. According to C1, visual inspections performed before and after the tests show no changes in the prototype.
- R2. Integrity is demonstrated according to C2. The low sine sweep provided the vibration modes spectrum of the model in the different axes, as shown in FIGURE 14, FIGURE 15 and FIGURE 16, before and after test.

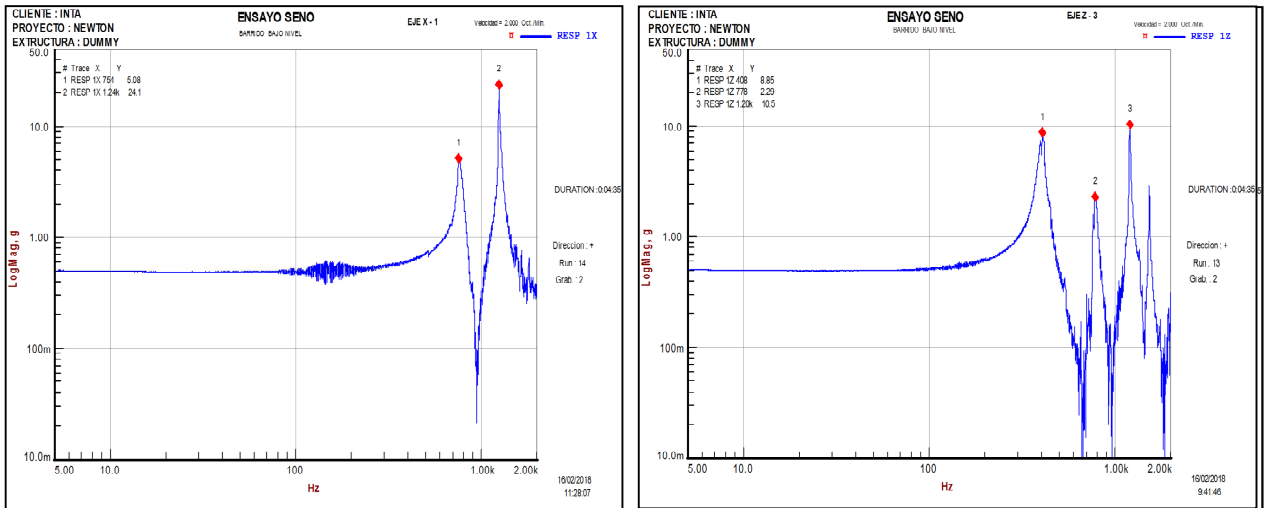


FIGURE 14. Low-sine profile. X axis. Left: before test. Right: after test.

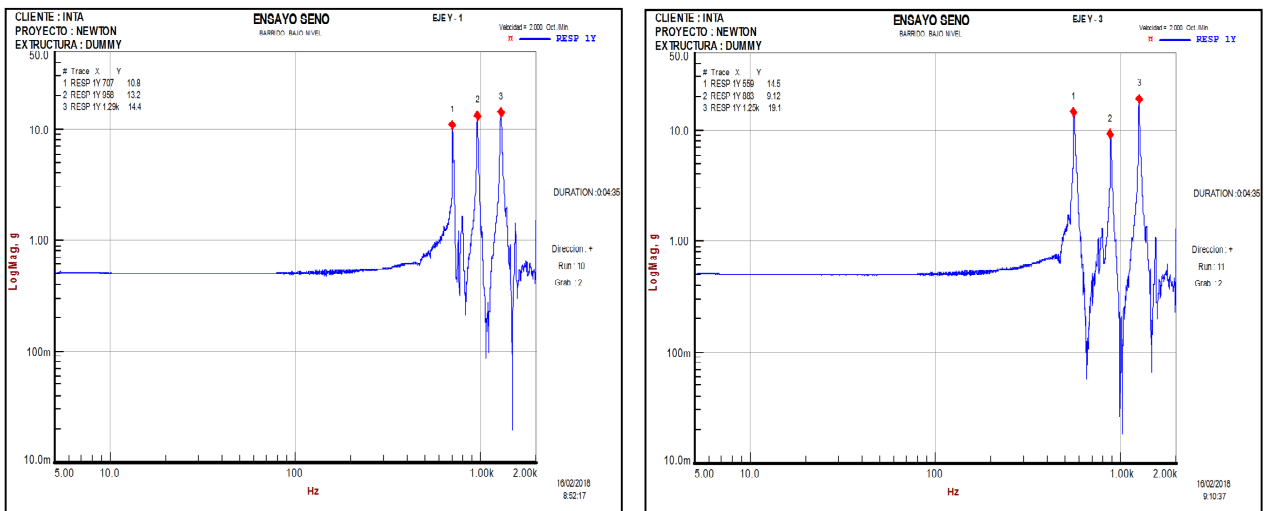


FIGURE 15. Low-sine profile. Y axis. Left: before test. Right: after test.

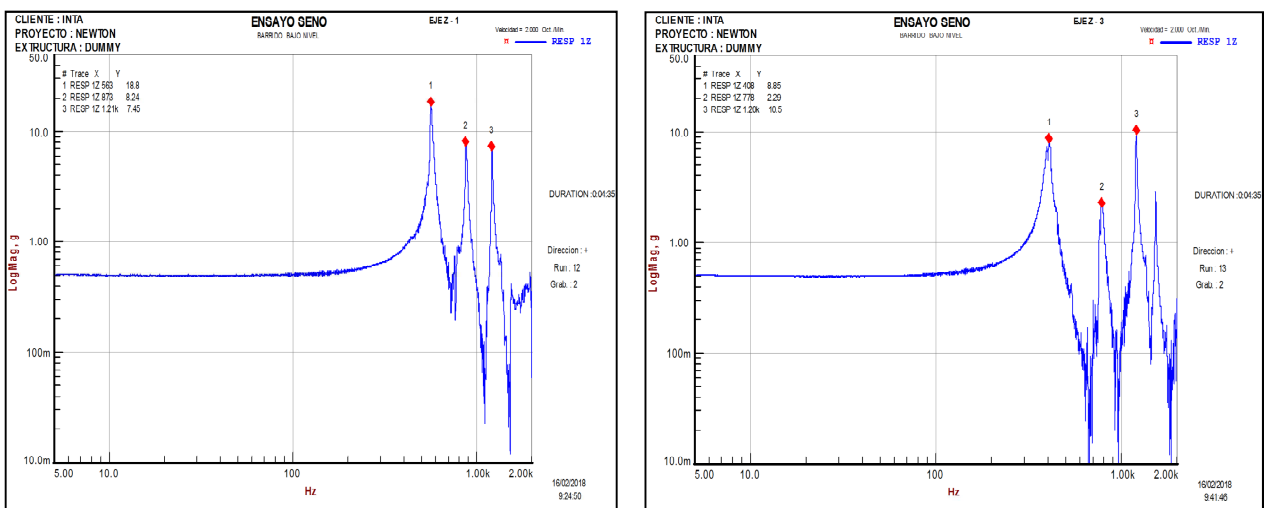


FIGURE 16. Low-sine profile. Z axis. Left: before test. Right: after test.

In all cases the low sine profile of the instrument is reproduced before and after the test except for the X axis (FIGURE 14). However, visual and functional verification of the device after the vibration in this axis were successful. The investigation done to analyse this abnormal behaviour reached the following conclusion: The X axis was the last to be tested, and during this test, two of the four screws that fixed the model to the test set-up loosened (FIGURE 17). This caused the modification of the profile, which is not attributed to the integrity of the model.

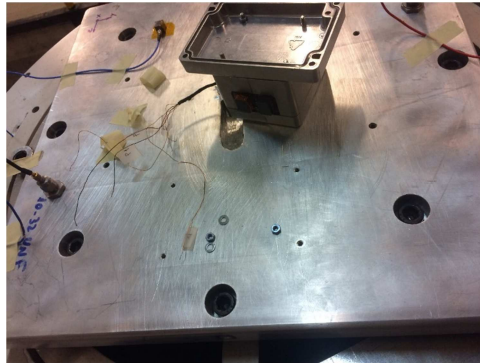


FIGURE 17. Image of the model and vibration interface after test. It can be seen that two of the screws and washers are loose and had fallen in the vibration set-up.

- R3. Functional verification of every axis do not show changes in behaviour according to C3.

TABLE 9 summarises the test results:

TABLE 9. Compliance matrix for vibration test.

Verification method	Axis	DEVIATION (Y/N)	Pass / Fail (✓/X)
Visual inspection	X	N	✓
Functional verification		N	✓
Low-sine profile		Y	✓
Visual inspection	Y	N	✓
Functional verification		N	✓
Low-sine profile		N	✓
Visual inspection	Z	N	✓
Functional verification		N	✓
Low-sine profile		N	✓

3.4.2. Thermal-Vacuum Test (TVT)

The sensor head of prototype 1 engineering model was submitted to a thermal cycling in vacuum up to representative temperatures of storage and operation in the Martian environment (with the use of heaters) to validate the building blocks fruit of the innovation of NEWTON project. The electronic units are being developed with components which are not qualified but that are equivalent to qualified components. Therefore, the electronics in these cases is considered robust by design.

Test definition and conditions of test

1. Test procedure: Temperature profile consists of 4 cycles being each cycle schemed in FIGURE 18. + 65 and – 45 °C are considered operation temperatures, and therefore it is included verification in these steps. – 135 °C is considered storage temperature and the unit is driven to this temperature but there is not verification in the step.

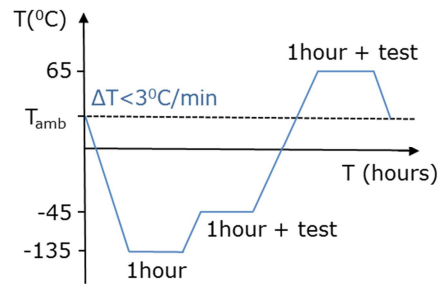


FIGURE 18.Temperature cycle for TVT.

2. Vacuum conditions: $1 \cdot 10^{-6}$ mbar.
3. Validation criteria
 - C1. Absence of changes in visual inspection
 - C2. Functional verification is performed with ad hoc calibration samples consisting of a metglas stripes core coiled and driven at different currents to simulate different permeability materials. Results after the test have a deviation respect to initial data lower than 10 % in resonance frequency, which correspond to deviations lower than 10 % in the calibration.
 - C3. Deviations in behavior in the different operative steps are lower than 10 %.
4. No clean conditions are needed.
5. No planetary protection protocol needs to be implemented.

Test results

- R1. The model does not present visible changes after the cycling.
- R2. Tests prior and after the cycling are in good agreement according to C2.
- R3. Temperature verification under equivalent conditions provided results with a deviation lower than stated in C3.

TABLE 10 summarises the test results:

TABLE 10. Compliance matrix for TVT.

Verification method	Cycle	DEVIATION WITHIN ESTABLISHED MARGINS (Y/N)	Pass / Fail (✓/X)
Functional verification	1	--	✓
Functional verification	2	Y	✓
Functional verification	3	Y	✓
Functional verification	4	Y	✓
Functional verification after test	--	Y	✓
Visual inspection after test	--	Y	✓

3.4.3. Conclusions of preliminary tests

Preliminary vibration and ambient tests performed in prototype 1 engineering model have been successful. The sensor head has been proven to stand representative qualification levels of a planetary mission and therefore, the design is considered to be validated for a TRL 6.

Even though NEWTON does not target a qualified instrument, the successful tests of the design permit to guarantee its correct behaviour in the frame of a planetary mission as for instance to Mars.

3.5. Magnetometer position

The magnetometer position has been determined studying the optimal position by means of simulations using the Multiphysics software ANSYS, concretely with the Maxwell Modulus. There are restrictions on the location of the magnetometer within the structure of the prototype, constrained by the maximum dimensions of the device. Within this constrains, it will be considered the optimum position for the magnetometer simulating the distortion of the magnetic field produced by the ferrite core. The simulations are restricted to close distances from the H-core. First of all, the magnetic field was simulated around the H-core and a region with minimum distortion was selected. The differences on the magnetic field were analysed along the different axis, in various positions, as it can be seen in FIGURE 19. To determine the final position, all these analysis has been considered, also the restrictions in the position. The optimum position of the magnetometer is: $[x, y, z] = [5.05 \text{ mm}, 6.05 \text{ mm}, -2 \text{ mm}]$ measured from the exterior superior corner of any H superior's arm. This solution reflects a trade-off between: the minimum distance between devices (H-core and magnetometer), and minimum distortion of the magnetic field produced by the ferrite core.

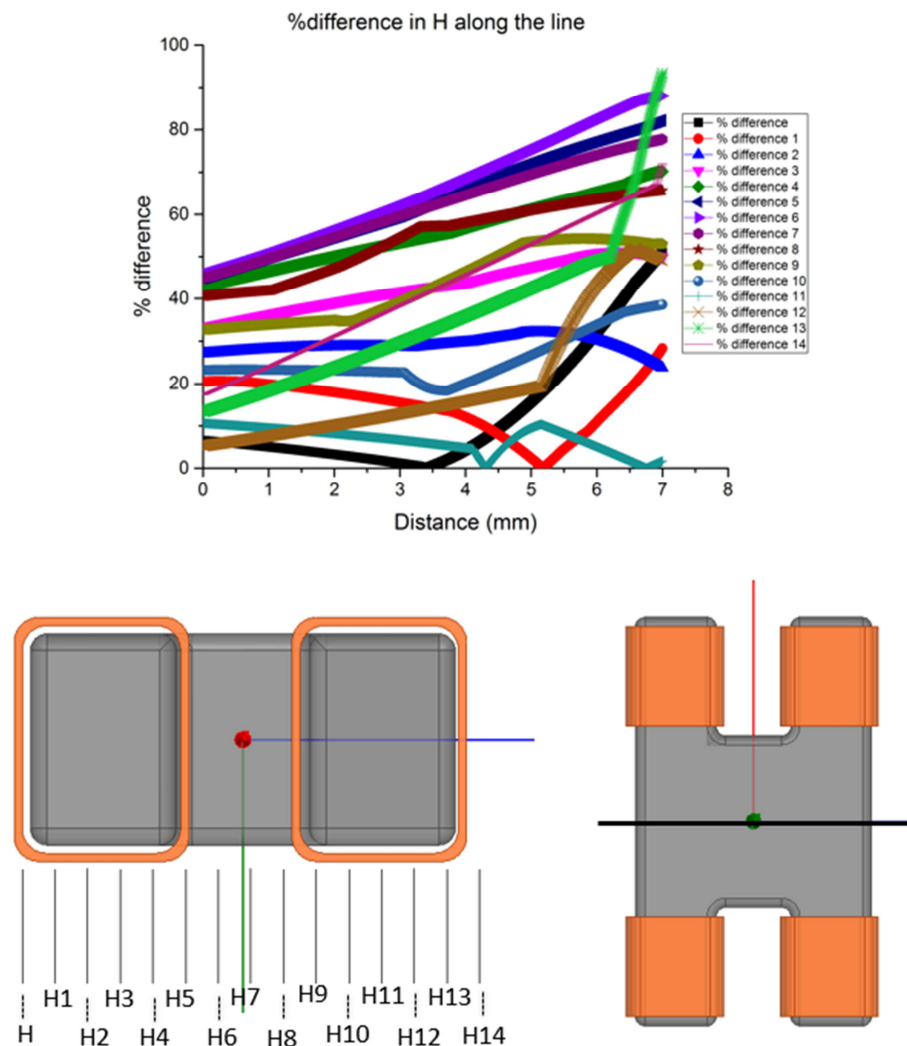


FIGURE 19. Up: Magnetic field distortion (in % comparing with field without ferrite core) along 15 lines in the plane $XY=0$. Down left: Lines distribution in the plane XY . Down right: Dark line represents the plane containing the lines. An analogue process is used to determine the magnetic field along different lines in the Z direction. Considering the minimum in the difference between magnetic field vector magnitude (H) along the different lines in the three directions it can be found the optimal position for the magnetometer in the proximities of the ferrite core.

In this position, the distortion produced by the ferrite core on the magnetic field is in the order of 0% to 10.8%. The highest difference is concentrated in the inner face and affected in a small region, as it is shown in FIGURE 20.

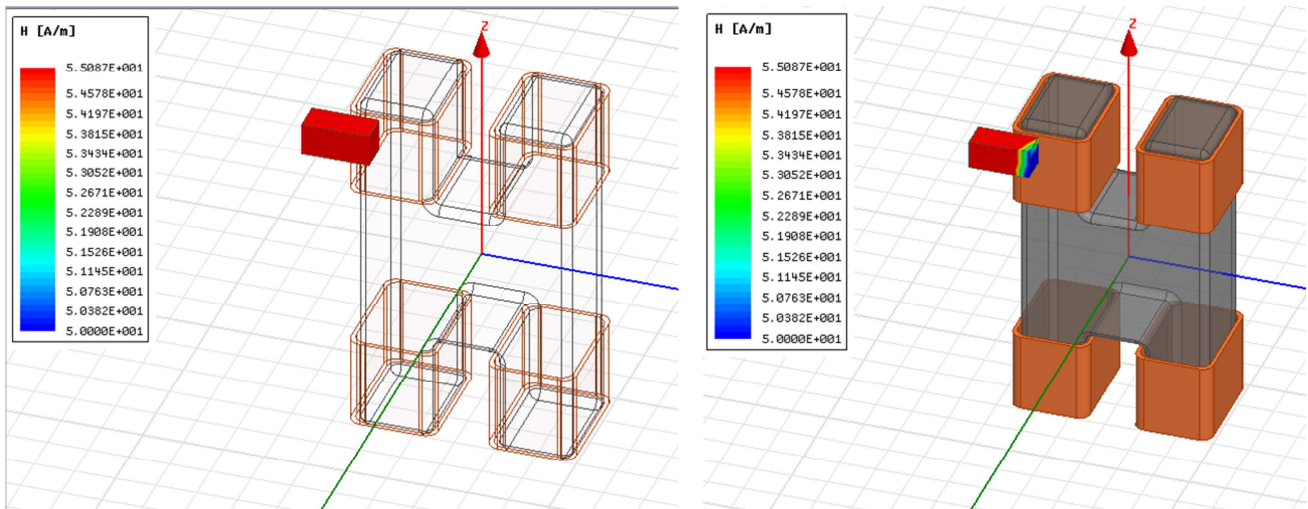


FIGURE 20. Left: The H vector in the surface of the HMC1023 magnetometer without ferrite core. Right: The H vector in the surface of the HMC1023 magnetometer with ferrite core.

4. ELECTRONIC CONTROL UNIT

4.1. Overview and target requirements

The control unit, which is described below, is responsible for the generation of the signals used to measure the necessary characterization parameters as well as communication with a process unit that controls the entire system autonomously through a command system and a proprietary communications protocol. The preliminary design of the electronic control unit can be found in D3.2 [6]. For this the system generates a controlled excitation signal in amplitude, frequency and phase and connects it through a power amplifier to a sensor head from which 2 signals are extracted that are amplified, rectified in full wave (thanks to TTL reference signals) and are filtered and then converted to digital data that will be processed on the on-board computer.

4.2. Detailed design

4.2.1. Hardware system for excitation and measurement

The excitation and measurement unit is responsible for generating a total of 3 signals, one of which will be used for excitation and the other two will act as a reference for each of the two lock-in channels that will be used for the measurement. Said signals are generated in a controlled manner by serial communications between the central microcontroller and the signal generator stages.

The measurement is made by the full-wave rectification operation with subsequent filtering, which is considered a measurement in phase between a reference signal and the input signal. Once the signal is filtered, it is measured with an ADC converter and sent as data for the subsequent post-processing.

The stages that form the measuring instrument can be seen in FIGURE 21.

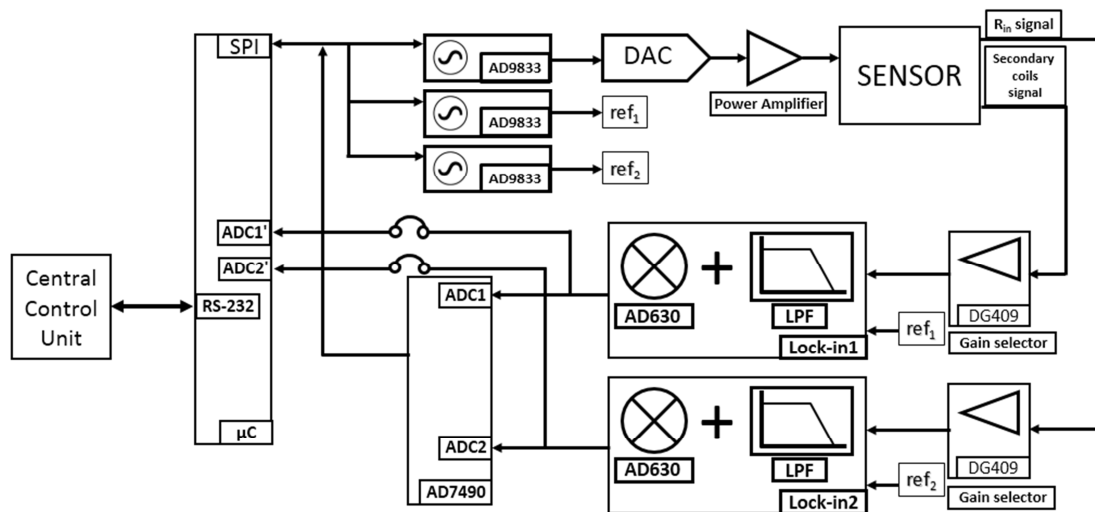


FIGURE 21. General scheme of the measuring instrument.

4.2.1.1. Signal generator block

This block is responsible for generating the sensor excitation signals and references for each of the signal rectifiers that act as a lock-in. The parts that compose it, within the general scheme can be seen in FIGURE 22.

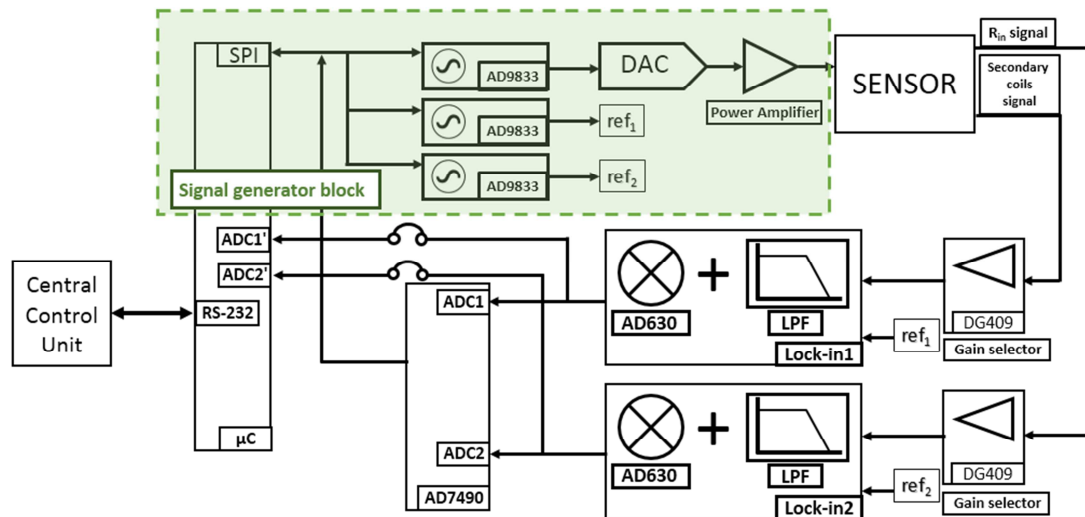


FIGURE 22. General diagram of the measuring instrument and indication of the signal generation block.

The fundamental elements of this block are the signal generators AD9833. These are SPI-controlled oscillators that are able to control the form, frequency and phase of the output signal, thanks to the system of loading values by registers. The block diagram of these devices can be seen in FIGURE 23. These oscillators are controlled by the core of the system, which is the microcontroller which will be discussed later. This μC is connected via an SPI bus to the oscillators where it loads the data related to the characteristics of the signal that have been mentioned above. The SPI protocol consists of 4 lines: SDI, SDO, SCK and CS, which are respectively data input, data output, clock signal and chip select. In the case of the AD9833 only the lines will be used to load data, so the pins corresponding to SDO (SDATA) SCK (SCLK) and CS (FSYNC) will be used.

There are 3 possible operations for the handling of oscillators:

1. Control of the shape of the signal: To choose between triangular, sinusoidal, square and square with period $T / 2$. It is done by loading a value in the control register.

DB15	DB14	DB13	DB12	DB11	DB10	DB9	DB8	DB7	DB6	DB5	DB4	DB3	DB2	DB1	DB0
0	0	B28	HLB	FSELECT	PSELECT	0	RESET	SLEEP1	SLEEP12	OPBITEN	0	DIV2	0	MODE	0

FIGURE 23. AD9833 control register.

2. Control of the frequency of the signal: it is carried out by loading in the dedicated registers, the data whose conversion results in the division of the oscillation frequency of the master clock to which the device is connected. The frequency of the output signal is calculated by the equation:

$$f = \frac{FREQREG \cdot f_{mclk}}{2^{28}} \quad (4.2-10)$$

Where f_{mclk} is the frequency of the master oscillator. Two possible values are allowed: 1MHz to obtain a definition of 0.004Hz per register LSB, and 25MHz for 0.1Hz resolutions.

3. Phase control: in a similar way the phase of the signal can be changed with respect to that of the master clock. In this case, since the register is only 12 bits the equation that will govern the value of the phase is the following:

$$\theta = \frac{PHASEREG \cdot 2\pi}{2^{12}} \quad (4.2-11)$$

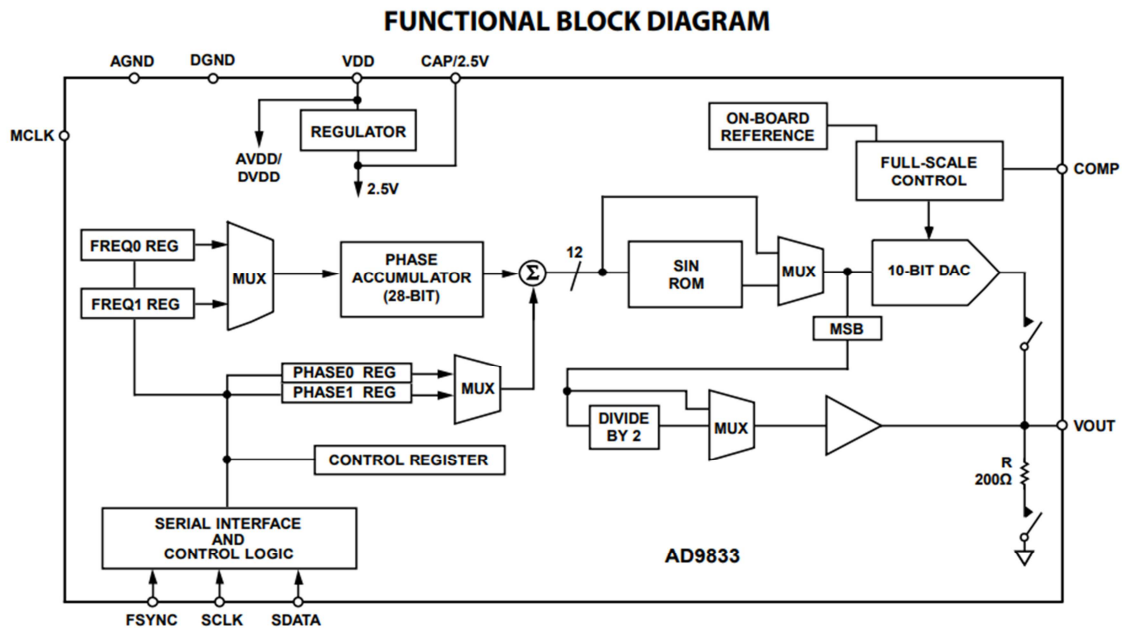


FIGURE 24. AD9833 block diagram.

As previously indicated 3 oscillators will be used to generate 3 signals, one of which will be the sensor excitation and will be connected to a digital-analog converter DAC for digital amplitude control, and will be a sinusoidal signal. The other two signals will be for the lock-in references so they will be TTL type signals.

The DAC converter that has been chosen is the AD5452. It is an SPI controlled converter whose block diagram is shown in FIGURE 25. Like the AD9833, only the three SPI signals corresponding to data entry (SDIN), clock signal (SCLK) and Select device or chip select signal (SYNC).

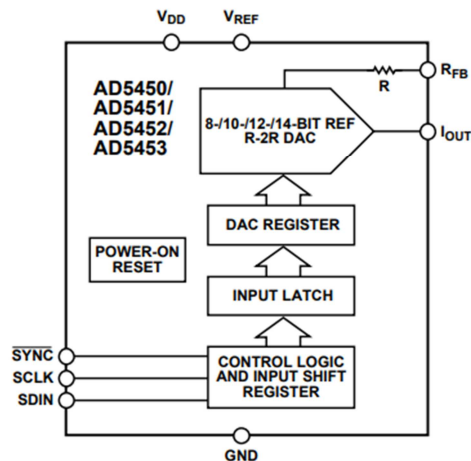


FIGURE 25. Block diagram of AD5452 DAC converter.

The value of the output voltage will depend on the numerical value of the device's own register. In the case of model AD5452, this register is 12 bits so the maximum definition that can be achieved with the selected 5V power supply is:

$$LSB = \frac{5V}{2^{12}} = 1.22 \text{ mV} \quad (4.2-12)$$

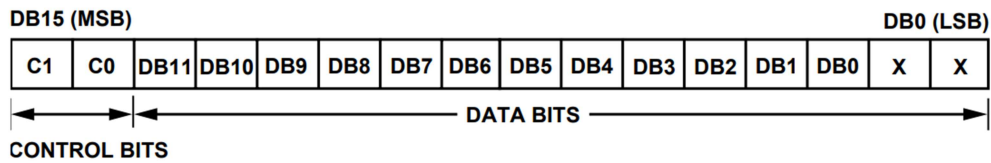


FIGURE 26. AD5452 conversion register.

The assembly used for this converter allows the conversion across the range of voltages that marks the dynamic range of analog power supply of the instrument. That is, the conversion register shown in FIGURE 26 allows output signals whose amplitude ranges from the negative supply voltage to the positive supply voltage. In FIGURE 27 the assembly diagram is shown.

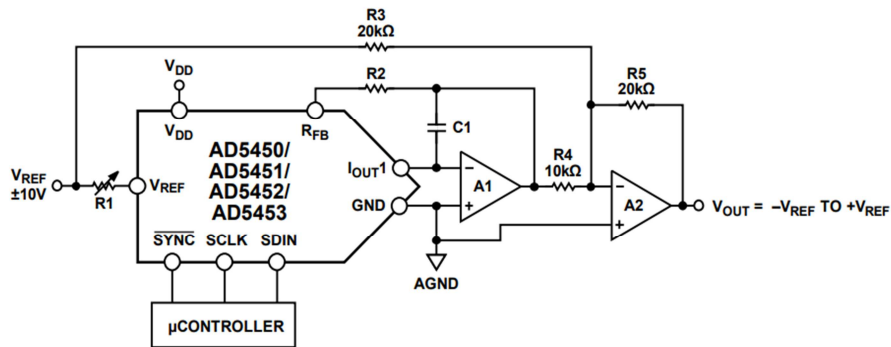


FIGURE 27. Diagram of the AD5452 converter setup.

The converter circuitry is complemented with OP484 type rail-to-rail operational amplifiers. The that component has been chosen integrated 4 amplifiers internally. The main advantages of these amplifiers are shown in FIGURE 28:

FEATURES

- Single-supply operation**
- Wide bandwidth: 4 MHz**
- Low offset voltage: 65 μ V**
- Unity-gain stable**
- High slew rate: 4.0 V/ μ s**
- Low noise: 3.9 nV/ \sqrt Hz**

FIGURE 28. Main characteristics of the OP484.

4.2.1.2. Power stage

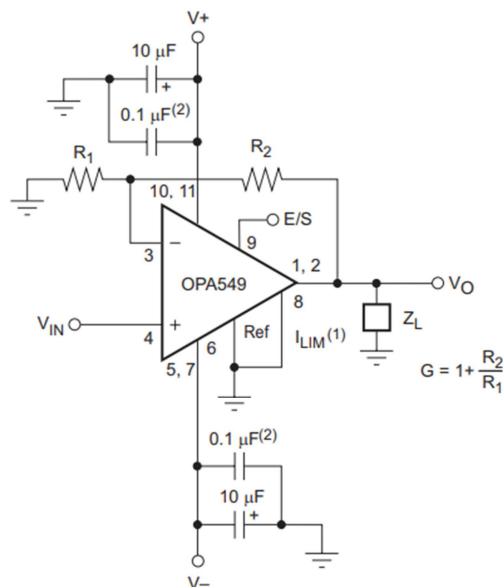
The output of the DAC is connected to a power amplifier that allows current amplification, prior to being introduced into the resonant circuit as a magnetic field generation signal. The power amplifier chosen is the OPA549-HiRel. It is an operational amplifier with the following characteristics:

FEATURES

- **High Output Current:**
 - 8-A Continuous
 - 10-A Peak
- **Wide Power Supply Range:**
 - Single Supply: 8 V to 60 V
 - Dual Supply: ± 4 V to ± 30 V
- **Wide Output Voltage Swing**
- **Fully Protected:**
 - Thermal Shutdown
 - Adjustable Current
- **Output Disable Control**
- **Thermal Shutdown Indicator**
- **High Slew Rate: 9 V/ μ s**
- **Control Reference Pin**
- **11-Lead Power Package**

FIGURE 29. Characteristics of the OP549-HiRel amplifier.

The objective of adding this element in the signal excitation chain is to obtain an element that is capable of supplying all the necessary current to the sensor head and in the entire range of frequencies that is needed to comply with the specifications of the instrument. The assembly used for the amplifier is the one corresponding to a non-inverting amplifier. The idea of this assembly is not to have problems associated with the signal mismatches characteristic of an inverter assembly. It is, of course, necessary to minimize the sources of error between the excitation signal and the reference signals.


FIGURE 30. Setup of the operational amplifier OPA549-HiRel.

The manufacturer provides data on the frequency behavior of said amplifier that serve to justify its correct choice. In FIGURE 31 y FIGURE 32 can be seen as both in terms of gain and phase as output voltage, the behavior of the amplifier is appropriate. The logarithmic drop in terms of gain in the working range can be replaced thanks to the fact that the DAC allows a digital control of the output voltage which makes that the gain can remain constant.

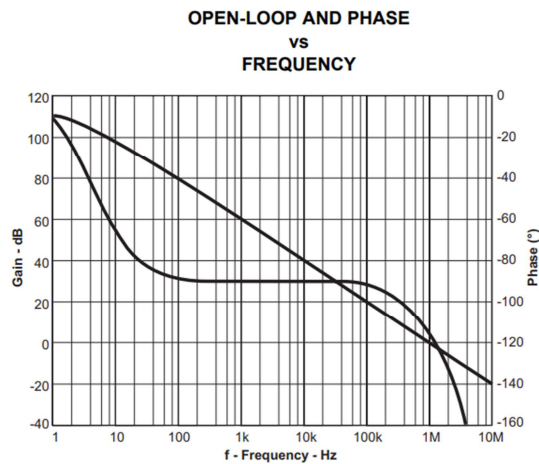


FIGURE 31. Frequency response of the gain and phase parameters of the amplifier.

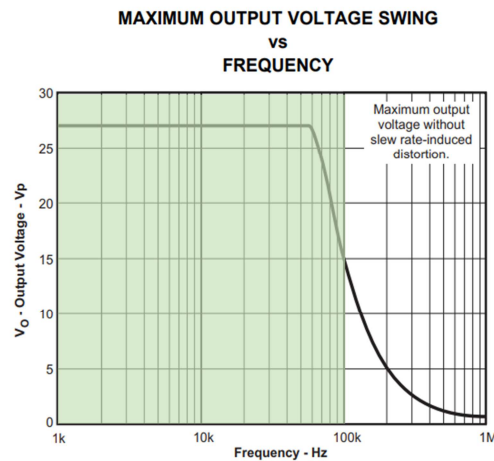


FIGURE 32. Output voltage of the amplifier in the frequency range of the instrument.

According to FIGURE 32 the maximum output voltage that can be achieved is 27V, in the frequency range where the gain oscillates between 20dB and 60dB. If this gain is in terms of power, it can be assumed that for the worst case of frequency, the output power can be up to 100 times the input power. By making an approximate calculation we can establish input current margins in the specific range of work.

For minimum gain if:

$$P_{out} = 100P_{in} \rightarrow V_{out}I_{out} = 100V_{in}I_{in} \quad (4.2-13)$$

For a maximum output voltage, according to the manufacturer, and for the most restrictive case in terms of current output (2.5 A) and assuming that the input voltage is the maximum that the DAC (5V) can give the current of input that is necessary to obtain the maximum magnetic field (maximum excitation current) is:

$$I_{in} = \frac{27V \cdot 2.5A}{100 \cdot 5} = 135mA \quad (4.2-14)$$

For the case of maximum gain (60dB) doing a similar calculation:

$$I_{in} = \frac{27V \cdot 2.5A}{1 \cdot 10^6 \cdot 5} = 13,5\mu A \quad (4.2-15)$$

4.2.1.3. Measurement and acquisition of signal from sensor

The measurement and acquisition system is formed by subsystems showed in FIGURE 33:

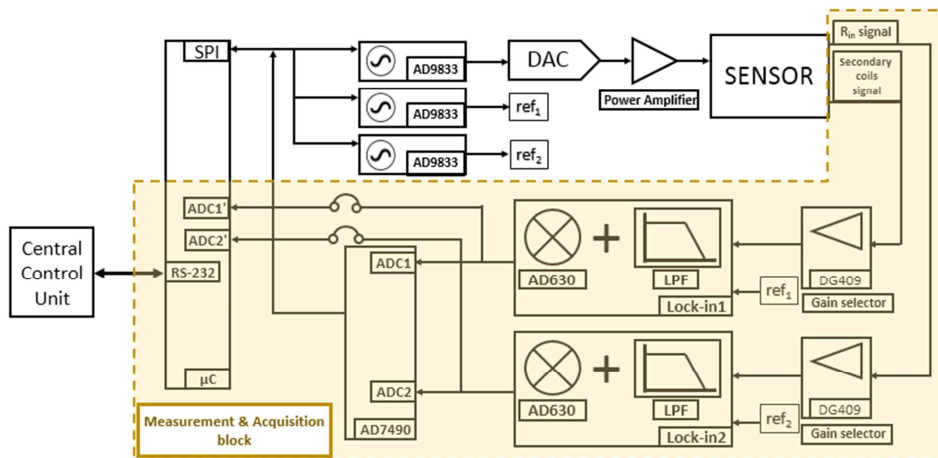


FIGURE 33. Measurement block and acquisition of data from the sensor.

The two signals named " R_{in} " and "secondary coils signal" are those coming from the output of two instrumentation amplifiers that provide the signal values at the ends of the input resistance of the resonant circuit (previous to the sensor) and the differential signal result of the subtraction of the secondary windings mounted on the sensor head. The amplifier chosen for this function is the AD8422BRZ. The main characteristics of said device are shown in FIGURE 34.

FEATURES

- Low power: 330 μ A maximum quiescent current
- Rail-to-rail output
- Low noise and distortion
 - 8 nV/ $\sqrt{\text{Hz}}$ maximum input voltage noise at 1 kHz
 - 0.15 μ V p-p RTI noise ($G = 100$)
 - 0.5 ppm nonlinearity with 2 k Ω load ($G = 1$)
- Excellent ac specifications
 - 80 dB minimum CMRR at 10 kHz ($G = 1$)
 - 2.2 MHz bandwidth ($G = 1$)
- High precision dc performance (AD8422BRZ)
 - 150 dB minimum CMRR ($G = 1000$)
 - 0.04% maximum gain error ($G = 1000$)
 - 0.3 μ V/ $^{\circ}\text{C}$ maximum input offset drift
 - 0.5 nA maximum input bias current
- Wide supply range
 - 4.6 V to 36 V single supply
 - ± 2.3 V to ± 18 V dual supply
- Input overvoltage protection: 40 V from opposite supply
- Gain range: 1 to 1000

FIGURE 34. Main characteristics of the instrumentation amplifiers used.

During the preliminary design, this amplifier was chosen for two fundamental reasons: first, it is a device that has been used other times with quite positive results, and second, it is an amplifier with a quite adequate frequency response, taking into account the wide range of frequencies in which you are working. FIGURE 35 shows the graph given by the manufacturer that justifies that at adjustable gain $G = 1$ the behavior of the gain that can be obtained is practically constant.

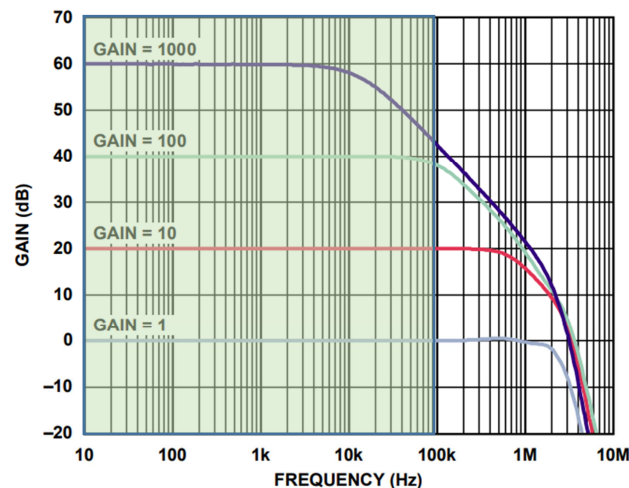


FIGURE 35. Behaviour of the gain of the instrumentation amplifier in the frequency range of work.

It can also be seen in FIGURE 35 that within this frequency range the behavior is practically constant also for 10dB and 100dB, which drops slightly when it reaches 100 KHz.

The formula used to calculate the gain resistance of the amplifier is:

$$R_G = \frac{19.8K\Omega}{G-1} \quad (4.2-16)$$

During the preliminary design, a variable resistance was substituted in the place of the one calculated as R_G . However, it was observed that the behavior of the amplifier gets worse when no resistance was used, so in the definitive design it was decided to leave said resistance without mounting. In these conditions, R_G is an open circuit which makes that the gain G would be 1. The output signals of the two instrumentation amplifiers are connected to a gain chain that amplifies the 3, 9 and 27 factor signals. It is done with OP484 operational amplifiers, as indicated above. The configuration of each one of these stages is non-inverting so, as has been justified previously, no uncontrolled phase shift in the output signal is introduced. The selection of each of the gains is made through the analog switch DG409CY. It is based on multiplexing technology through MOSFET.

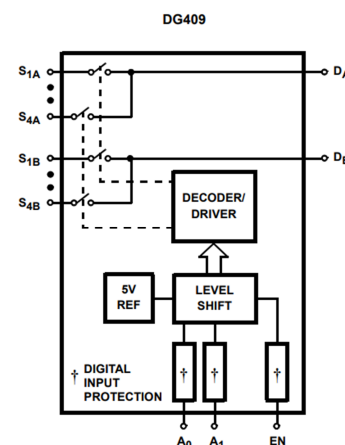


FIGURE 36. Block diagram of DG409.

The control inputs of said multiplexer are A0, A1 and EN. Depending on the value they acquire, the DA and DB outputs will be connected to each of the inputs. The behavior is described by the truth table shown in TABLE 11.

TABLE 11. Truth table of DG409.

A ₁	A ₀	EN	ON SWITCH
X	X	0	NONE
0	0	1	1
0	1	1	2
1	0	1	3
1	1	1	4

In the preliminary design, the inputs corresponding to channel B were canceled and only channel A was used. In the final design this same assembly was respected since it has been mounted two identical output chains for each of the signals coming from the sensor. This was done due to it is needed to make each of the outputs independent with the idea that the gain control and the rectification process (modulation) were controllable signal to signal. The final design contemplates two different paths for the two signals and, therefore, the option to cancel channel B and use only A is respected in the two switches used. The output signal of the switch is connected as an input to the lock-in amplifier. The lock-in design consists of a full wave rectifier and a low pass filter. An AD630 demodulator and the necessary operational amplifiers for the design of two active low pass filters have been mounted for each of the two sensor output signals.

As the lock-in process, adjusted to the design specifications, is no more than a full-wave rectification, the mathematical process is that of a multiplication of the measurement signal with a square signal. The AD630 is a modulator / demodulator that is based on the switching between two signals (direct and inverted) with the switching signal being the output of a comparator between the reference signal and ground. The resulting signal will be defined above 0 with a continuous level that will be proportional to how synchronized the input signal and the reference signal are. Two completely out-of-phase signals will have a maximum but negative continuous level. Conversely, the maximum positive level will be achieved when both signals are completely in phase.

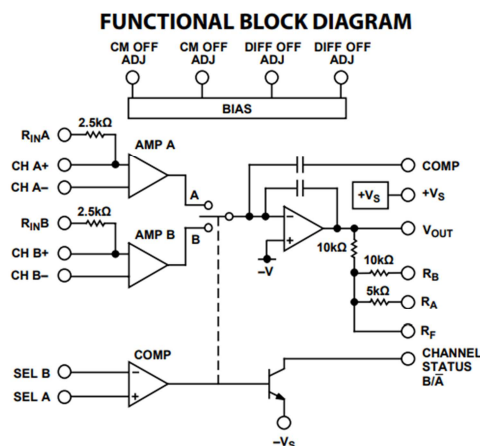


FIGURE 37. AD630 block diagram.

The final process of obtaining the acquisition signal is completed with two active low pass filters in series, one of second order and one of first. Both filters are implemented with operational amplifiers of the same model as those mentioned above. The output signal of this stage will be a DC signal which, as mentioned above, is proportional to the amplitude of the sensor and reference signals, and to the phase shift between them.

The last stage prior to the storage of the data is the connection of the output of the filters to an analog-digital converter for the conversion of the continuous signal into a digital data that will be used for the post-processing of the information referring to the susceptibility. In the preliminary design, this stage was implemented in the microcontroller itself using one of the peripherals. The convenience of using an ADC with greater definition (greater number of bits) was seen, so the model AD7490-EP has been chosen. It is an ADC converter with 12 conversion bits, which guarantees a definition of:

$$LSB = \frac{5V}{2^{12}} = 1.22mV \quad (4.2-17)$$

Its block diagram can be seen in FIGURE 38. The principle of conversion of ADCs involves the selection of certain conversion modes as well as the conversion speed or the sequencing of the input channels. Therefore, it is necessary that the device integrates a logical unit that serves as a configurator of the operation of the ADC. It also has a control of the serial port and the converter itself, which in this case is through the process of successive approaches.

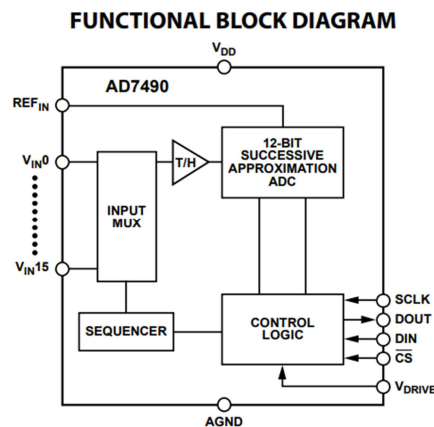


FIGURE 38. Internal block diagram of the AD7490-EP.

The system is designed to make the selection between the two possible ADCs, the one mentioned now and the ADC integrated in the microcontroller. This will be used in the case where the measure does not require a too high definition. If the external ADC is selected, the orders pertaining to the load in the control register of the bits that govern the behavior of the ADC and the commands used to extract the conversion data will be added.

MSB											LSB	
11	10	9	8	7	6	5	4	3	2	1	0	
WRITE	SEQ	ADD3	ADD2	ADD1	ADD0	PM1	PM0	SHADOW	WEAK/TRI	RANGE	CODING	

FIGURE 39. ADC converter control word.

The SEQ and SHADOW bits are used to control the sequencing of the conversion channels. The AD7490 allows the absence of it or the conversion following patterns programmed in the SHADOW register. This

register consists of 16 bits that indicate which channels should be converted. When the conversion is selected through the use of this register, the value of the SHADOW register is loaded internally before each conversion start and after loading the control register. Each time the level of the device selection input (CS) pin is changed, the register traversed to select the channel to be converted. The bits from ADD3 to ADD0 select the channel to be converted. Under certain sequencing configurations these bits mark the single conversion of the indicated channel or the end of a channel-to-channel sequence, starting at channel 0. The PM1 and PM0 bits configure the operating power modes of the ADC, things like stand-by mode or auto-off mode. Finally, the WEAK / TRI, RANGE and CODING bits control, respectively, the state of the Vout line, the range of reference voltages and the type of numerical coding of the output data.

4.2.1.4. Microcontroller

The instrument's processing unit is the PIC16F887 microchip microcontroller. It is responsible for managing the entire system and storing the program code that allows communication between the μC and the central control unit installed on the platform. The microcontroller has stored the necessary code to autonomously perform the following functions:

1. - Loading of the information in the registers of the excitation signal generators and references.
2. - Control of the ADC converter for the measurement of the information extracted from the sensor head.
3. - Measurement of the information extracted from the sensor, as an alternative to the use of the external ADC.
4. - Communications with the central control unit. It has stored all the information related to the general communications protocol for the instrumentation designs of the entire process.

4.2.2. Explanation of the codes using in the system

4.2.2.1. Explanation about communication frames

As previously stated, the microcontroller autonomously controls the entire system carrying out the functions explained above by handling the elements and devices mounted in the hardware design. For this, it executes a series of orders from the central processing unit mounted on the control platform. It does this through an RS-232 serial data line, where data packets belonging to a native protocol designed for this project are exchanged.

During the previous phase of design a protocol was used for this control by its own orders and quite basic since the number of orders that had to be given was not very high. During the final design phase, this protocol was adapted to all the instruments of the project and the order system was reorganized to make it easier to use. The communications between the central unit and the microcontroller are based on the sending and receiving of a series of data packets that both the transmitter and the receiver must understand and accept or reject. The data packets contain subfields that compose disagreeable frames so that it is easy for the receiver to discern whether the frame is correct or not and in what way it is not.

Control frame

The control frames are sent by the transmitter and receiver and processed by the receiver that, based on certain aspects related to the form and content of the data packet fields, answers with two valid answers:

- 1- ACK frame: the receiver has received the frame and there are no errors in it.

2- NACK frame or error: the receiver has received the frame incorrectly and requires it to be forwarded. The basic structure of the frames can be seen in FIGURE 40.



FIGURE 40. Basic structure of communication frames between the central control unit and the microcontroller.

Where:

- **Head:** the header of the plot will give information about the morphology of the data package, as well as information about the data transmission.
- **Order:** This is the content of the frame itself, and contains the information regarding the order that the transmitter wants the receiver to execute or information about the results that the transmitter wants to send to the receiver.
- **CRC:** the results of the error control operations in the frame are stored.
- **Tail:** the tail of the frame contains the bytes that delimit the end of the data package.

Each of these fields, in turn, are composed of smaller packets that correspond to bytes or groups of bytes that form the frame that can be seen in FIGURE 41.



FIGURE 41. Parts that make up the communication frames.

We describe below each of the subfields that make up the plot:

- **0x55:** This code in binary corresponds to byte 01010101. It is a code widely used in digital communications to detect errors produced in noisy channels. It is a check code that has no meaning as such for the execution of the order that contains the frame.
- **T.W (To Who):** is the identifier code of the recipient of the message.
- **F.W (From Who):** contains the identification code of the message transmitter.
- **Length (MSB):** is the most significant byte that marks the size of the frame, that is, the byte of the order and the number of arguments.
- **Length (LSB):** is the least significant byte that indicates the size of the frame: order more arguments.
- **Order:** this is the byte identifier of the order that the transmitter wants the receiver to execute or on which confirmation or response is sent with the sending data required by the transmitter itself. There can be a total of 254 orders (1-254), discarding the data 0x00 as a valid order and the 0xFF that will be used for the error notifications.
- **Argument (from 1 to n):** they contain the bytes that are the necessary data for the order to be executed. If the frame is the error, the argument or arguments will be those corresponding to the identification of the error that has occurred.
- **CRC:** Cyclic redundancy code. It is the result of a mathematical operation that is done with all the bytes that form the frame. The idea is that the transmitter of the data packet sends the CRC and this value is compared with that obtained by the receiver when it receives the frame. If both coincide, the transmission is correct. If not, an error must be reported. Generally the mathematical operation is the XOR but there are

more sophisticated codes with great features to detect failures and make communication much more reliable. In principle, this is implemented due to the low complexity of the protocol and the great robustness of the communications line.

- **0x00**: this is the delimitation code at the end of the frame.

Answer frames

The two possible response frames are shown in FIGURE 42 and FIGURE 43.



FIGURE 42. Proper confirmation frame for sending or ACK.



FIGURE 43. Error frame.

The confirmation frame or ACK is identical to the order's sending frame. The only difference is that the T.W and F.W fields change order. This has the great advantage that the error check is much faster since the CRC is identical to having the frames the same fields but placed differently. In the case of the error frame, the change mentioned before also occurs as well as including the 0xFF byte as content of the order field. In the field of arguments, which is reduced to only one, the identifier of the error that has been detected is included.

4.2.2.2. Explanation of the orders for microcontroller handling

As mentioned above, the microcontroller is managed through a series of commands that come from the central processing unit and have the objective of controlling each of the devices installed in the hardware of the measuring instrument. In the case of the preliminary design, the orders were focused on the management of two signal generators and a single measurement signal. In the case of the definitive design, the new protocol must contemplate the existence of two reference signals and two measurement signals.

These orders are:

- 1- Order 30: change of the frequency in the oscillator AD9833. The arguments of the order will contain the information about the selected oscillator, and the data that must be loaded in the register of the oscillator.
- 2- Order 31: change of amplitude in the DAC. The arguments of the order will contain the data that must be loaded in the converter registry.
- 3- Order 32: phase change of the AD9833 oscillator. The arguments of the order will contain the information about the selected oscillator, and the data that must be loaded in the register of the oscillator.
- 4- Order 33: change the gain of the sensor output signal to x3. The arguments of the order include the information about the switch on which to act.
- 5- Order 34: change the gain of the sensor output signal to x9. The arguments of the order include the information about the switch on which to act.

- 6- Order 35: change the gain of the sensor output signal to x27. The arguments of the order include the information about the switch on which to act.
- 7- Order 36: make a measurement with the ADC. The arguments of the order refer to the ADC that must be used.
- 8- Order 37: reading of the external ADC. The arguments of the order refer to the channel or set of channels on which you want to perform the conversion.

The microcontroller is programmed with two interruptions: the UART and the ADC, and is prepared to coordinate the conversion of the analog data with the sending of the same through the serial port. When it has finished, it is sent to the central processing unit that receives the data, processes it and unlocks the execution of the code allowing the μC to execute another conversion of the ADC. The way to unlock the code is sent a confirmation frame from the central unit as a validation of the data it has just received.

4.3. Functional verification

In the preliminary design, the board was tested to verify its operation. Some images were obtained in each of the stages through which the reference and excitation signals pass since they are generated, and the measurement signal of the sensor. The difference between the board with the provisional design and the board with the definitive design is a blocking path and an additional external analog-digital converter. Conceptually there is no difference between the two boards so the signals are identical.

FIGURE 44 represents the provisional scheme of the board, and shows the reference signal used for the demodulator. FIGURE 45 corresponds to the output signal of the DAC converter prior to the power stage. FIGURE 46 is the output signal of the demodulator (full wave rectifier). FIGURE 47 (blue signal) is the DC level of the AD630 output signal that is filtered and converted into digital data in the ADC converter of the microcontroller. Two more measurements were taken to obtain the graphs in point 4 (FIGURE 44) and verify that the lock-in works properly. It was tested with two signals (reference and input) without lag between them and with a lag of 90 degrees. The results can be seen in FIGURE 45 and FIGURE 46 respectively.

The testing of the board with the definitive design consists of checking the operation of the new measurement path (the duplicated lock-in works the same as the previous one). The scheme of the final design with the signals in the corresponding test points is shown in FIGURE 47.

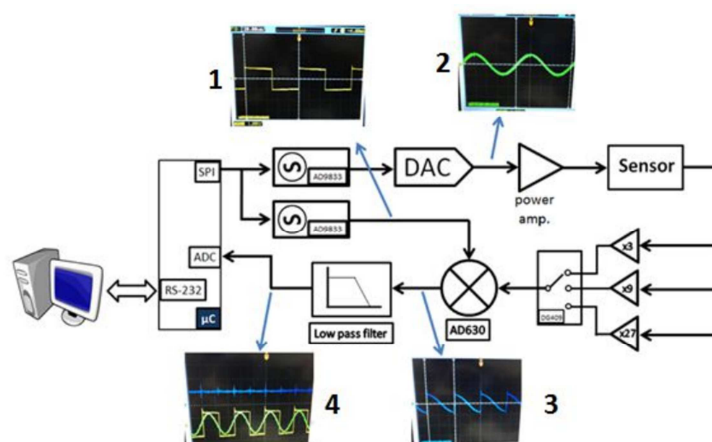


FIGURE 44. Verification of the first designed board.



FIGURE 45. Low pass filter output signal (blue) and input signals in AD630 for a phase shift of 0° .



FIGURE 46. Low pass filter output signal (blue) and input signals in AD630 for a phase shift of 90° .

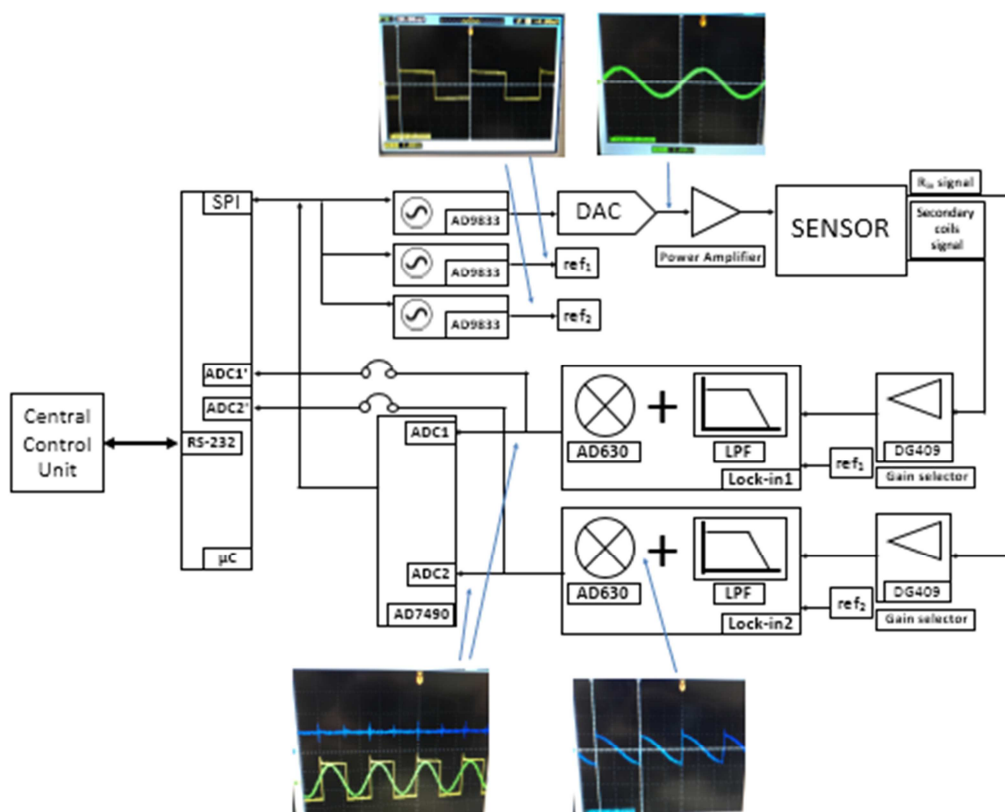


FIGURE 47. General scheme of final design with the signals in the corresponding test points.

5. POWER DISTRIBUTION UNIT

5.1. Overview and target requirements

The Power Distribution Unit of NEWTON instrument (for the three prototypes) supplies energy to the Control Unit and to the Sensor Unit and it is integrated by the AC current source and the power module, i.e. DC/DC converter.

With regard to the AC current source, it drives the primary winding of the Sensor Unit. The requirements of the AC current source are different for each NEWTON instrument. In the case of prototype 3, the demand of the AC current needs an ad hoc development which is based on a Full-Bridge switching. The final design of this source is described in D3.6 [3]. On the contrary, for none of both prototype 1 and prototype 2 is required to implement an individual AC current source. In this case, the generation of the AC current is implemented as part of the electronic Control Unit by means of using a frequency generator and an external amplifier which is placed in the Sensor Unit, as illustrated in FIGURE 48. The requirements are the same for the prototypes 1 and 2, so the same design has been adopted for both instruments. More details related to the signal generation can be found in section 4 (4.2.1.1 and 4.2.1.2).

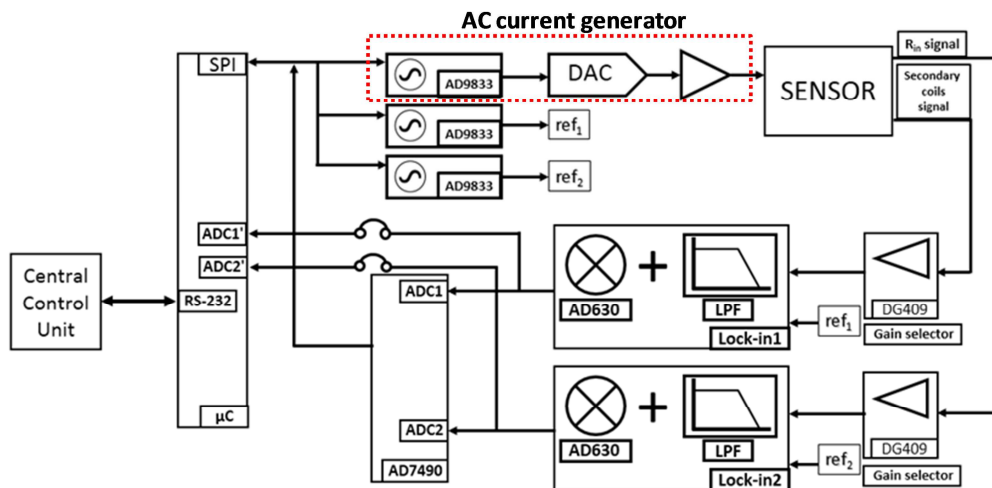


FIGURE 48. AC current generator for NEWTON instrument prototype 1.

With regard to the DC/DC converter, the same design is required for the three NEWTON prototypes, i.e. prototype 1, prototype 2 and prototype 3. As illustrated in FIGURE 49, the DC/DC converter receives the primary power from the rover (or external batteries in the case of prototype 2), and provides three different output voltages with different power consumptions which interface with the electronic CU (+5V) and the SU ($\pm 12V$).

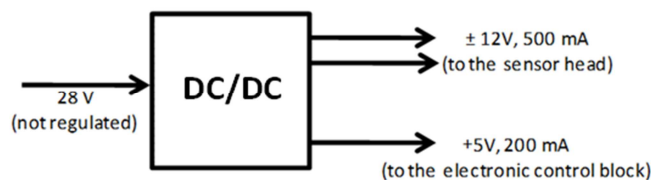


FIGURE 49. Block diagram of the DC/DC converter.

The requirements of the DC/DC converter for NEWTON prototype 1 are listed in TABLE 12. There has been no modification with respect to the requirements initially defined and reported in D2.1 [5] and D3.3 [7].

TABLE 12. Requirements for the design of the DC/DC converter.

Parameter	Prototype 1	Observations
ELECTRICAL		
Input DC Voltage	+28V (not regulated)	From the rover/ lander
Output DC Voltages	+5V +12V -12V	+5V are dedicated to supply general electronics (digital output) +12V and -12V should supply the amplifiers of the susceptometer and magnetometer (analogue output)
Output ripple	$\leq \pm 0.5\%$	Implies a maximum ripple of 120mVpp at the +12V and -12V outputs, and 50mVpp at the +5V output
Output regulation	$\pm 0.1V$	Maximum deviation of the output voltages from their nominal values
Steady current consumption from $\pm 12V$	500mA (max)	Current to be consumed by the susceptometer and the magnetometer
Steady current consumption from 5V	200mA (max)	Current to be consumed by the digital electronics
Inrush current per output	2A	Peak current demanded to the PSU when the devices hanging from its outputs are powered on
ON/OFF feature	Yes	NEWTON instrument operation is enabled after +5V POWER ON of the Control Unit. Magnetometer operation is disabled by removing the +5V (switching OFF) of the PDU to the Control Unit
ISOLATION		
Isolation (Prim. – Sec.)	TBD	Different isolated and non-isolated topologies have been analysed in order to evaluate the main advantages and drawbacks of them
Isolation (outputs)	Isolation required	Two different grounds should be considered, referring the +12V and the -12V outputs to an analogue ground, and the +5 output to a digital one (ground isolation)
EFFICIENCY		
Efficiency	$\geq 90\%$	Efficiency in a steady stage, calculated as the ratio between the total amount of power delivered and the input rms power
SIZE AND WEIGHT		
Area / Height	TBD	Including base plate (or other mechanical parts). The target is to achieve a reduced size.
Weight	TBD	Including base plate (or other mechanical parts). The target is to achieve a reduced weight.

One of the main challenges related to the design of the DC/DC converter is the efficiency. Although, there is no concrete requirement, the target is to achieve maximum efficiency (>90%) in order to save a maximum electrical power due to prototype 1 will operate in a limited energy scenario. In addition to this, the size and weight are also limited resources in space applications. Therefore, the weight and volume of the DC/DC converter will be optimized while the efficiency is maximized. With regard to the isolation requirement, different isolated and non-isolated DC/DC source topologies were analysed during the preliminary design stage, and compared considering different features such as their efficiency, output power, design complexity, flexibility and physical dimensions. In particular, a Flyback converter, a Half-Bridge converter and a Synchronous Buck converter were designed and implemented and their performances were experimentally evaluated in the laboratory with the aim of analysing the advantages and drawbacks of each

of them. This work was reported in deliverable D3.3 [7]. It is important to note that, as already mentioned, the power and control units of NEWTON instrument will be allocated inside the rover body which will protect the DC/DC converter from some of the environmental requirements.

5.1.1. Background from the preliminary design

Three different converters were implemented and validated during the preliminary design stage. Preliminary validation results showed that the efficiency of Buck converter which is around 96% achieves the target requirement. In the case of isolated topologies, Flyback converter was discharged due to its low efficiency for the requirements of NEWTON instrument (around 60%) while the Half-Bridge converter provides an efficiency (80%) close to the target while its physical dimensions and design complexity is similar to the non-isolated solution. After analysing these preliminary results, two different lines of work were distinguished depending on the way in which the power supply isolation is obtained. If we consider that the not-regulated +28V that supplies the NEWTON DC/DC converter already offers huge isolation from the main supply of the system, a synchronous Buck based architecture can be deployed, obtaining a very good efficiency-volume-cost ratio. In the other hand, if the +28V input doesn't guarantee isolation from a main supply, galvanic isolation should be implemented, and an architecture based on a main Half-Bridge converter and some synchronous Bucks hanging from a main output line could be an optimum solution. These two lines of work have been evaluated during the final design stage. To that purpose new designs have been developed, implemented and validated as section 5.2 and 5.3 describe.

5.2. Detailed design

5.2.1. Non-Isolated DC/DC converter

The block diagram of the non-isolated DC/DC converter is illustrated in FIGURE 50. As can be seen, the source consists on a Synchronous buck converter which is integrated at the same time by three different Synchronous buck converters providing the different output voltages required by the instrument.

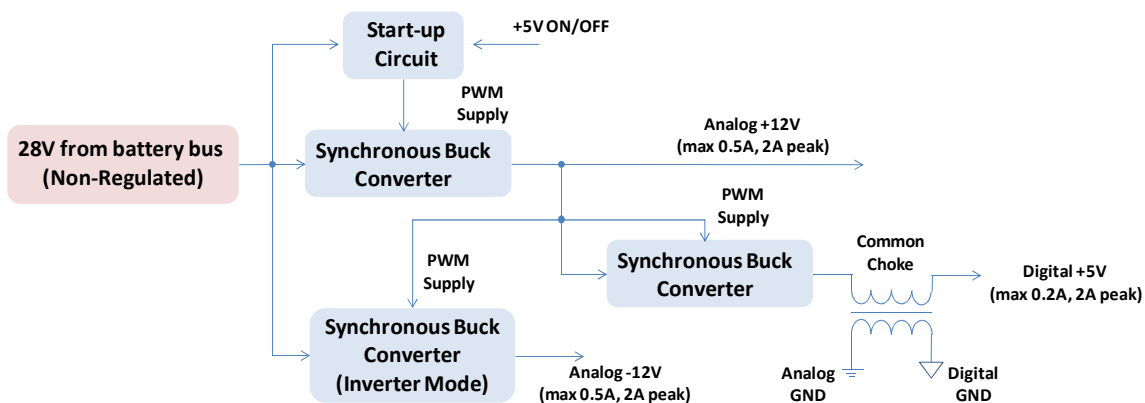


FIGURE 50. Block diagram of the proposed non-isolated solution for the DC/DC conversion.

The +12V synchronous buck converter is connected to the primary +28V bus. Then, the +5V converter is connected in cascade with the +12V converter to introduce some advantages in the design, such as the decrease of the voltage drop in the conversion, and thus, to avoid the use of PWM duty cycles with wider spectral content. Also this configuration helps to minimize the ripple at the low voltage digital bus and move the operation of the +12V converter to a higher load point, improving the global efficiency. A common choke was placed as an isolation element to minimize the common and differential noise between analog and digital buses. For the negative voltage generation, the synchronous buck architecture was modified by means of changing the nodal references to obtain both voltage and polarity conversion. This

change implies that the differential voltage applied to the circuitry is now $V_{in} + |V_{out}| = 28V + 12V = 40V$. Although the circuitry employed in the design is capable to drive these values, to fulfil the derating requirements ([8]) the controller circuitry is powered from the +12V converter, while the switches are connected directly from the main 28V input bus.

5.2.1.1. Sub-Circuits design

The main synchronous buck circuit including the FET driver and the logic block to generate the complementary PWM signals is depicted in FIGURE 51 (This is part of the +28V to +12V converter). In this synchronous buck configuration one transistor operates as switch whereas the other is the synchronous rectifier, reaching higher efficiency than its counterpart based on rectifying diodes. The devices employed are enhancement mode gallium nitride FETs (eGaN FETs). Compared to the traditional silicon MOSFET, eGaN FETs have higher switching speeds and power handling capabilities in a much smaller footprint. The logic array transforms the signal from the PWM controller to the complementary waveforms that performs the ON/OFF process for both the switch and the rectifier and controls the “dead time” interval to ensure the soft-switching operation.

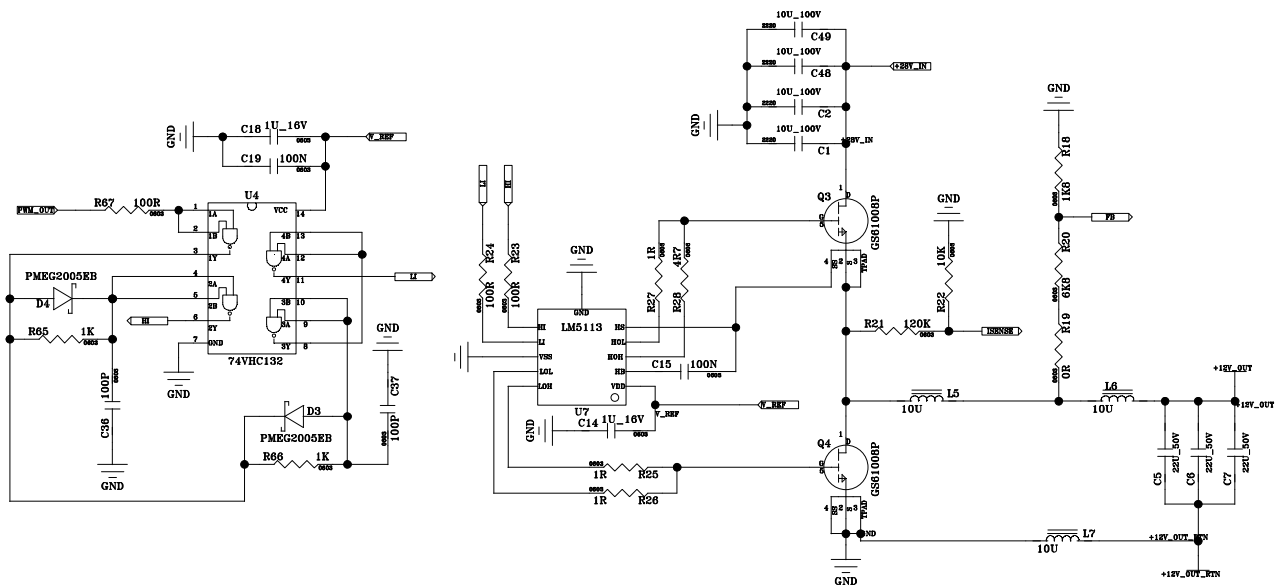


FIGURE 51. Circuit schematic of the synchronous buck sub-circuit (+28V to +12V converter).

The PWM signal is generated by a controller unit that integrates the feedback error amplifiers and the compensation circuits in a single chip. The external components are adjusting elements to ensure the correct operation at the desired conditions. FIGURE 52 shows this sub-circuit based on the device UC1843 from Texas Instruments.

The start-up sub-circuit implements the process that follows the converter when it is switched on. In the first moments, the controller circuitry is supplied by V_{in} ($V_{SUPPLY} \approx V_{in}$), until the converter starts to provide output voltage. In this moment the start-up sub-circuit switches between V_{in} to V_{out} and reach a higher efficiency operating regime ($V_{SUPPLY} \approx V_{out}$). A simulation of this sub-circuit was performed using the Quite Universal Circuit Simulator software (QUCS) and is presented in the FIGURE 53.

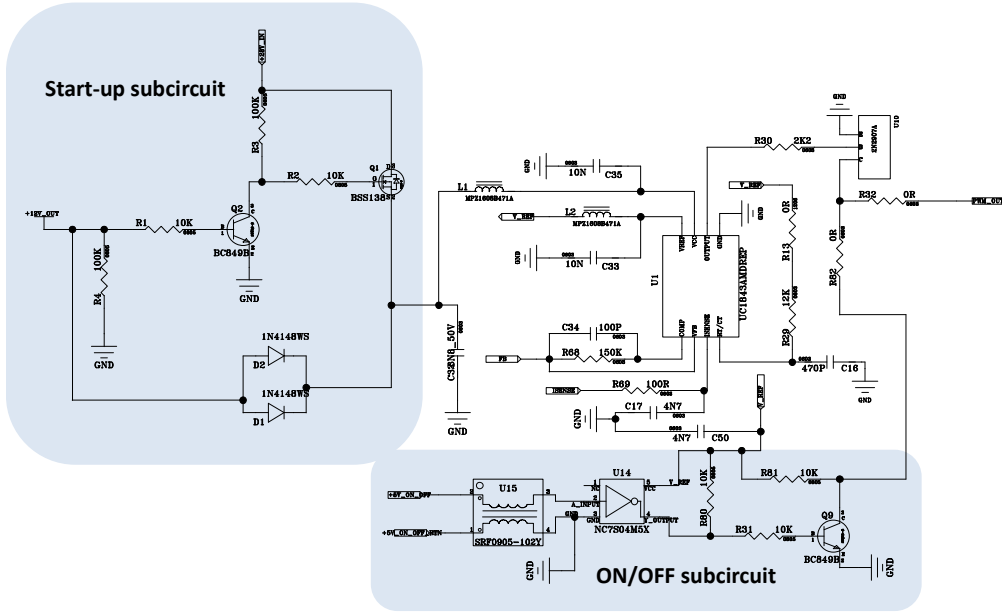


FIGURE 52. Schematic of the synchronous buck sub-circuit (part 2). Start-up circuit and ON/OFF sub-circuit.

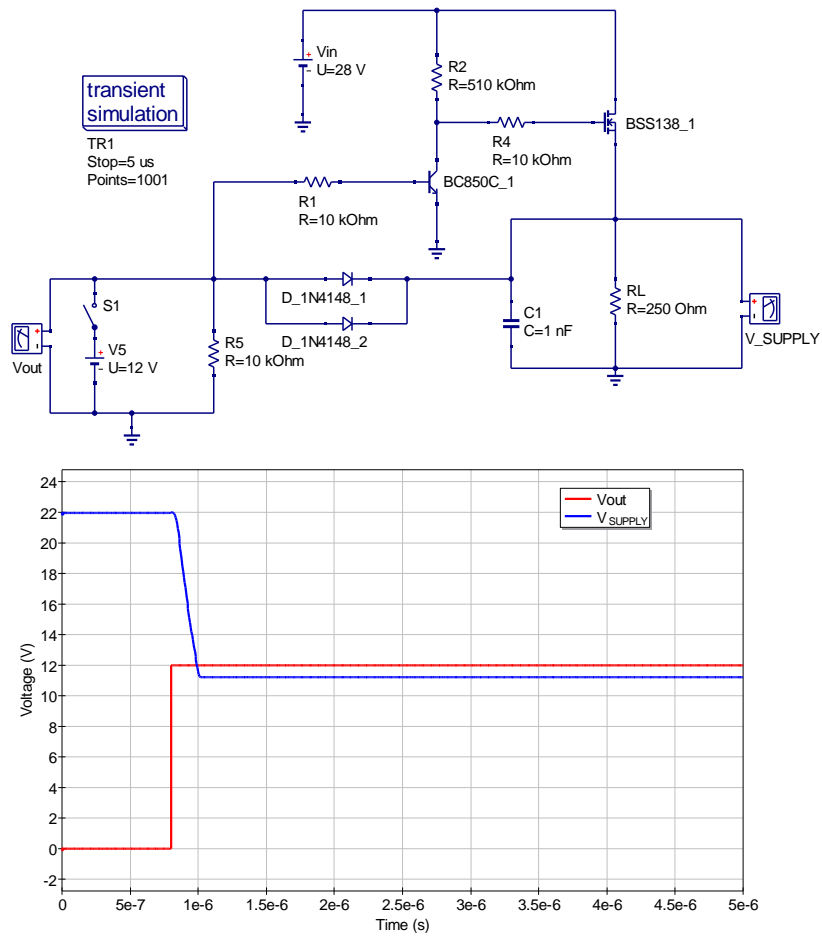


FIGURE 53. QUCS simulation of the start-up circuit.

The transition speed is controlled by the capacitor C1 and the diodes in parallel configuration ensure the isolation between V_{in} and V_{out} before the switching. In addition to this, the ON/OFF sub-circuit is in charge of enabling/disabling the operation of NEWTON instrument by means of switching ON/OFF the DC/DC converter. To do this, a TLL signal (+5V ON, 0V OFF) will be sent by the Control Unit to the PDU to activate the PDU and deactivating it during the inactivity periods which will serve to save energy.

The performance of the synchronous buck converter was simulated using the Tina Software from DesingSoft-Texas Instruments. Ideal devices were employed for the passive lumped elements. For active devices and chips, SPICE models were used. In the cases of components with unavailable models, they were substituted by equivalent devices. FIGURE 54 shows the schematics implementation of the synchronous buck in the simulator.

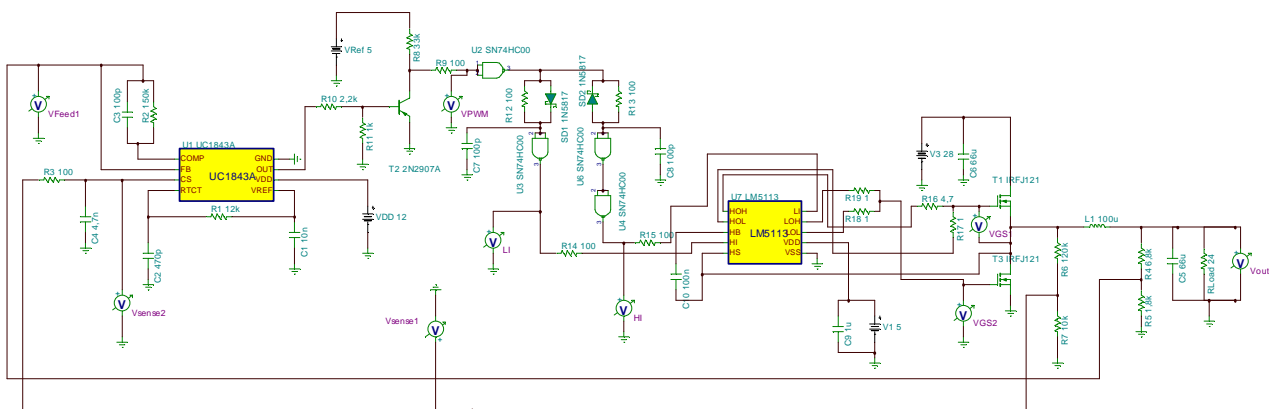


FIGURE 54. Schematics of the synchronous buck architecture simulated in TINA software.

The simulation results are depicted in the FIGURE 55 where the regulation capabilities of the design can be observed.

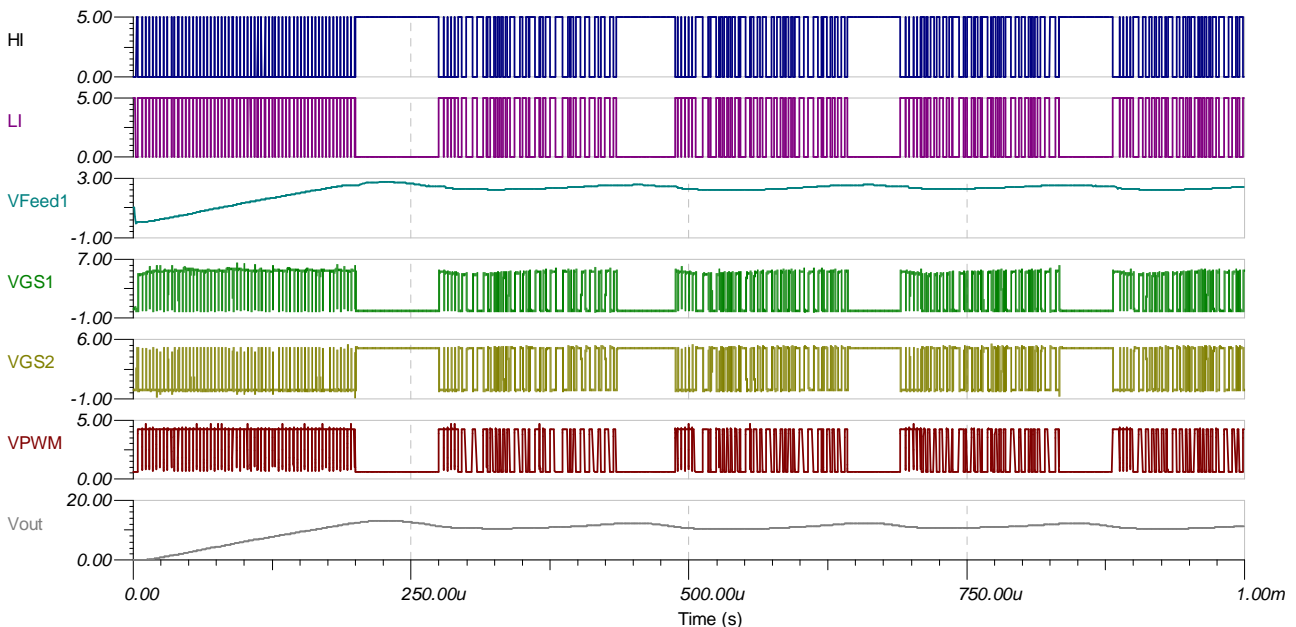


FIGURE 55. Simulation results for the time domain waveform characteristics of the synchronous buck topology.

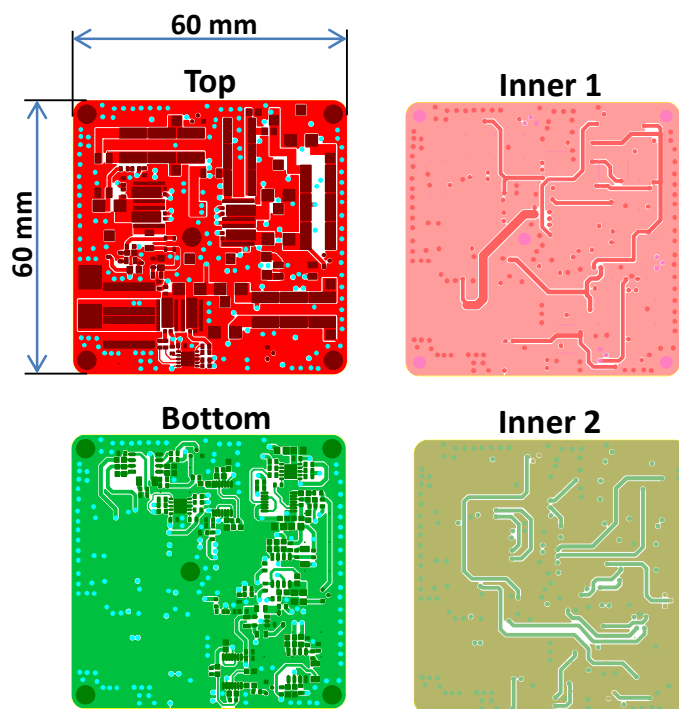


FIGURE 57.PCB layout of the non-isolated DC/DC converter.

The component mounting view of the board and the photograph of the final manufactured PCB are shown in FIGURE 58.

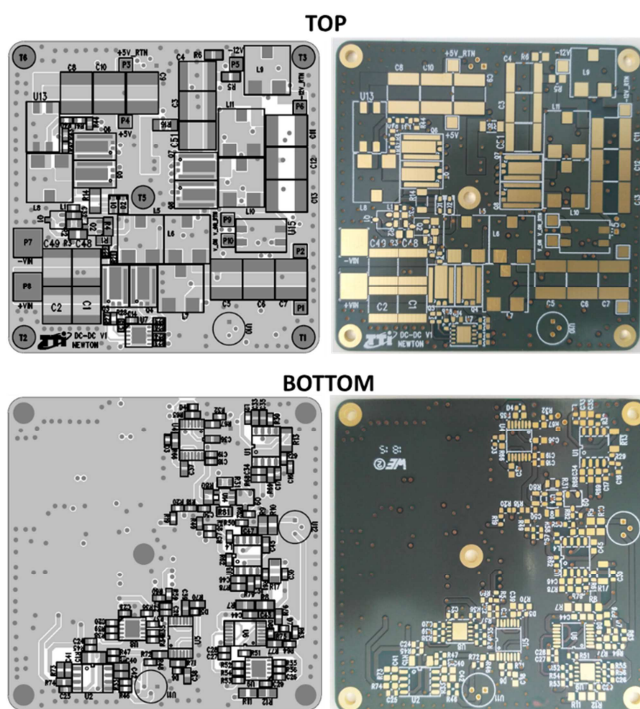


FIGURE 58.Component mounting view (left) and photographs of the manufactured PCB (right).

A metallic box was designed for mechanical support, heat dissipation and EMI shielding. The 3D view of this design can be observed in FIGURE 59, including its main dimensions and connectors. In order to reduce the

weight and size of the enclosure, and simplify the integration process, the same micro D-Sub connector were used for input and output terminals in its female and male version, respectively.

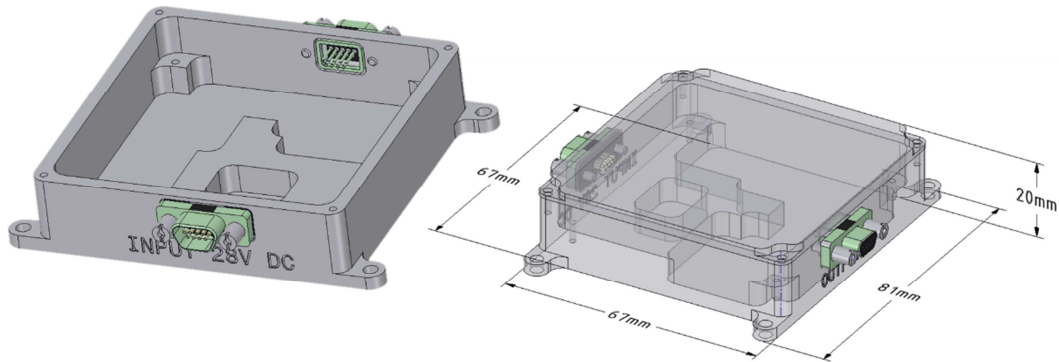


FIGURE 59. 3D view of the metallic enclosure designed for the non-isolated DC/DC converter.

5.2.2. Isolated DC/DC converter

The block diagram of the isolated DC/DC converter was presented in FIGURE 60. The main element of this design is a symmetric half bridge converter. The multi-windings transformer is the core of the half-bridge topology and also provides auxiliary isolated voltages that are used to supply different sub-circuits. In order to avoid the use of an expensive customized transformer, full wave diode rectifiers were used in all output windings of a commercial transformer instead of center tapped rectifier, which needs more complex winding configuration. Also, the use of full wave rectifiers brings other advantages to the design, for example, the PIV (peak inverse voltage) ratings of the diodes in bridge rectifier is half than that of needed in a center tapped full wave rectifiers. The diode used in bridge rectifier has capable of bearing high peak inverse voltage, whereas in center tapped rectifiers, the peak inverse voltage coming across each diode is double the maximum voltage across the half of the secondary winding. The transformer utilization factor (TUF) is also higher in bridge rectifier as compared to the center tapped full wave rectifier, which makes it more advantageous.

As it is shown in the FIGURE 60, the half bridge converter provides the +12V voltage and the +5V is cascaded to this output in a similar way to the topology presented for the non-isolated case (FIGURE 50). The inverter converter for the -12V generation is connected to a non-regulated voltage produced by an auxiliary secondary winding. The auxiliary primary winding is used to provide the voltage demanded by the half bridge controller circuitry in the primary side, which also employs a start-up switching technique.

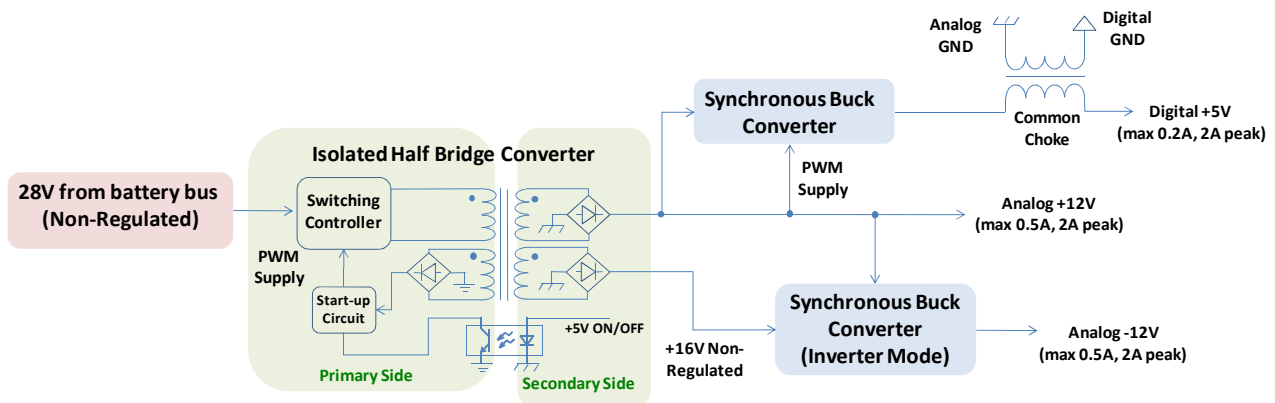


FIGURE 60. Block diagram of the isolated solution for the DC/DC conversion.

5.2.2.1. Sub-Circuits design

The half bridge sub-circuit schematic is represented in FIGURE 61. The architecture is based in the same eGaN devices employed in the synchronous buck converter to take advantages of its improved switching and efficiency capabilities. The opt-isolated feedback network is also represented, where the resistive divisor formed by R14, R12 and R19 is used to set the desired output voltage (+12V in this case).

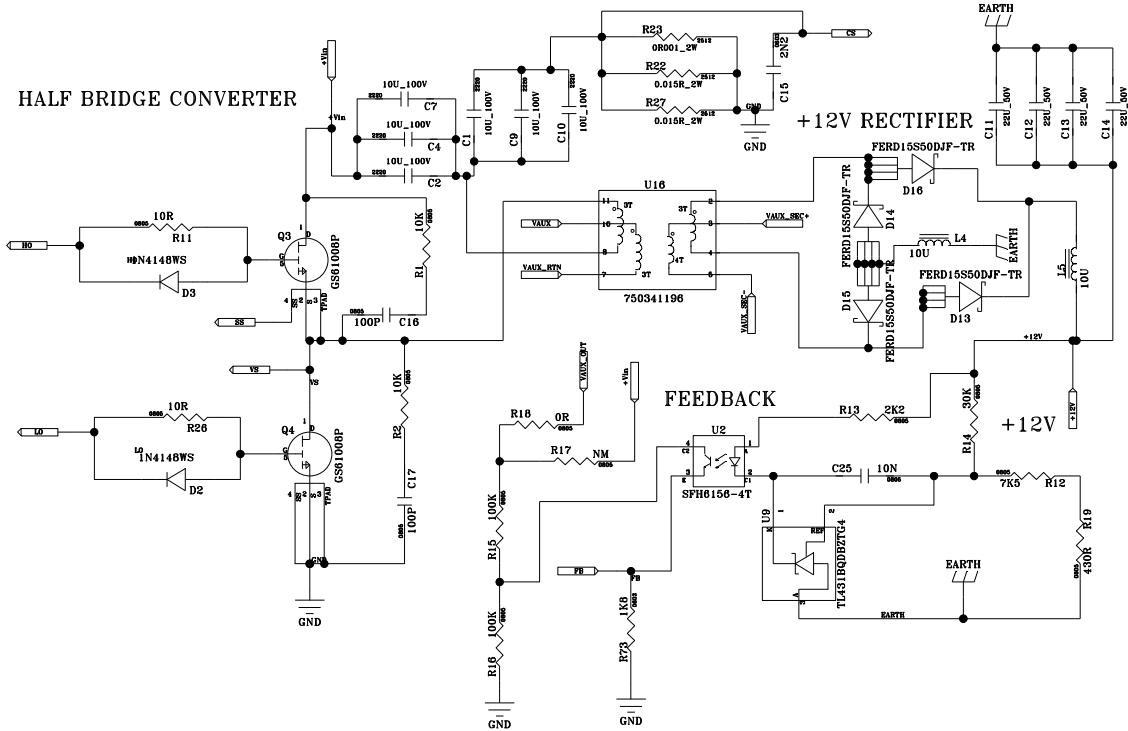


FIGURE 61. Circuit schematics of the half-bridge sub-circuit.

As already mentioned, a commercial transformer from Würth Elektronik has been used for the implementation of the half-bridge converter. FIGURE 62 shows the mechanical information and main electrical information of this transformer.

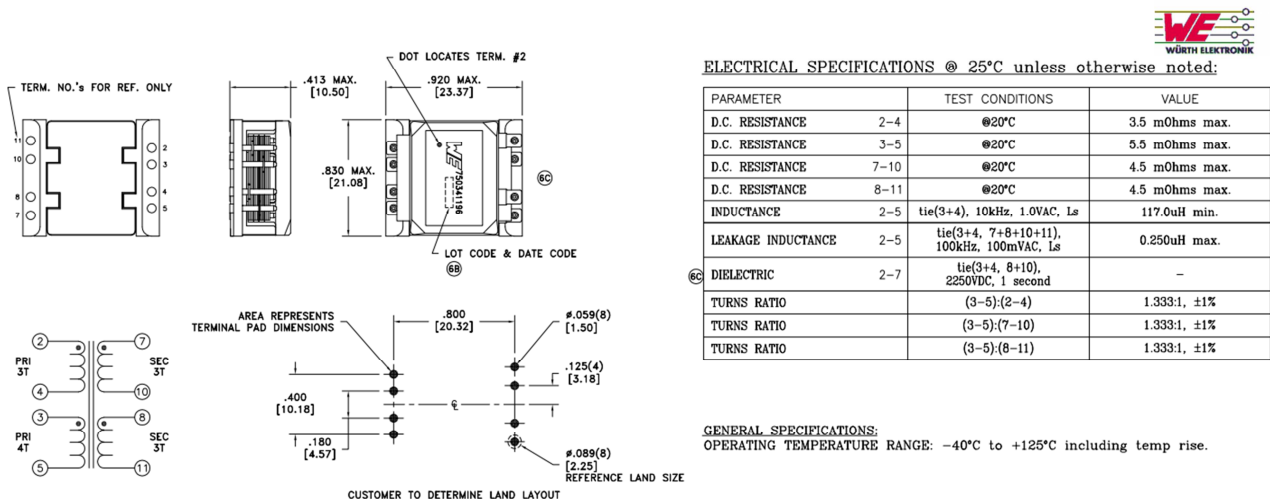


FIGURE 62. Characteristics of the commercial transformer employed in the isolated DC/DC converter.

The half-bridge controller schematic is shown in FIGURE 63, including the ON/OFF, FET driver and the start-up sub-circuits.

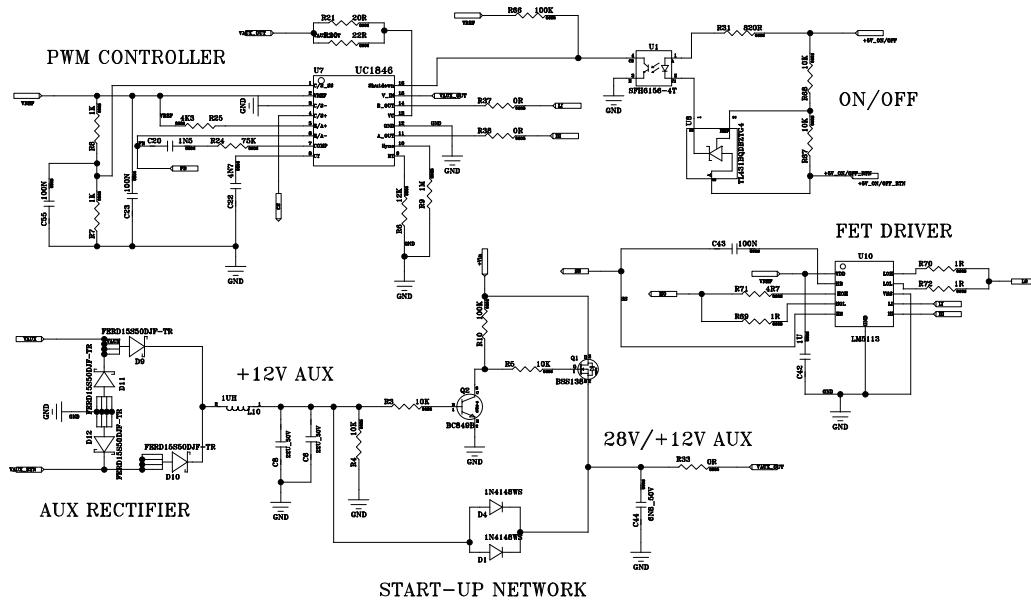


FIGURE 63. Circuit schematics of the half-bridge controller sub-circuit

The PWM controller is based on the chip UC1846 from Texas Instruments, a “classic” device with a widely proved space heritage. The ON/OFF sub-circuit is based on a common emitter opto-coupler connected to the shutdown pin of the UC1846, allowing the safe ON/OFF of the complete unit maintaining the desired isolation. The rest of sub-circuits are similar to the presented in previous sub-section for the non-isolated converter (FIGURE 51, FIGURE 52 and FIGURE 53).

This half-bridge architecture was also simulated using the TINA software. FIGURE 64 shows the circuit implementation on the simulator.

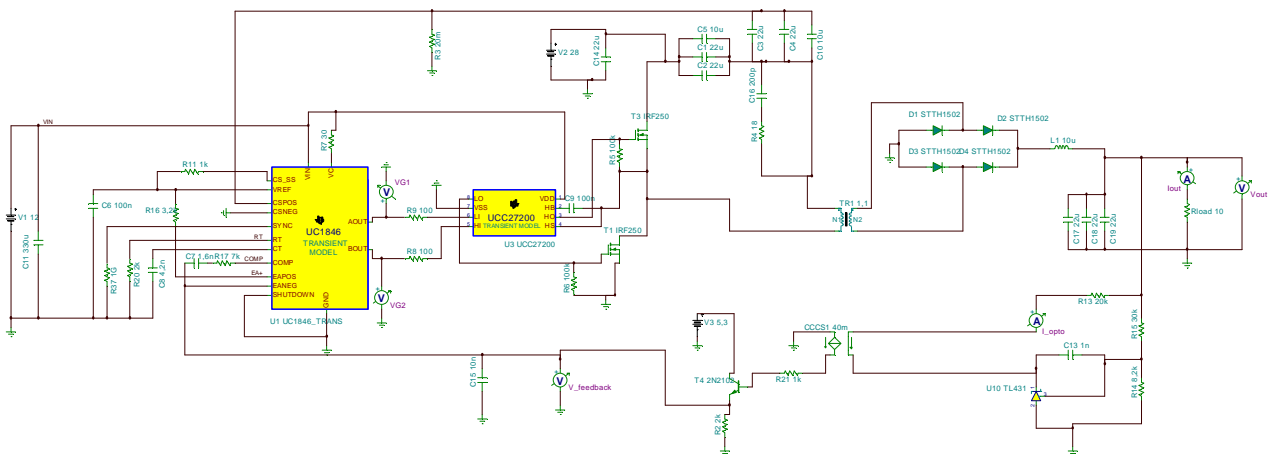


FIGURE 64. Half-bridge circuit implementation on the TINA simulator.

In this case, the same procedure used for the non-isolated converter was followed, employing ideal components, device models, or equivalent device models if were unavailable. For example, note that for modelling the opto-coupler in the feedback sub-circuit, a combination of a current-controller-current-source with a NPN bipolar transistor was necessary. The simulation results are shown in FIGURE 65. Special attention will be paid at the measurement campaign to the initial 20V peak voltage, in order to verify if it is

a real behaviour of the circuit or a mathematical problem of the solver when calculates the initial conditions.

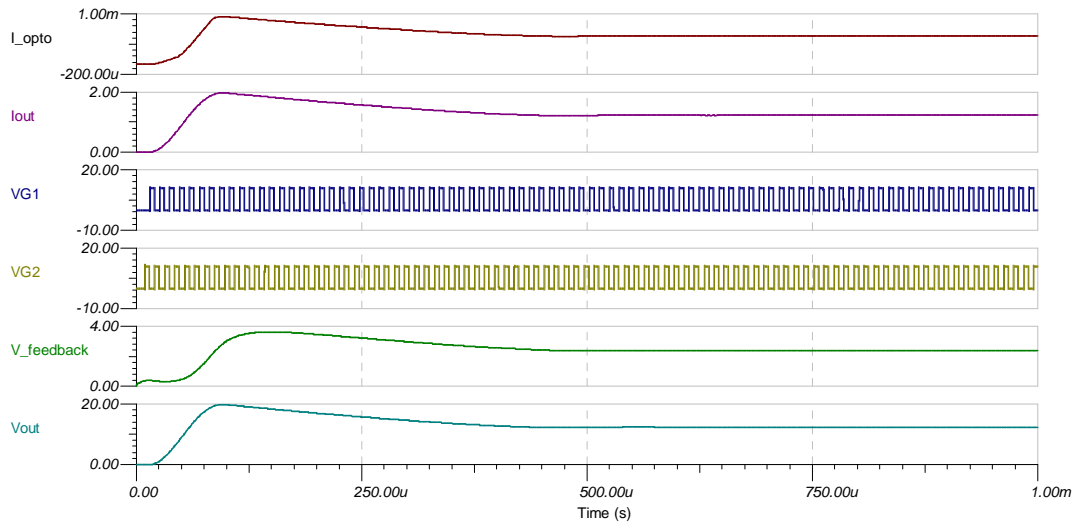


FIGURE 65. Simulation results of the half-bridge converter.

The rest of synchronous buck sub-circuits for -12V and +5V generation are similar to the presented in previous sub-sections for the non-isolated converters. The complete schematic for the isolated multi-output DC/DC unit is shown in the ANNEX 2.

5.2.2.2. Manufacturing and integration

In this case the same FR4 multilayer substrate was employed for the board implementation. FIGURE 66 shows the board layout of the isolated solution including its dimensions.

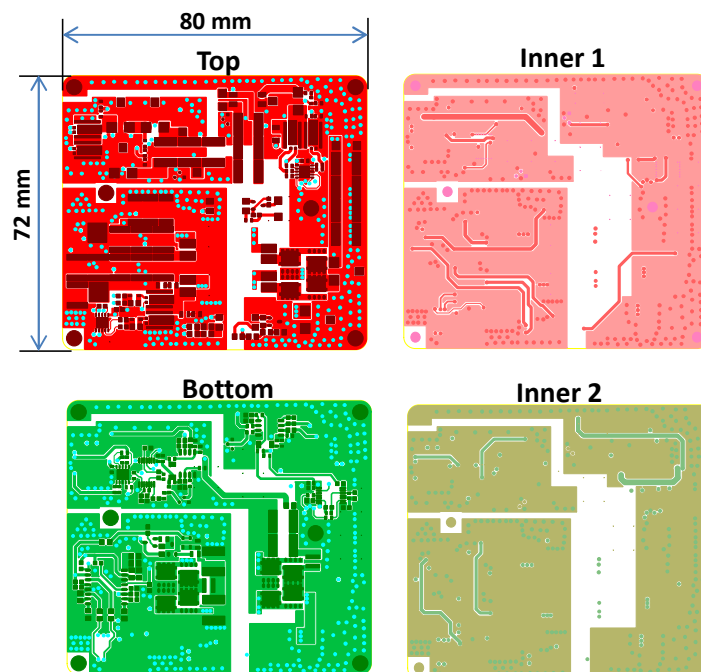


FIGURE 66. PCB layout of the isolated DC/DC converter.

The component mounting view of the board and the photograph of the final manufactured PCB are shown in FIGURE 67.

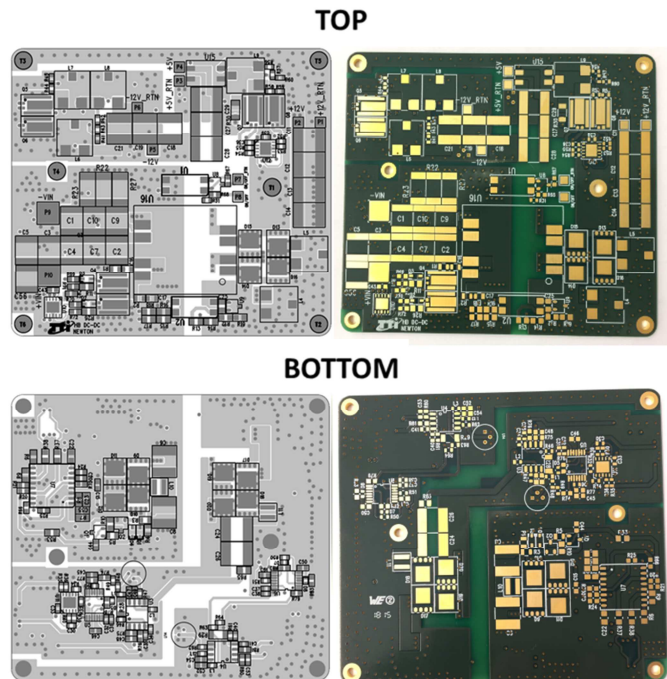


FIGURE 67. Component mounting view (left) and photographs of the manufactured PCB (right).

A metallic enclosure was also designed for this isolated solution. As can it can be observed in the 3D view of the FIGURE 68, the same design guidelines of the non-isolated converter were followed in terms of dimension minimization and the connectors employed.

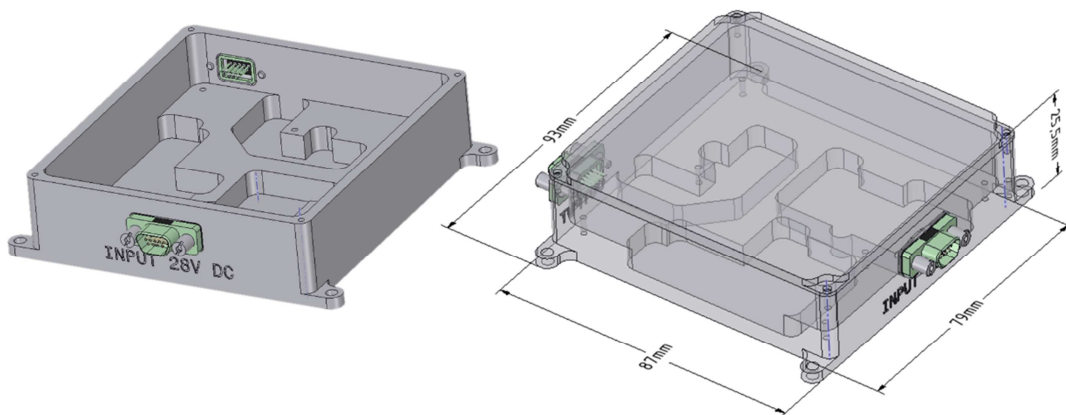


FIGURE 68. 3D view of the metallic enclosure designed for the isolated DC/DC converter.

5.3. Functional Verification

5.3.1. Non-Isolated DC/DC converter

As already mentioned, the Non-Isolated DC/DC converter consists on a synchronous buck converter which is integrated at the same time by three different synchronous buck converters providing the different output voltages. To verify the functionality of the non-isolated DC/DC converter, firstly the performance of the +12V synchronous buck converter was stand-alone validated. To do this, a dedicated PCB was

manufactured and tested in the laboratory. This PCB includes some adjustment elements in order to optimize the performance of the converter and then translate the final configuration to the complete Non-Isolated solution (which includes the three converters). FIGURE 69 shows the manufactured PCB while FIGURE 70 shows the laboratory test-setup used for its validation. The power supply provides the input power +28V voltage, simulating the rover bus. An electronic load varies the current demanded by the output load while an oscilloscope is used to measure the output signals.

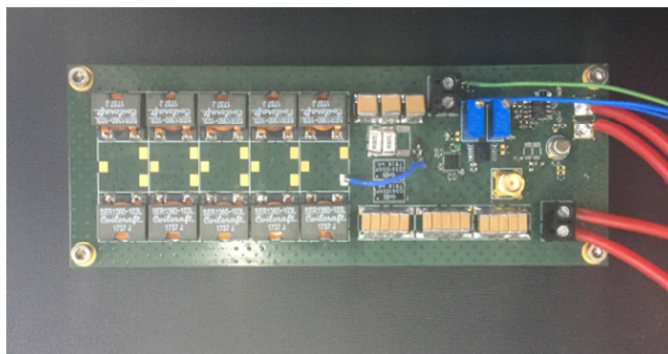


FIGURE 69. PCB manufactured for the functional verification of the +12V synchronous buck converter.

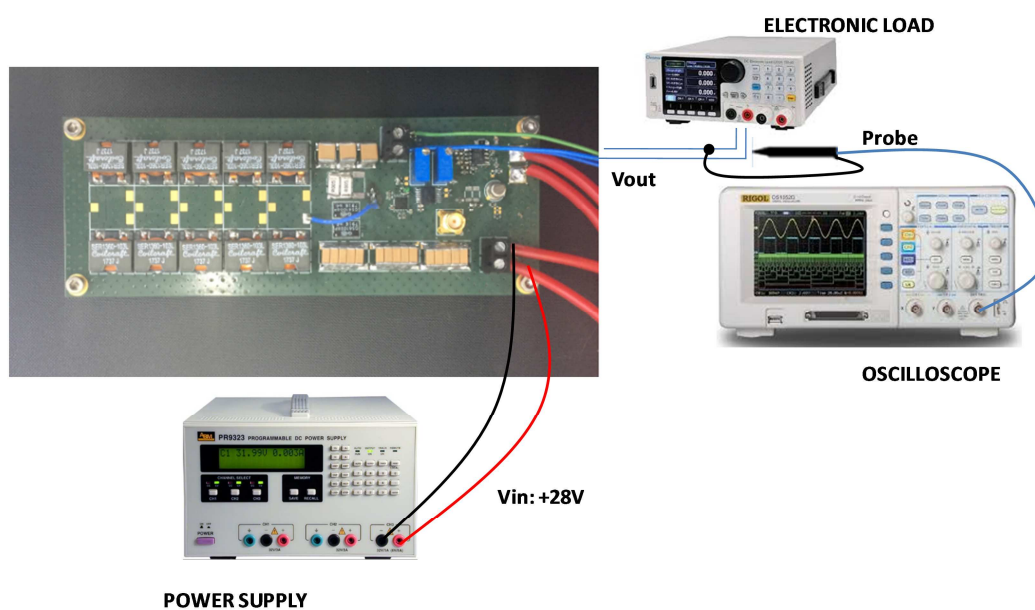


FIGURE 70. Test-setup for the +12V synchronous buck converter validation.

FIGURE 71 shows the results obtained from the validation of the +12V synchronous buck converter after its adjustment. In the figure, the output power vs the input power is illustrated (blue line), as well as the switching efficiency (green line) and the efficiency including the consumption of the PWM (red line). As can be seen the switching efficiency is close to 97% while consumption of the PWM reduces the efficiency till 93.23%. This has been considered for the design of the complete Non-Isolated converter and the consumption of the controller has been optimized.

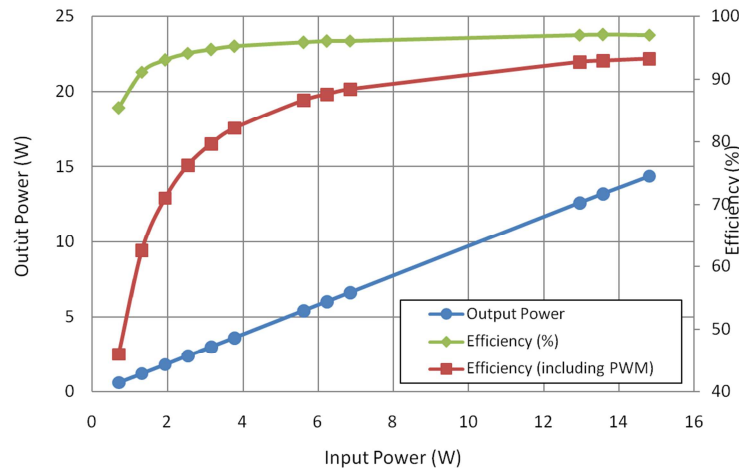


FIGURE 71. Results obtained from the validation of the +12V synchronous buck converter.

The next step within the functional verification of the final design is the validation of the complete Non-Isolated DC/DC converter. Due to a delay in the manufacturing of the boards, the complete validation of the source cannot be finalized before the delivery of this deliverable. This verification will be completed during the next stage of the project and the results will be included in the deliverable D4.1 which is planned to be submitted at the end of June.

5.3.2. Isolated DC/DC converter

FIGURE 72(A) shows the assembled Isolated DC/DC converter. The performance of the converter has been evaluated in the laboratory by means of implementing the test set-up shown in FIGURE 72(B). The power supply #1 provides the input power +28V voltage, simulating the rover bus, while the power supply #2 is used to send the internal ON/OFF signal generated by the Electronic Control Unit to the circuit. An electronic load varies the current demanded by the different output voltage ports while its sense terminal will be used to minimize the effects of the connexion wires in the measurements. Finally, an oscilloscope measures the electrical parameters related to ripple and regulation requirements. The measurements have been performed at ambient temperature. It has not been necessary to place the converter under test over temperature controlled platform due to the power dissipated by the converter is low enough.

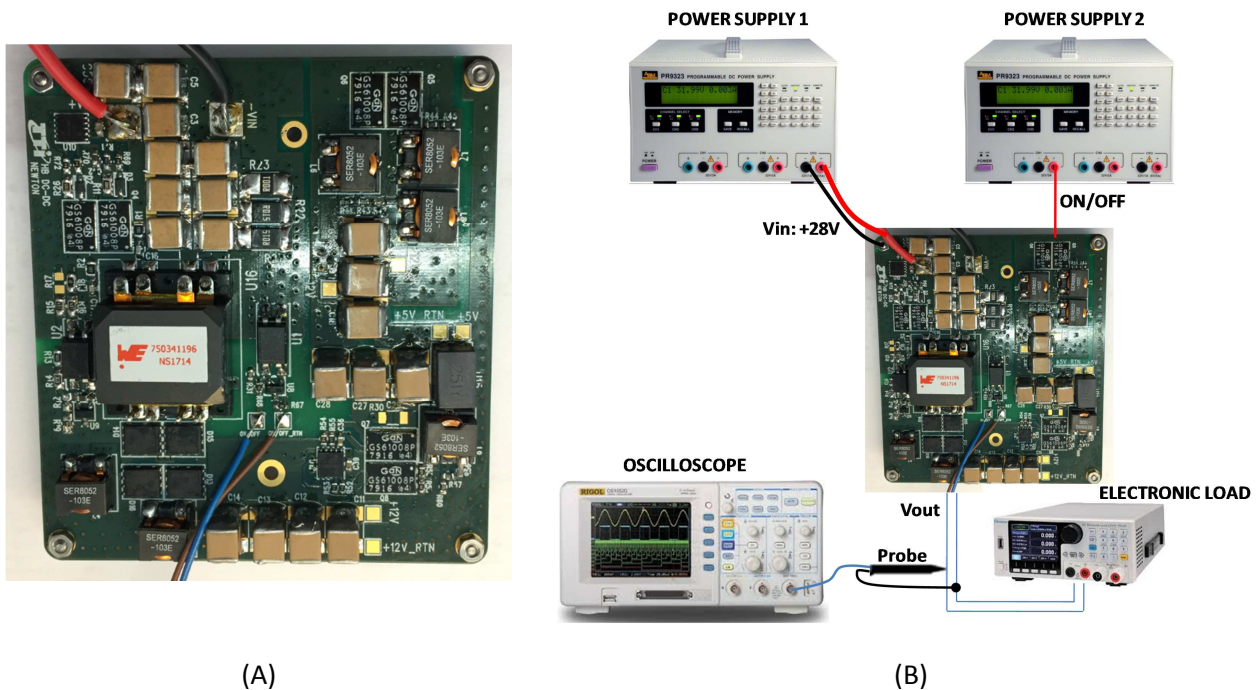


FIGURE 72. (A) Isolated DC/DC converter. (B) Test-setup for the isolated converter characterization.

First of all, the performance of the main element of the isolated DC/DC converter was validated, i.e. the 28V to 12V half-bridge converter. With this regard, TABLE 13 shows the efficiency of this module calculated at different output loads. As can be seen, the efficiency of the converter is around 90% at maximum load.

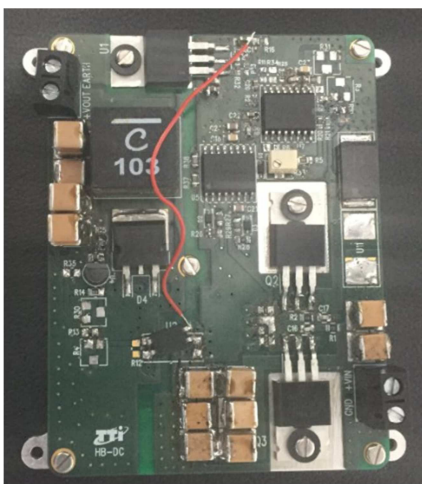
TABLE 13. Efficiency of the +12V HB-DC (eGaN technology) converter for different loads.

Vin (V)	Iin(A)	Pin(W)	Vout(V)	Iout(A)	Pout(W)	Eff(%)	Pdiss (W)
28.00	0.06	1.57	12.00	0.04	0.50	31.84	1.07
28.00	0.11	2.97	12.00	0.13	1.51	50.94	1.46
28.00	0.15	4.23	12.00	0.21	2.50	59.23	1.72
28.00	26.60	5.85	12.00	0.33	4.01	68.47	1.85
28.00	0.24	6.69	12.00	0.42	5.00	74.72	1.69
28.00	26.60	7.71	12.00	0.50	6.00	77.78	1.71
28.00	26.60	9.31	12.00	0.63	7.52	80.78	1.79
28.00	26.60	10.91	12.00	0.75	9.03	82.81	1.87
28.00	26.60	11.97	12.00	0.83	10.02	83.68	1.95
28.00	26.60	13.03	12.00	0.92	11.01	84.51	2.02
28.00	0.50	13.94	12.00	1.00	12.04	86.35	1.90
28.00	0.55	15.32	12.00	1.13	13.54	88.43	1.77
28.00	0.58	16.32	12.00	1.21	14.51	88.88	1.82
28.00	0.64	17.84	12.00	1.33	16.01	89.74	1.83
28.00	0.70	19.66	12.00	1.37	17.70	90.02	1.96
28.00	0.75	20.94	12.00	1.47	18.90	90.22	2.05
28.00	0.79	22.12	12.00	1.67	20.04	90.60	2.08

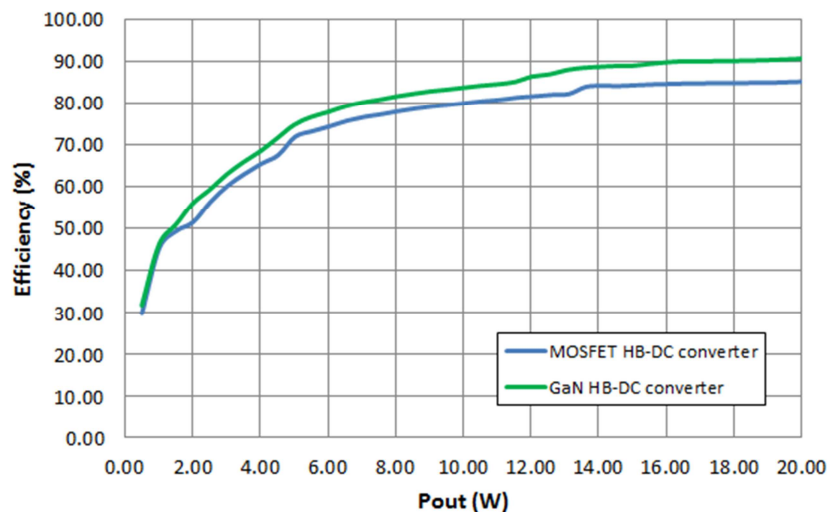
Comparison between GaN and Si technologies

At this point, the benefits of including GaN technology in switch-mode power supplies (SMPS) have been evaluated. As already mentioned, enhancement-mode Gallium Nitride (eGaN) FETS have been used for the implementation of isolated, as well as non-isolated converters. A GaN transistor is a wide bandgap device with superior conductivity compared to traditional silicon transistors resulting in smaller devices and lower capacitance for the on-resistance ($R_{DS(on)}$). Enhancement-mode operation allows taking the advantage of the performance benefits of gallium nitride in switching applications. eGaN FET's small size and lateral structure give ultra low capacitance while the scale packaging gives low inductance which provides improved capabilities in terms of switching speed and thus in the efficiency. The switching performance of eGaN FETS enables higher power density in smaller footprint.

With the aim of evaluating the benefits of this technology, a +28V to 12V HB-DC converter including Si MOSFETs has been designed and implemented as FIGURE 73(A) illustrates. This new PCB has been validated in the laboratory and its performance in terms of efficiency has been compared with the results obtained with the eGaN HB-DC converter as illustrated in FIGURE 73 (B). As can be seen, the eGaN HB-DC converter provides improved efficiency in a reduced size in comparison with the MOSFET HB-DC converter. In particular, the efficiency of the eGaN HB-DC is around 5 points better at maximum load.



(A)



(B)

FIGURE 73. (A) HB converter including MOSFETS (from +28V to +12V). (B) Comparison of efficiency of eGaN HB-DC converter vs MOSFET HB-DC converter.

The next step within the functional verification of the final design is the validation of the complete Isolated DC/DC converter. Due to a delay in the manufacturing of the boards, the complete validation of the source cannot be finalized before the delivery of this deliverable. This verification will be completed during the next stage of the project and the results will be included in the deliverable D4.1 which is planned to be submitted at the end of June.

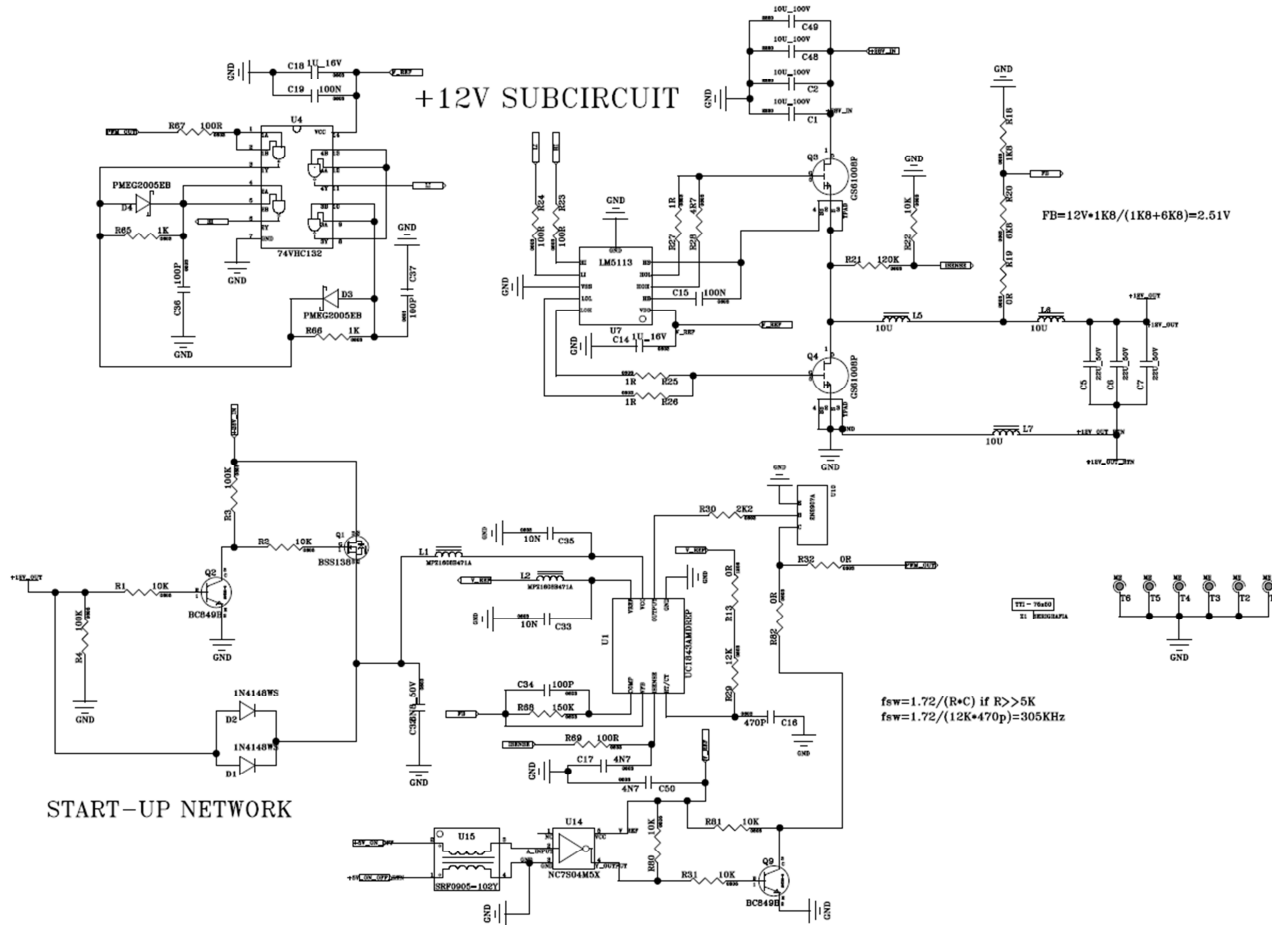
6. SUMMARY AND CONCLUSIONS

The design of the prototype 1 is completely finished. The description of the manufacturing and measurements procedures covers all the development and utilization activities for the susceptometer device. The prototype 1 has been tested in terms of performance with good results in the determination of the complex magnetic susceptibility. The TABLE 5 reflects some results for different manufactured samples. Following steps include integration of the prototype elements in a unique device, test the global performance and to perform a calibration of the device.

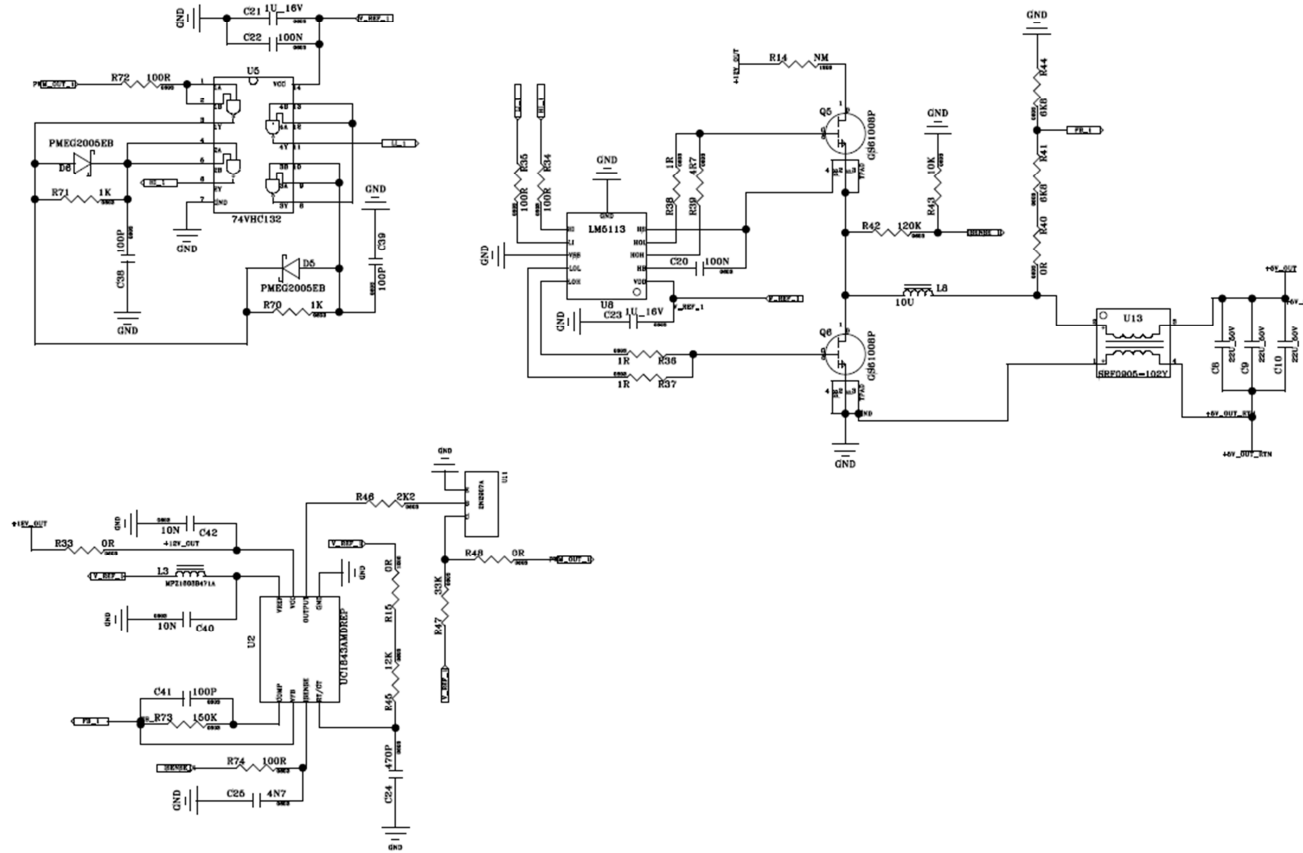
The measurements performed during the development of the device, apart from proving the reliability of the device and the techniques, has thrown some potential capabilities of the device to be considered for future exploitation. When measuring in R_{in} , as shown in section 3, we take measurements of module and phase(R, φ) or real part(X) and imaginary part(Y) of the voltage drop in the input resistor. If we watch the module of R , it increases for magnetic materials and decreases for conductive materials. Also, the resonance frequency increases when diamagnetic or conductive samples are presented. Current methods are not developed for finding absolute values of diamagnetic susceptibility or conductivity, but in a first approximation the device can be used to differentiate whether the material is diamagnetic or conductive. The same situation is found when measuring in the secondary coils. In this case, the situation is favorable for the identification the type of material (conductive, paramagnetic/ferromagnetic or diamagnetic), as the different effects of the magnetization and induced currents on each type of material produce a representative scenarios: positive and negative shift of the amplitude, and positive and negative shift of the phase.

With regard to the Control Unit and the Power Distribution Unit, the design of the CU has been finalized and its verification has been also performed. In the case of the PDU the design has been completed and partially validated. Additional validation test will be performed in the next stage of the project and reported in the following deliverables.

ANNEX 1: NON-ISOLATED DC/DC CONVERTER



+5V SUBCIRCUIT



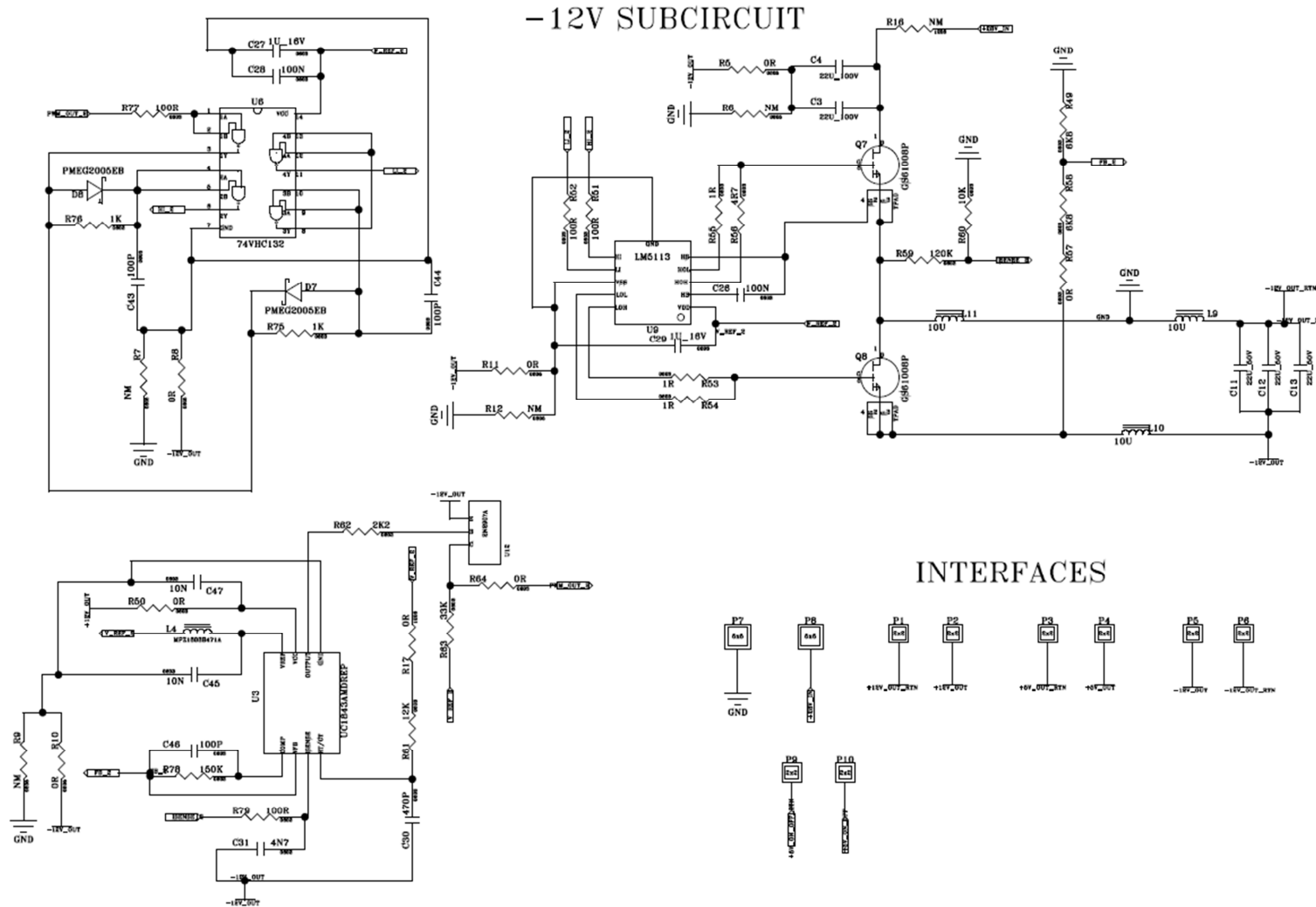


FIGURE 74. Complete schematic of the Non-isolated DC/DC converter.

TABLE 14. List of Components of the Non-isolated DC/DC converter.

REFDES	Value	Tol.	P/N: Commercial Version	MFG	P/N: Space Version	Temperature Range	Main Char.
C1,C2,C3,C4,C48,C49,C51	10U_100V	20%	22201C106MAT2A	AVX	BME X7R MLCC	-55 to 125°C	$V_{max}=100V$
C5,C6,C7,C8,C9,C10,C11,C12,C13	22U_50V	20%	RH225C226MA3RA3	AVX	BME X7R MLCC	-55 to 125°C	$V_{max}=500V$
C14,C18,C21,C23,C27,C29	1U_16V	10%	C1608X7R1C105K080AC	TDK	BME X7R MLCC	-55 to 125°C	$V_{max}=50V$
C15,C19,C20,C22,C26,C28	100N	10%	06035C104KAT2A	AVX	BME X7R MLCC	-55 to 125°C	$V_{max}=50V$
C16,C24,C30	470P	5%	C0603C471F5GACTU	KEMET	BME X7R MLCC	-55 to 125°C	$V_{max}=50V$
C17,C25,C31,C50	4N7	10%	C0603C472K3GACTU	KEMET	BME X7R MLCC	-55 to 125°C	$V_{max}=50V$
C32	6N8_50V	10%	C0603C682K5RACTU	KEMET	BME X7R MLCC	-55 to 125°C	$V_{max}=50V$
C33,C35,C40,C42,C45,C47	10N	10%	06031C103KAT2A	AVX	BME X7R MLCC	-55 to 125°C	$V_{max}=100V$
C34,C36,C37,C38,C39,C41,C43,C44,C46	100P	5%	06031A101JAT2A	AVX	BME X7R MLCC	-55 to 125°C	$V_{max}=100V$
D1,D2	1N4148WS	5%	1N4148WS	Microsemi	JANTXV1N4148-1	-75 to 175°C	$V_{max}=100V$
D3,D4,D5,D6,D7,D8	PMEG2005EB	0	PMEG2005EB	Nexperia	66293-002	-65 to 125°C	$V_{max}=20V$
L1,L2,L3,L4	MPZ1608B471A	25%	MPZ1608B471A	TDK	FCMS 30	-55 to 125°C	$I_{rms}=10A$
L5,L6,L7,L8,L9,L10,L11	10U	15%	994-SER8052-103MEB	COILCRAFT	ST615PTA103M	-55 to 125°C	$I_{rms}=9.2A$
Q1	BSS138	0	BSS138	Fairchild Semiconductor	IRFE310	-55 to 150°C	$V_{max}=400V$
Q2,Q9	BC849B	0	BC849B	NXP	2N3700HR	-55 to 200°C	$V_{max}=80V$
Q3,Q4,Q5,Q6,Q7,Q8	GS61008P	0	499-GS61008P-E05-MR	GaN Systems	FBG10N30BX	-55 to 150°C	$V_{max}=100V$
R1,R2,R31,R80,R81	10K	5%	CRCW080510K0JNEA	VISHAY	CHPR Series	-55 to 155°C	$V_{max}=150V$
R3,R4	100K	5%	120920 CRT0805-BY-1003ELF	BOURNS	CHPR Series	-55 to 155°C	$V_{max}=150V$
R5,R8,R10,R11	0R	5%	CR0805-J/-000ELF	BOURNS	CHPR Series	-55 to 155°C	$V_{max}=150V$
R13,R15,R17	0R	1%	CRCW12060000Z0EA	BOURNS	CHPR Series	-55 to 155°C	$V_{max}=200V$
R18	1K8	1%	CR0603-FX-1801ELF	BOURNS	CHPR Series	-55 to 155°C	$V_{max}=50V$
R19,R32,R33,R40,R48,R50,R57,R64,R82	0R	5%	CR0603-J/-000GLF	BOURNS	CHPR Series	-55 to 155°C	$V_{max}=50V$
R20,R41,R44,R49,R58	6K8	1%	CR0603-FX-6801ELF	BOURNS	CHPR Series	-55 to 155°C	$V_{max}=50V$
R21,R42,R59	120K	5%	CR0805-JW-124ELF	BOURNS	CHPR Series	-55 to 155°C	$V_{max}=50V$

R22,R43,R60	10K	1%	CR0603-FX-1002ELF	BOURNS	CHPR Series	-55 to 155°C	$V_{max}=150V$
R23,R24,R34,R35,R51,R52,R67,R69,R72,R74,R77, R79	100R	1%	CR0603-FX-1000ELF	BOURNS	CHPR Series	-55 to 155°C	$V_{max}=50V$
R25,R26,R27,R36,R37,R38,R53,R54,R55	1R	5%	CRT0805-CY-1R00ELF	BOURNS	CHPR Series	-55 to 155°C	$V_{max}=50V$
R28,R39,R56	4R7	5%	ESR10EZPJ4R7	BOURNS	CHPR Series	-55 to 155°C	$V_{max}=50V$
R29,R45,R61	12K	1%	CR0603-FX-1202ELF	BOURNS	CHPR Series	-55 to 155°C	$V_{max}=50V$
R30,R46,R62	2K2	1%	CR0603-FX-2201ELF	BOURNS	CHPR Series	-55 to 155°C	$V_{max}=50V$
R47,R63	33K	1%	CR0603-FX-3302ELF	BOURNS	CHPR Series	-55 to 155°C	$V_{max}=50V$
R65,R66,R70,R71,R75,R76	1K	1%	CR0603-FX-1001ELF	BOURNS	CHPR Series	-55 to 155°C	$V_{max}=50V$
R68,R73,R78	150K	5%	CRT0805-BY-1503EAS	BOURNS	CHPR Series	-55 to 155°C	$V_{max}=50V$
U1,U2,U3	UC1843AMDREP		UC1843AMDREP	TEXAS INSTRUMENTS	ST1843K1	-65 to 150°C	$V_{max}=30V$
U4,U5,U6	74VHC132	0	74VHC132MTCX	Fairchild Semiconductor	SN54AC00-SP	-65 to 150°C	$V_{max}=6V$
U7,U8,U9	LM5113		LM5113SD/NOPB	TEXAS INSTRUMENTS	Not found		
U10,U11,U12	2N2907A		2N2907A	MICROSEMI	2N3700HR	-55 to 200°C	$V_{max}=80V$
U13,U15	SRF0905-102Y	0.75%	SRF0905-102Y	BOURNS	ST515FRF3531LZ	-40°C to +85°C	$I_{rms}=0.5A$
U14	NC7S04M5X	0	NC7S04M5X	Fairchild Semiconductor	M54HC04	-55 to 200°C	$V_{max}=6V$

TABLE 15. List of Materials (ML).

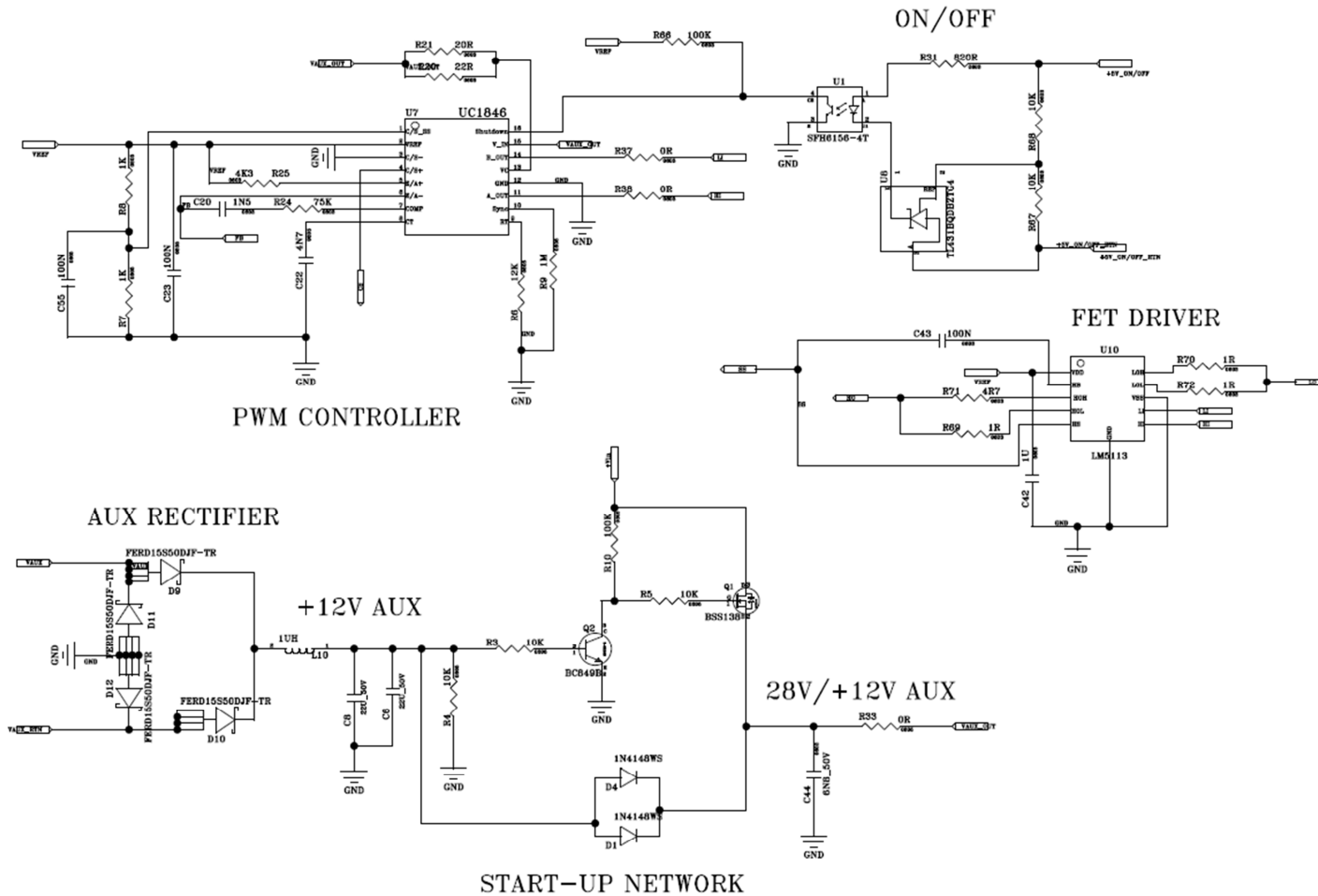
Item no.	1	2	3	4	5	6	7	8	9			10
									9.1	9.2	9.3	
	Grp.	Commercial identification and Description	1) Chemical nature 2) Product type	1) Manufacturer /Supplier name 2) Procurement spec. Issue/RevDate	Summary of process parameters	Use and Location 1) Subsystem 2) Equipment 3) Use	Environmental Code 1) A (Ambience) 2) T (Temperature)	Size Code 1) A (Area) 2) V (Volumen) 3) M (Masa)	Acronym/ rating/ Validation Ref. for applicable properties	1) Justification for approval 2) Prime comments	Prime approval status	Customer approval status/ comments
1	1	DC/DC converter mechanical enclosure material	Aluminium, conductive alodine finish		Thermal conditions		1) V 2) 4	1) A2 2) V3 3) TBC		ESCC-Q-ST-70-01		
2	15	PCB Board	Polyamide HASH tin lead		Tmax Tg		1) V 2) 4	1) A2 2) 3) TBC		ESCC-Q-ST-70-01		
3	8	SMD components Solder	62 tin silver solder		Soldering Temp Temperature Thermal resistance		1) V 2) 4	1) A1 2) 3) M0		ECSS-Q-70-71		
4	16	Solvents used for cleaning in soldering operations	isopropyl alcohol, 99 % pure				1) V 2) 4			ECSS-Q-ST-70-08C		
5	6	Screws, washers, nuts used for assembling , etc	Stainless steel				1) V 2) 4					
6	10	Non conductive epoxy used to attach the transformers to the mechanical	3M: 2216 B/A		Percentages Time of curing Temperature of curing		1) V 2) 4	1) A2 2) 3) M1		DOD-A-82720		
7	10	Non conductive epoxy used to attach the components weigher than 5 grs.	EPO-TEK 930		Percentages Time of curing		1) V 2) 4	1) A1 2) 3) M1		ECSS-Q-70-71A rev. 1		

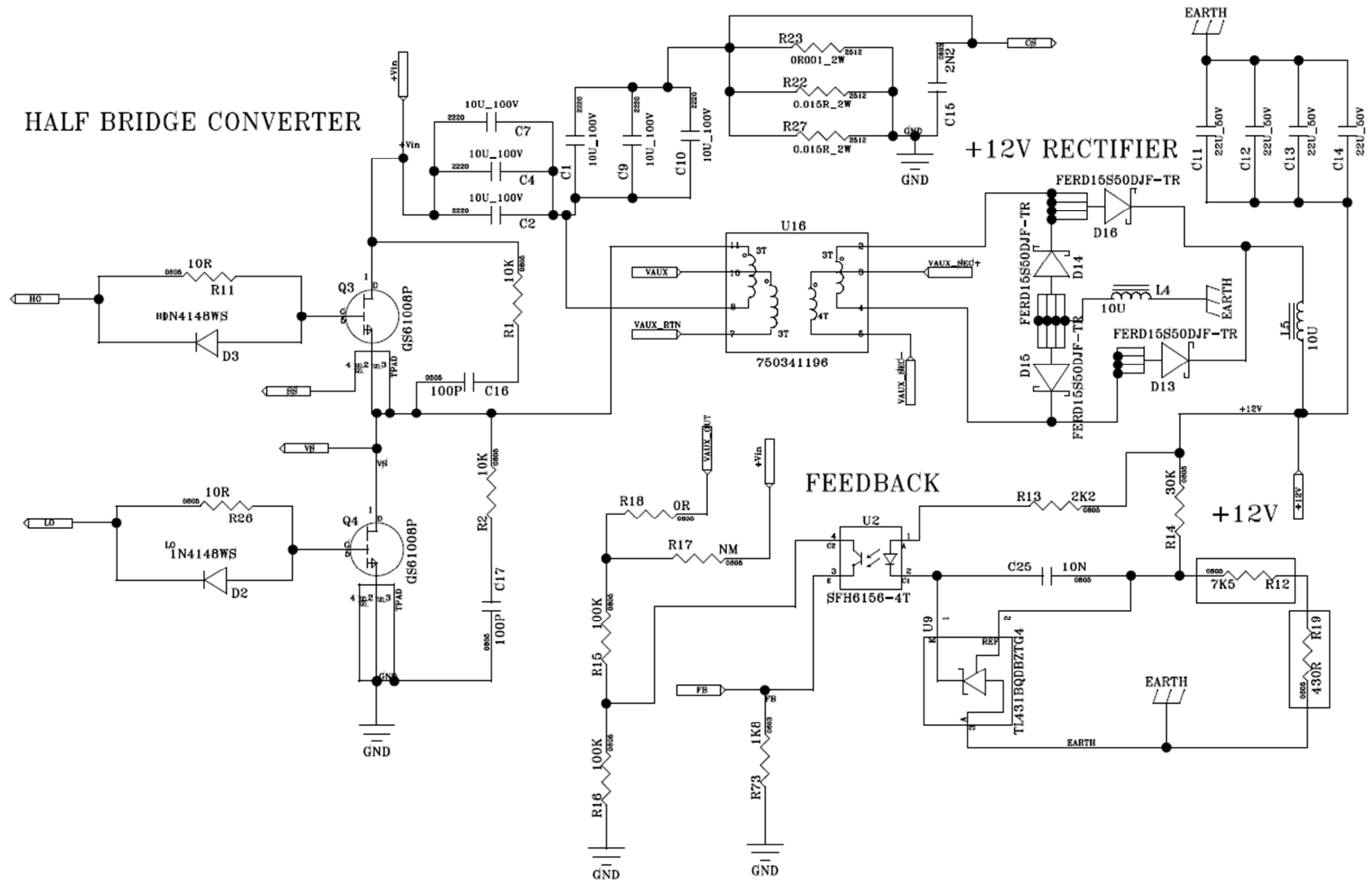
TABLE 16. List of Processes.

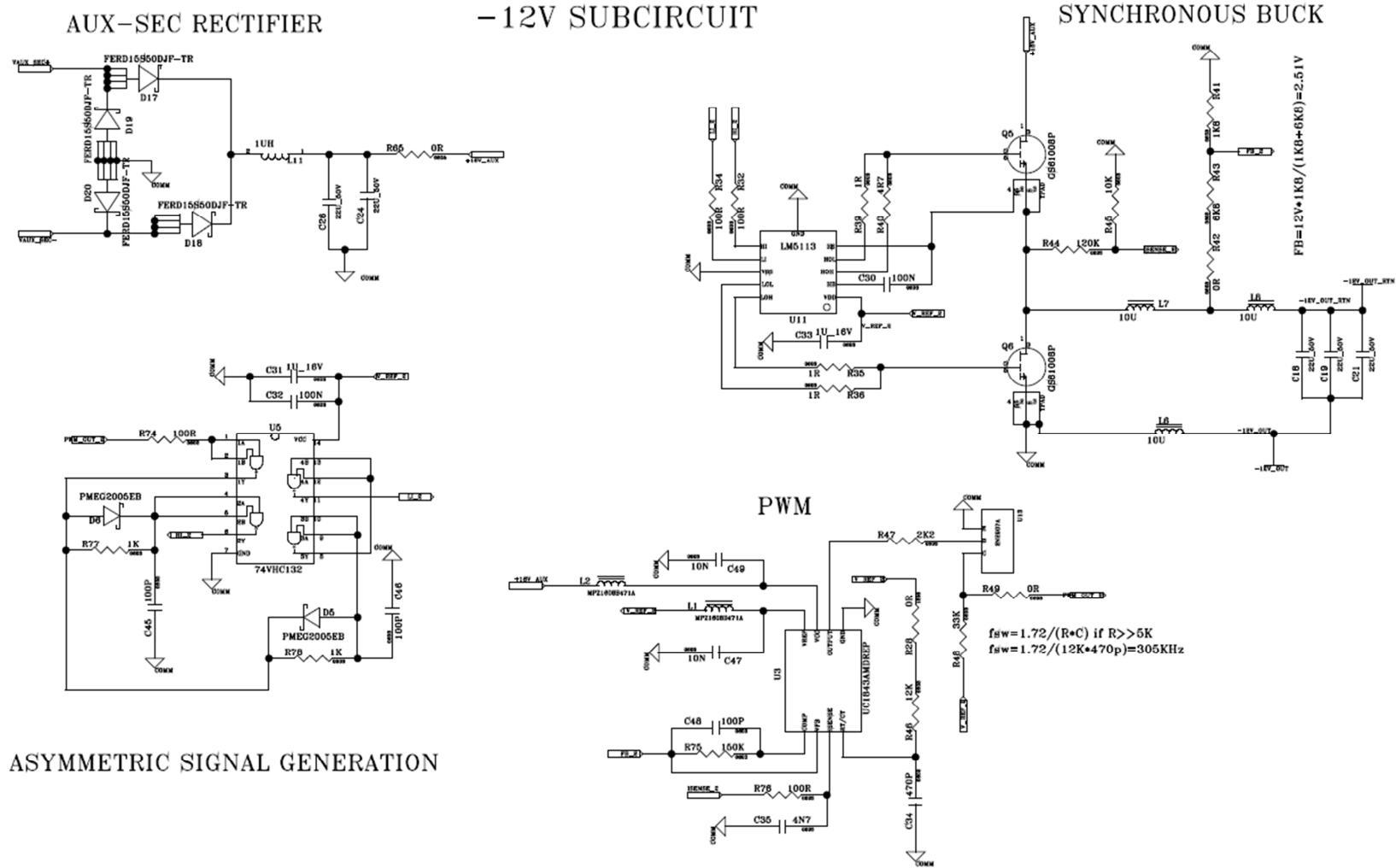
	1	2	3	4	5	6	7	8	9		10
Item no.	Group	Process Identification	1) User Name 2) Associated Procedure issue/revision/date	Process Description	Use and Location 1) Subsystem 2) Equipment 3) Use		Associated item numbers DML item number	1) Criticality 2) Reason for criticality	1) Supplier reference 2) Supplier comments	Supplier approval status	Prime approval status/ comment
1	8	SMD Soldering PCB	Supplier xxxx Soldering process	Reflow Reference Profile Temperature			Soldering material (ML_3) Polyamide HASH tin lead for EPC (ML_2) Solvents used for cleaning in soldering operations (ML_4)		ECSS-Q-ST-70-08C --> Manual soldering ECSS-Q-ST-70-38C --> SMD and mixed technology ECSS-Q-ST-70-28C --> Repair and modifications		
2	5	PCBs and mechanical cleaning	Supplier xxxx cleaning	Brushes			Box (ML-1) PCB (ML_2) Solvent (ML_4)		ECSS-Q-ST-70-08C --> Manual soldering ECSS-Q-ST-70-38C --> SMD and mixed technology ECSS-Q-ST-70-28C --> Repair and modifications		
3	1	Transformers to PCB attachment to mechanical	Supplier xxxx attaching process	Reference Profile Temperatures Curing time Percentages			Box (ML-1) Non Conductive epoxy (ML_6)		ECSS-Q-ST-70-08C --> Manual soldering ECSS-Q-ST-70-38C --> SMD and mixed technology ECSS-Q-ST-70-28C --> Repair and modifications ECSS-E-HB-32-21A --> Adhesive bonding Handbook		
4	1	Heavier (>5 gr) component attachment	Supplier xxxx attaching process	Reference Profile Temperatures Curing time Percentages			Box (ML-1) Non Conductive epoxy (ML_7)		ECSS-Q-ST-70-08C --> Manual soldering --> section 8.1.2 Heavy components ECSS-Q-ST-70-38C --> SMD and mixed technology ECSS-Q-ST-70-28C --> Repair and modifications ECSS-E-HB-32-21A --> Adhesive bonding Handbook		
5	16	Box manufacture	Supplier xxxx manufacture process	Manufacturing tolerances			Box material (ML_1)		ECSS-Q-ST-70-71		

6	16	PCBs manufacture	Supplier xxxx manufacture process	Space qualified protocol following ESCC rules: - Tolerances. - Finishes - Temperatures profiles			PCB material (ML_2)		ECSS-Q-ST-70-10C --> Qualification of PCBs ECSS-Q-ST-70-11C --> Procurement of PCBs ECSS-Q-ST-70-12C --> Design rules for PCBs		
7	16	Mechanical attachment/integration	Supplier xxxx attaching process	Reference Profile Temperatures Curing time Percentages			Box material (ML_1) Screws, washers, nuts, etc. (ML_5)		ECSS-Q-ST-70-28C --> Repair and modifications ECSS-Q-ST-70-18C --> Preparation, assembly and mounting of RF cables (TBC) ECSS-Q-ST-70-46C --> Requirements for manufacturing and procurement of threaded fasteners. ECSS-E-HB-32-21A --> Adhesive bonding Handbook		

ANNEX 2: ISOLATED DC/DC CONVERTER







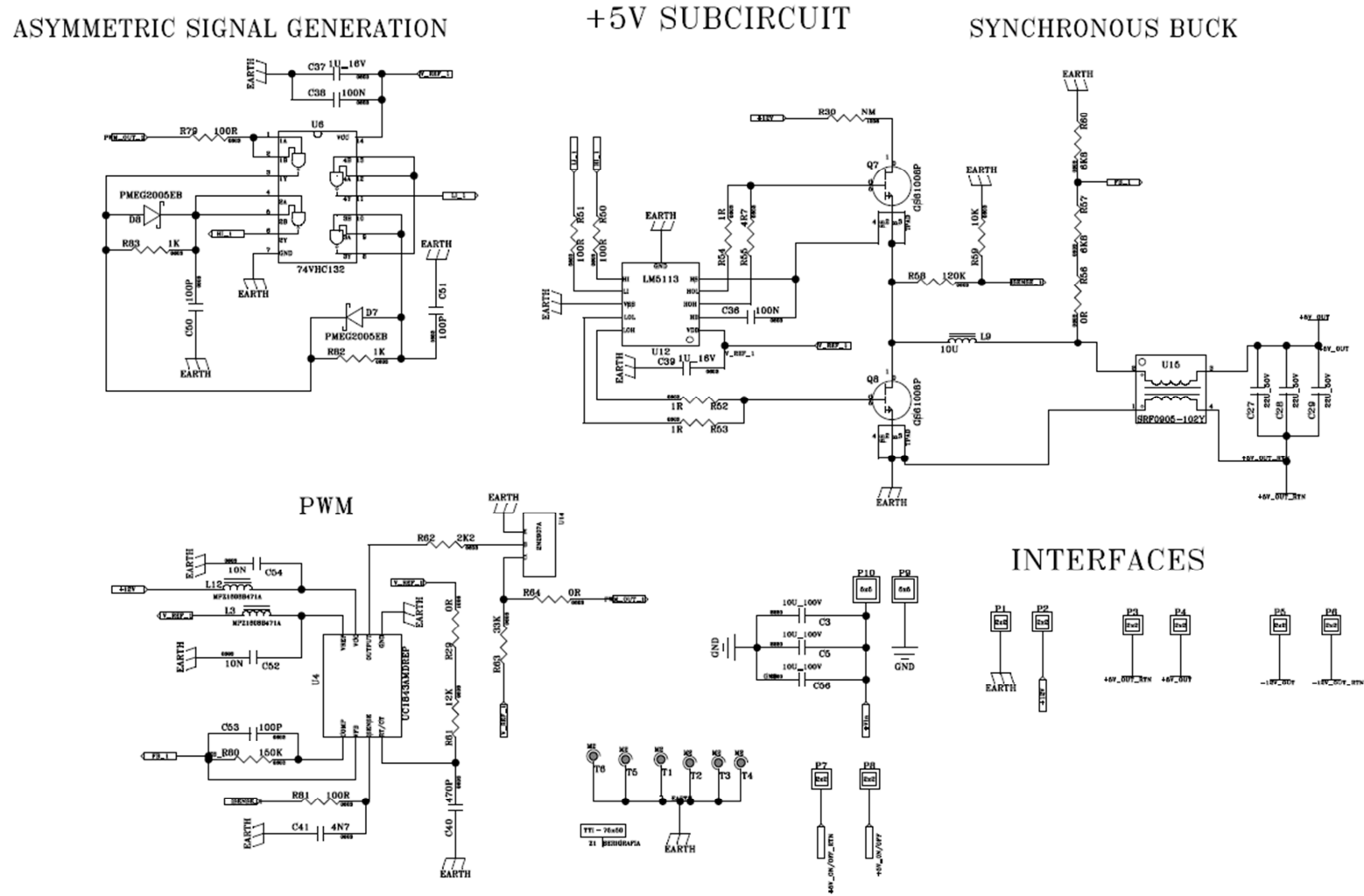


FIGURE 75. Complete schematic of the Isolated DC/DC converter.

TABLE 17. List of Components of the Isolated DC/DC converter.

REFDES	Value	Tol.	P/N: Commercial Version	MFG	P/N: Space Version	Temperature Range	Main Char.
C1,C2,C3,C4,C5,C7,C9,C10,C56	10U_100V	20%	22201C106MAT2A	AVX	BME X7R MLCC	-55 to 125°C	$V_{max}=100V$
C6,C8,C11,C12,C13,C14,C18,C19,C21,C24,C26,C27,C28,C29	22U_50V	20%	RH225C226MA3RA3	AVX	BME X7R MLCC	-55 to 125°C	$V_{max}=500V$
C15	2N2	10%	CC01W2201K	GENERIC			
C16,C17	100P	10%	C0603C101K1RACTU	KEMET	BME X7R MLCC	-55 to 125°C	$V_{max}=100V$
C20	1N5	5%	06035C152KAT2A	AVX	BME X7R MLCC	-55 to 125°C	$V_{max}=100V$
C22	4N7	10%	08055C472KAT2A	AVX	BME X7R MLCC	-55 to 125°C	$V_{max}=50V$
C23,C55	100N	10%	08051C104KAT2A	AVX	BME X7R MLCC	-55 to 125°C	$V_{max}=50V$
C25	10N	10%	08051C103KAT2A	AVX	BME X7R MLCC	-55 to 125°C	$V_{max}=100V$
C30,C32,C36,C38,C43	100N	10%	06035C104KAT2A	AVX	BME X7R MLCC	-55 to 125°C	$V_{max}=50V$
C31,C33,C37,C39	1U_16V	10%	C1608X7R1C105K080AC	TDK	BME X7R MLCC	-55 to 125°C	$V_{max}=50V$
C34,C40	470P	5%	C0603C471F5GACTU	KEMET	BME X7R MLCC	-55 to 125°C	$V_{max}=50V$
C35,C41	4N7	10%	C0603C472K3GACTU	KEMET	BME X7R MLCC	-55 to 125°C	$V_{max}=50V$
C42	1U	10%	C0603C105K3PACTU	KEMET	BME X7R MLCC	-55 to 85°C	$V_{max}=25V$
C44	6N8_50V	10%	C0603C682K5RACTU	KEMET	BME X7R MLCC	-55 to 125°C	$V_{max}=50V$
C45,C46,C48,C50,C51,C53	100P	5%	06031A101JAT2A	AVX	BME X7R MLCC	-55 to 125°C	$V_{max}=100V$
C47,C49,C52,C54	10N	10%	06031C103KAT2A	AVX	BME X7R MLCC	-55 to 125°C	$V_{max}=100V$
D1,D2,D3,D4	1N4148WS	5%	1N4148WS	Microsemi	JANTXV1N4148-1	-75 to 175°C	$V_{max}=100V$
D5,D6,D7,D8	PMEG2005EB	0	PMEG2005EB	Nexperia	1N5822U	-65 to 125°C	$V_{max}=40V$
D9,D10,D11,D12,D13,D14,D15,D16,D17,D18,D19,D20	FERD15S50DJF-TR	0	FERD15S50DJF-TR	STMicroelectron.	STPS1045HR	-65 to 175°C	$V_{max}=45V$
L1,L2,L3,L12	MPZ1608B471A	25%	MPZ1608B471A	TDK	FCMS 30	-55 to 125°C	$I_{rms}=10A$
L4,L5,L6,L7,L8,L9	10U	15%	994-SER8052-103MEB	COILCRAFT	ST615PTA103M	-55 to 125°C	$I_{rms}=9.2A$
L10,L11	1UH	20%	XAL4020-102MEB	COILCRAFT	ML566PNB102MLZ	-40 to 165°C	$I_{rms}=6A$
Q1	BSS138	0	BSS138	Fairchild Semiconductor	IRFE310	-55 to 150°C	$V_{max}=400V$
Q2	BC849B	0	BC849B	NXP	2N3700HR	-55 to 200°C	$V_{max}=80V$

Q3,Q4,Q5,Q6,Q7,Q8	GS61008P	0	499-GS61008P-E05-MR	GaN Systems	FBG10N30BX	-55 to 150°C	$V_{max}=100V$
R1,R2,R3,R4,R5	10K	5%	CRCW080510K0JNEA	VISHAY	CHPR Series	-55 to 155°C	$V_{max}=150V$
R6	12K	1%	ERJ-6ENF1202V	PANASONIC	CHPR Series	-55 to 155°C	$V_{max}=150V$
R7,R8	1K	1%	RC0805FR-071KL	YAGEO	CHPR Series	-55 to 155°C	$V_{max}=150V$
R9	1M	1%	CRCW08051M00FKEA	VISHAY	CHPR Series	-55 to 155°C	$V_{max}=150V$
R10,R15,R16	100K	5%	120920 CRT0805-BY-1003ELF	BOURNS	CHPR Series	-55 to 155°C	$V_{max}=150V$
R11,R26	10R	1%	CR0805-FX-10R0ELF	BOURNS	CHPR Series	-55 to 155°C	$V_{max}=150V$
R12	7K5	1%	RC0805FR-071KL	YAGEO	CHPR Series	-55 to 155°C	$V_{max}=150V$
R13	2K2	1%	ERJ-6ENF2201V	PANASONIC	CHPR Series	-55 to 155°C	$V_{max}=150V$
R14	30K	5%	CR0805-FX-3002ELF	BOURNS	CHPR Series	-55 to 155°C	$V_{max}=150V$
R18,R33,R37,R38,R65	0R	5%	CR0805-J/-000ELF	BOURNS	CHPR Series	-55 to 155°C	$V_{max}=150V$
R19	430R	1%	RC0805FR-071KL	YAGEO	CHPR Series	-55 to 155°C	$V_{max}=150V$
R20	22R	1%	CR0603-FX-22R0ELF	BOURNS	CHPR Series	-55 to 155°C	$V_{max}=50V$
R21	20R	1%	CR0603-FX-20R0ELF	BOURNS	CHPR Series	-55 to 155°C	$V_{max}=50V$
R22,R27	0.015R_2W	1%	LRC-LRF2512LF-01-R015-F	TT ELECTRONICS	CHPR Series	-55 to 155°C	$V_{max}=150V$
R23	0R001_2W	5%	CRF2512-JV-R001ELF	BOURNS	CHPR Series	-55 to 155°C	$V_{max}=150V$
R24	75K	1%	CR0603-FX-7502ELF	BOURNS	CHPR Series	-55 to 155°C	$V_{max}=150V$
R25	4K3	1%	CR0603-FX-7502ELF	BOURNS	CHPR Series	-55 to 155°C	$V_{max}=150V$
R28,R29	0R	1%	CRCW12060000Z0EA	BOURNS	CHPR Series	-55 to 155°C	$V_{max}=200V$
R31	820R	1%	CR0603-FX-8200ELF	BOURNS	CHPR Series	-55 to 155°C	$V_{max}=50V$
R32,R34,R50,R51,R74,R76,R79,R81	100R	1%	CR0603-FX-1000ELF	BOURNS	CHPR Series	-55 to 155°C	$V_{max}=50V$
R35,R36,R39,R52,R53,R54,R69,R70,R72	1R	5%	CRT0805-CY-1R00ELF	BOURNS	CHPR Series	-55 to 155°C	$V_{max}=50V$
R40,R55,R71	4R7	5%	ESR10EZPJ4R7	BOURNS	CHPR Series	-55 to 155°C	$V_{max}=50V$
R41,R73	1K8	1%	CR0603-FX-1801ELF	BOURNS	CHPR Series	-55 to 155°C	$V_{max}=150V$

R42,R49,R56,R64	0R	5%	CR0603-J/-000GLF	BOURNS	CHPR Series	-55 to 155°C	V _{max} =50V
R43,R57,R60	6K8	1%	CR0603-FX-6801ELF	BOURNS	CHPR Series	-55 to 155°C	V _{max} =150V
R44,R58	120K	5%	CR0805-JW-124ELF	BOURNS	CHPR Series	-55 to 155°C	V _{max} =50V
R45,R59,R67,R68	10K	1%	CR0603-FX-1002ELF	BOURNS	CHPR Series	-55 to 155°C	V _{max} =50V
R46,R61	12K	1%	CR0603-FX-1202ELF	BOURNS	CHPR Series	-55 to 155°C	V _{max} =150V
R47,R62	2K2	1%	CR0603-FX-2201ELF	BOURNS	CHPR Series	-55 to 155°C	V _{max} =50V
R48,R63	33K	1%	CR0603-FX-3302ELF	BOURNS	CHPR Series	-55 to 155°C	V _{max} =150V
R66	100K	1%	CR0603-FX-1003ELF	BOURNS	CHPR Series	-55 to 155°C	V _{max} =150V
R75,R80	150K	5%	CRT0805-BY-1503EAS	BOURNS	CHPR Series	-55 to 155°C	V _{max} =150V
R77,R78,R82,R83	1K	1%	CR0603-FX-1001ELF	BOURNS	CHPR Series	-55 to 155°C	V _{max} =50V
U1,U2	SFH6156-4T	0	SFH6156-4T	VISHAY	66293-002	-55 to 150°C	V _{max} =6V
U3,U4	UC1843AMDREP		UC1843AMDREP	TEXAS	ST1843K1	-65 to 150°C	V _{max} =30V
U5,U6	74VHC132	0	74VHC132MTCX	Fairchild Semiconductor	HCC40107BKG FP-14	-65 to 150°C	V _{max} =7V
U7	UC1846	0	UC1846MDWREP	TEXAS INSTRUMENTS	UC1846-EP	-65 to 125°C	V _{max} =40V
U8,U9	TL431BQDBZTG4	0.50%	TL431BQDBZTG4	TEXAS INSTRUMENTS	TL1431-SP	-55 to 125°C	V _{max} =36V
U10,U11,U12	LM5113		LM5113SD/NOPB	TEXAS INSTRUMENTS	Not found		
U13,U14	2N2907A		2N2907A	MICROSEMI	2N3700HR	-55 to 200°C	V _{max} =80V
U15	SRF0905-102Y	0.75%	SRF0905-102Y	BOURNS	5962-0420401H	-55 to 125°C	V _{max} =2.5V
U16	750341196		750341196	WURTH MIDCOM	Custom		

The list of materials and list of processes are the same as the previously reported in Annex 1 for the Non-Isolated solution.

REFERENCES

- [1] Zhang, W., Appel, E., Fang, X., Yan, M., Siong, C., & Cao, L. (2012). Paleoclimatic implications of magnetic susceptibility in Late Pliocene-Quaternary sediments from deep drilling core SG-1 in western Qaidam Basin (NE Tibetan Plateau). *J. Geophys. Res.*, Vol. 117, B06101.
- [2] M. Sanz et al, "Final Design Report: NEWTON instrument prototype 2", H2020-COMPET-2016 NEWTON - 730041, Report D3.5, April 2018.
- [3] C. Lavín et al, "Final Design Report: NEWTON instrument prototype 3", H2020-COMPET-2016 NEWTON - 730041, Report D3.6, April 2018.
- [4] M. Díaz-Michelena et al, "Preliminary design report for the magnetic head ", H2020-COMPET-2016 NEWTON - 730041, Report D3.1, October 2017.
- [5] C. Lavín et al, "Definition of instrument requirements and architecture. Design guidelines", H2020-COMPET-2016 NEWTON - 730041, Report D2.1, February 2017.
- [6] M. Sanz et al, "Preliminary design report for the electronic control block ", H2020-COMPET-2016 NEWTON - 730041, Report D3.2, October 2017.
- [7] C. Lavín et al, "Preliminary design report for power distribution block ", H2020-COMPET-2016 NEWTON - 730041, Report D3.3, October 2017.
- [8] ECSS-Q-ST-30-11C. "Space Product Assurance. Derating. EEE components". Date 4 October 2011.